

DEVELOPMENT AND USE OF A NEW CURVATURE RELAXATION
TECHNIQUE TO MEASURE THE *IN SITU* OXYGEN SURFACE EXCHANGE
COEFFICIENTS AND STRESS OF LANTHANUM STRONTIUM FERRITE FILMS

By

Qing Yang

A DISSERTATION

Submitted to
Michigan State University
in partial fulfillment of the requirements
for the degree of

Materials Science and Engineering—Doctor of Philosophy

2014

ABSTRACT

DEVELOPMENT AND USE OF A NEW CURVATURE RELAXATION TECHNIQUE TO MEASURE THE *IN SITU* OXYGEN SURFACE EXCHANGE COEFFICIENTS AND STRESS OF LANTHANUM STRONTIUM FERRITE FILMS

By

Qing Yang

Solid oxide fuel cells (SOFCs) provide fuel flexibility and the highest efficiency of any chemical-to-electrical energy conversion technology. Unfortunately, slow oxygen transport, especially that caused by low surface exchange kinetics at the cathode, limits overall SOFC performance. In the common SOFC material $\text{La}_{0.6}\text{Sr}_{0.4}\text{FeO}_{3-\delta}$ (LSF64) efforts to engineer and understand oxygen surface exchange have been complicated by the 5 orders of magnitude chemical surface exchange coefficient (k) discrepancy reported in the literature. To help remedy this discrepancy, a new bilayer curvature relaxation technique utilizing the mechano-chemical coupling of LSF64 was developed in this work. This technique provides reliable, *in-situ*, electrode-free, simultaneous measurement of film stress and k as a function of temperature and oxygen partial pressure. This is demonstrated here by measuring LSF64 films prepared via sputter deposition, pulsed laser deposition, and colloidal spray deposition. The similarities and differences between these films are systematically investigated across multiple thermal cycles, and correlated to the microstructure, stress state and sample preparation/testing history. Further, the k of LSF64 films was measured here below 500°C for the first time, and distinct lattice-dominated and grain-boundary-dominated chemical stress responses were identified.

ACKNOWLEDGMENTS

I am deeply grateful to those who have provided motivation, help and support throughout the course my doctoral study. First, I would like to thank my advisor, Dr. Jason D. Nicholas, for the tremendous help in research project blueprinting, laboratory construction, and encouragement on all aspects of being a researcher (especially when things don't go smoothly as one would like). I'm also grateful to my dissertation committee members Dr. Donald Morelli, Dr. Eldon Case and Dr. Ruby Ghosh for their guidance and support. I sincerely thank my past and present group members/lab-mates Lin Wang, Ted Burye, Andrew Flegler, Peter Su, Laura Bartow-Goudie, Vasiliy Sharikov-Bass and Tridip Das for their helpful discussions and routine lab assistance on a regular basis. I also appreciate Dr. Richard Lunt, Chris Traverse and Vasiliy Sharikov-Bass for assistance in sputtered thin film fabrication, and Dr. William Chueh and Sylvia Paris for assistance in PLD thin film fabrication. Valuable contributions from other collaborators Dr. Xiaofeng Fan, Dr. Per Askeland, Mr. Edward Timm and Mr. Scott Bankroff are also appreciated.

I would also like to acknowledge the generous financial support provided by the Army Research Office under contract number W911NF-13-0404, a Michigan State University faculty startup grant to Dr. Jason D. Nicholas, and fellowships from the Michigan State Graduate School, the College of Engineering, and the Department of Chemical Engineering and Materials Science. Support for the Composite Materials and Structures Center, provided by the NSF-MRI program and Michigan State University, is also acknowledged.

Finally, my special thanks go to my parents, who flew all the way from the other side of the planet and stayed with me during the last months of my doctoral study. I am forever indebted to their unconditional love, and this dissertation is dedicated to them.

TABLE OF CONTENTS

LIST OF TABLES	viii
LIST OF FIGURES.....	ix
KEY TO SYMBOLS AND ABBREVIATIONS	xiv
1. Motivation and Project Overview	1
1.1. Energy Challenges.....	1
1.2 Fuel Cells.....	1
1.2.1 Applications	1
1.2.2 Types of Fuel Cells.....	2
1.2.3. SOFC Overview	26
1.2.3.1 Components and Operating Principles	26
1.2.3.2 Materials and Requirements of SOFC Components	27
1.2.3.2.1 Cathode.....	27
1.2.3.2.2 Anode	28
1.2.3.2.3 Electrolyte	28
1.2.3.2.4 Interconnect.....	30
1.3 Technological Progress of SOFCs.....	30
1.4 Current Challenges at the SOFC Cathode.....	30
1.5 Hypothesis and Aim of this Work.....	32
2 Literature Review.....	34
2.1 Mechano-Chemical Coupling in Solid Oxide Fuel Cell Materials.....	34
2.1.1 Strain in Electro-ceramic Devices.....	34
2.1.2 Chemical Expansion in MIEC Materials.....	35
2.1.3 Utilizing Mechano-chemical Coupling	37
2.2 Oxygen Surface Exchange and its Measurement.....	37
2.2.1 The Characteristic Thickness.....	38
2.2.2 The Different Types of Oxygen Surface Exchange Coefficients.....	38
2.2.2.1 Chemical Exchange Coefficient	38
2.2.2.2 Tracer Exchange Coefficient.....	40
2.2.2.3 Electrically Determined Surface Exchange	40
2.2.3 Literature Oxygen Surface Exchange Coefficient Measurement Techniques	41
2.2.3.1 Oxygen Permeation.....	43
2.2.3.2 Ionic Conductivity.....	43
2.2.3.3 Isotope Exchange Depth Profiling	44
2.2.3.4 Electrical Conductivity Relaxation	45
2.2.3.5 <i>In situ</i> Isothermal Isotope Exchange	46
2.2.3.6 Electrical Titration	46
2.2.3.7 Thermogravimetric Relaxation.....	47
2.2.3.8 Optical Absorption Relaxation	47
2.2.3.9 Strain Relaxation by X-ray Diffraction	48
2.3 The Factors Governing Oxygen Surface Exchange.....	48
2.3.1 Material Composition (Dopants and Doping Level)	49

2.3.2	Oxygen Partial Pressure	50
2.3.3	Surface and Interface Structure.....	51
2.3.4	Grain Size	51
2.3.5	Electronic structure.....	52
2.3.6	Strain	52
2.3.7	Dislocations	53
3	Experimental Methods	55
3.1	The Bilayer Curvature Relaxation Technique	55
3.1.1	Theoretical Background	55
3.1.2	Experimental Setup.....	57
3.1.3	Flush Time Considerations	60
3.1.4	Film Stress Measurement.....	61
3.1.5	Substrate Selection	62
3.1.6	Error Analysis	63
3.1.7	Summary	64
3.2	Sample Preparation	65
3.2.1	Powder Processing.....	65
3.2.2	Sputtering Target Preparation.....	65
3.2.3	Sputter Deposition	66
3.2.4	Pulsed Laser Deposition (PLD)	66
3.2.5	Colloidal Spray Deposition	66
3.3	Dilatometry	67
3.4	Structural, Morphological and Compositional Characterization.....	68
3.4.1	X-ray Diffraction.....	68
3.4.2	Focused Ion Beam-Scanning Electron Microscopy (FIB-SEM)	68
3.4.3	X-ray Photoelectron Spectroscopy (XPS).....	69
4.	Dilatometry Measurements on Bulk LSF64	70
4.1	Introduction	70
4.2	Experimental.....	70
4.3	Results and Discussion.....	71
4.4	Conclusions	74
5.	Oxygen Surface Exchange and Stress Measurements on Sputtered LSF64 Dense Thin Films	76
5.1	Introduction	76
5.2	Experimental.....	77
5.2.1	Sample Preparation	77
5.2.2	Curvature Relaxation (κR) Measurements.....	78
5.2.3	Structural and Compositional Characterization	78
5.3	Results and Discussion.....	79
5.4	Conclusions	95
6.	Oxygen Surface Exchange and Stress Measurements on Pulsed Laser Deposited LSF64 Dense Thin Films.....	96
6.1	Introduction	96
6.2	Experimental.....	96
6.2.1	Sample Fabrication	96
6.2.2	Curvature Relaxation Measurements.....	97
6.2.3	Structural and Compositional Characterization	97
6.3	Results and Discussion.....	98

6.3.1 LSF64 YSZ.....	98
6.3.2 LSF64 SDC YSZ.....	108
6.4 Conclusions	116
7. Oxygen Surface Exchange and Stress Measurements on Spray Deposited LSF64 Porous Thick Films ..	117
7.1 Introduction	117
7.2 Experimental.....	117
7.2.1 Sample Fabrication.....	117
7.2.2 Porous Pellet Dilatometry.....	117
7.2.3 Curvature Relaxation Measurements.....	118
7.2.4 Structural and Morphological Characterization	118
7.3 Results and Discussion.....	119
7.4 Conclusions	135
8. Dissertation Summary	136
APPENDIX.....	140
REFERENCES	144

LIST OF TABLES

<i>Table 1 Selected features of different types of fuel cells. [10-13]</i>	4
<i>Table 2 Chemical expansion coefficients of common MIEC materials</i>	36
<i>Table 3 Methods for determining surface exchange coefficients and a comparison of their advantages/disadvantages.</i>	42
<i>Table 4 Atomic fractions of cation species at the surface of sputtered thin film SP-A.</i>	94
<i>Table 5 XPS measurement on the PLD LSF64 YSZ thin film after κR testing.</i>	107
<i>Table 6 Comparison of XPS measurements on the PLD LSF64 YSZ and LSF64 SDC YSZ thin films and the sputtered LSF64 δYSZ film after κR testing.</i>	115

LIST OF FIGURES

<i>Figure 1.1 Fuel cell market growth from 2009 to 2013. [4]</i>	<i>2</i>
<i>Figure 1.2 Planar (left) and tubular (right) design of SOFCs and their components.</i>	<i>26</i>
<i>Figure 1.3 Ionic conductivity of common SOFC electrolyte materials. Practical application requires area specific resistance (ASR) values $\leq 0.15 \Omega\text{cm}^2$. Therefore, a minimum target conductivity value of 0.01Scm^{-1} is necessary so inexpensive colloidal fabrication techniques producing dense electrolyte films $15 \mu\text{m}$ thick can be used. This helps dictate the necessary SOFC operating temperature. This figure was reproduced from Ref. [3].</i>	<i>29</i>
<i>Figure 1.4 Voltage drop of a typical SOFC operated at 100mA/cm^2 and various temperatures [53].</i>	<i>31</i>
<i>Figure 3.1 Curvature relaxation measurement apparatus schematic.</i>	<i>57</i>
<i>Figure 3.2 A 3×3 array of laser spots detected by the MOSS CCD camera</i>	<i>58</i>
<i>Figure 3.3 Temperature calibration of the furnace controller between 200°C and 700°C using actual sample chamber temperature measurements.</i>	<i>59</i>
<i>Figure 4.1 X-ray diffraction scans of calcined LSF64 powder. Peak indexing was performed using LSF64 PDF # 01-082-1961</i>	<i>71</i>
<i>Figure 4.2 Bulk, dense LSF64 sample dilatometry under $p\text{O}_2=0.21$ (black), $p\text{O}_2=0.021$ (blue), $p\text{O}_2=0.0005$ (orange) and N_2 (red). The dashed line represents the fitted linear thermal expansion.</i>	<i>72</i>
<i>Figure 4.3 Bulk, porous LSF64 sample dilatometry in air ($p\text{O}_2=0.21$). The dashed line denotes the temperature schedule and the solid line denotes the measured linear strain.</i>	<i>74</i>
<i>Figure 5.1 (a) Macroscale morphology of YSZ substrates with (left) and without (right) a LSF64 film. (b) cross section and (c) 45° view of the fracture surface morphology of the LSF64 YSZ bilayer after κR testing</i>	<i>79</i>
<i>Figure 5.2 X-ray diffraction scans of YSZ substrates (a) without any coating, (b) with as-sputtered with LSF64 film, (c) with a 4-day MOSS tested LSF64 film [203] and (d) with a 60-day MOSS tested LSF64</i>	

<i>film (this study). Peak indexing was obtained from PDF #01-082-1961 for LSF64, 01-070-4436 for cubic YSZ (c-YSZ) and 01-070-4431 for tetragonal YSZ (t-YSZ).</i>	80
<i>Figure 5.3 Representative multiple curvature relaxation cycles between $pO_2=0.21$ (air) and $pO_2=0.021$ (N_2-air) at 525°C and 475°C. The difference in equilibrium curvature levels between the two temperatures stems from the film-substrate thermal expansion mismatch [193, 205].</i>	81
<i>Figure 5.4 Normalized curvature relaxation data (dots) of the LSF64 film SP-C on reduction at 525°C (left) and on oxidation at 375°C (right). The top line is the combined fit to the data, while the lower lines show the separate contributions of each relaxation rate.</i>	82
<i>Figure 5.5 The κR data of 525°C on reduction plotted on a semi-log plot to illustrate that two relaxation times, τ_1 and τ_2, are present.</i>	83
<i>Figure 5.6 Schematic of the surface exchange process in the sputtered thin film. k_1 and k_2, can be attributed to bulk grains and grain boundaries, respectively.</i>	84
<i>Figure 5.7 A_1 values of the sputtered LSF64 thin film SP-C as a function of temperature across all seven thermal segments. Each value is averaged from its corresponding oxidation and reduction relaxation processes.</i>	84
<i>Figure 5.8 Arrhenius plots of both k_1 and k_2 in LSF64 thin film sample SP-B under oxidation and reduction conditions. Segment numbers follow the chronological order of the experiment. Segments 1, 3, 5 and 7 were measurements as the sample was cooling down, while segments 2, 4 and 6 were measurements as the sample was heating up.</i>	85
<i>Figure 5.9 Arrhenius plot of both k_1 and k_2 of LSF64 thin film sample SP-C under oxidation and reduction conditions.</i>	87
<i>Figure 5.10 κR-determined k_1 values of sputtered LSF64 thin film samples SP-A, SP-B and SP-C as a function of inverse temperature across multiple thermal cycles. k values are averaged from oxidation and reduction k's.</i>	88
<i>Figure 5.11 κR-determined k_2 values of sputtered LSF64 thin film samples SP-A, SP-B and SP-C as a function of inverse temperature across multiple thermal cycles. k values are averaged from oxidation and reduction k's.</i>	89
<i>Figure 5.12 LSF64 κR-determined k_1 values compared with those in the literature [47-50]. Open symbols denote literature values.</i>	90

Figure 5.13 Average equilibrium stress levels of the LSF64 film as a function of pO_2 and temperature. The dashed lines represent thermal expansion mismatch induced stress, based on coefficient of thermal expansion (CTE) and elastic constants of YSZ and LSF64 available in the literature [193, 205].91

Figure 5.14 Chemical stress of sputtered LSF64 films induced by pO_2 changes between 0.21 and 0.021 as a function of temperature.93

Figure 5.15 X-ray photoelectron spectroscopy (XPS) measurements on the sputtered LSF64 thin film SP-A after κR testing94

Figure 6.1 Fracture surface morphology of the PLD LSF64|YSZ bilayer after κR testing.98

Figure 6.2 X-ray diffraction scans of the PLD LSF64|YSZ before and after κR testing. Peak indexing was performed using LSF64 PDF # 01-082-1961 for LSF64 and cubic YSZ PDF# 01-070-4436.99

Figure 6.3 Multiple curvature relaxation cycles of the LSF64|YSZ sample at 700°C and 750°C between $pO_2=0.21$ and $pO_2=0.021$. The difference in equilibrium curvature levels between the two temperatures is a result of the film-substrate thermal expansion mismatch. 100

Figure 6.4 Representative κR data of 700°C on reduction shown in Figure 6.3 replotted on a semi-log plot, and showing only one time constant. κR data of other temperatures showed similar single time constant behavior. 101

Figure 6.5 κR -measured surface exchange coefficients of LSF64|YSZ as a function of temperature and flow rate..... 102

Figure 6.6 κR -measured k values of LSF64|YSZ across multiple thermal segments at a flow rate of 100 sccm. 103

Figure 6.7 κR -determined k values of LSF64|YSZ compared with those in the literature [47-50] and the sputtered thin films in this work. 104

Figure 6.8 Average equilibrium stress levels of the PLD LSF64 thin film as a function of pO_2 and temperature. The dashed lines represent thermal expansion mismatch induced stress, based on coefficient of thermal expansion (CTE) and elastic constants of YSZ and LSF64 available in the literature [193, 194]. 700°C was chosen as the stress-free state in line with the film deposition temperature. 105

Figure 6.9 Chemical stress of the PLD thin film LSF64|YSZ induced by pO_2 changes between 0.21 and 0.021 as a function of temperature. 106

Figure 6.10 X-ray photoelectron spectroscopy (XPS) measurements of a PLD LSF64/YSZ sample.....	107
Figure 6.11 X-ray diffraction scans of the PLD LSF64/SDC/YSZ before and after κ R test. Peak indexing was obtained from PDF #01-082-1961 for LSF64 and 01-070-4436 for YSZ.....	108
Figure 6.12 Multiple curvature relaxation cycles of the LSF64/SDC/YSZ sample at 700°C and 750°C between $pO_2=0.21$ and $pO_2=0.021$. The difference in equilibrium curvature levels between the two temperatures is a result of the film-substrate thermal expansion mismatch.	109
Figure 6.13 Representative κ R data of 700°C on reduction shown in Figure 6.14 replotted on a semi-log plot, and showing only one time constant. κ R data of other temperatures showed similar single time constant behavior.	110
Figure 6.14 κ R-measured k values of LSF64/SDC/YSZ across multiple thermal segments at a flow rate of 100 sccm.	111
Figure 6.15 κ R-determined k values of PLD LSF64 thin films compared with those in the literature [47-50] and the sputtered thin films in this work.	112
Figure 6.16 Average equilibrium stress levels of the PLD thin film LSF64/SDC/YSZ as a function of pO_2 and temperature. The dashed lines represent thermal expansion mismatch induced stress, based on coefficient of thermal expansion (CTE) and elastic constants of YSZ and LSF64 available in the literature [193, 215]. 700°C was chosen as the stress-free state in line with the film deposition temperature.	113
Figure 6.17 Chemical stress of the PLD thin film LSF64/SDC/YSZ induced by pO_2 changes between 0.21 and 0.021 as a function of temperature.....	114
Figure 6.18 X-ray photoelectron spectroscopy (XPS) measurements of a PLD LSF64/SDC/YSZ sample.	115
Figure 7.1 (a) Picture of the top surface of a κ R-tested LSF64 porous thick film on a 25.4 mm diameter YSZ substrate, (b) SEM image of the top surface of a LSF film, and (c) a FIB-SEM 3D reconstruction. The film thickness is 5 μ m and aligned in the upward direction.....	119
Figure 7.2 X-ray diffraction of (a) the LSF64 powder after calcination at 1000°C for 1h, (b) a LSF64/YSZ bilayer before κ R testing and (c) a LSF64/YSZ bilayer after κ R testing. XRD peak indexing was performed using LSF64 PDF # 01-082-1961 and YSZ PDF # 01-077-2114.	121
Figure 7.3 Multiple curvature relaxation cycles between $pO_2=0.21$ and $pO_2=0.021$, at 375°C (top) and 325°C (bottom).	122

Figure 7.4 Representative κR data of 325°C on reduction shown in Figure 7.3 replotted on a semi-log plot, and showing only one time constant. κR data of other temperatures showed similar single time constant behavior. 123

Figure 7.5 k measurements (a) under 500 sccm flow rate across multiple thermal segments $\kappa R1$ - $\kappa R5$ and (b) under different flow rates at $\kappa R3$. Errors of k 's are smaller than the symbols. The numbers are in chronological order of experiments, where 1, 3 and 5 are measurements during sample cooling, 2 and 4 are during sample heating. Open and solid symbols denote k measurements with and without flush time limitations, respectively. As indicated by the grayed out region, reliable k measurements could not be obtained above 375°C due to reactor flush time limitations. 124

Figure 7.6 Surface exchange coefficients (averaged over the oxidation and reduction k 's) of the porous thick film LSF64 under 500 sccm for $\kappa R3$ compared to other literature measurements [47, 49, 50, 220], as well as the sputtered and PLD thin films measured in this work. Only k_1 values are shown. 125

Figure 7.7 Estimated LSF64 thickness averaged film stress. Curvature/stress level of the bilayer prior to sintering (at room temperature) was chosen as reference of stress-free state. 126

Figure 7.8 Thickness average film stress of the LSF64 porous thick films compared to representative film stresses as found in the sputtered and PLD thin films measured in this work. 128

Figure 7.9 Chemical stress of spray deposited porous thick films LSF64 between $pO_2=0.21$ and $pO_2=0.021$ as a function of temperature. 129

Figure 7.10 Replot of the Figure 7.9 data on an Arrhenius scale, illustrating two regimes with different activation energies. The dashed lines are linear fits to the data. 130

Figure 7.11 Summary of the chemical stress found in sputtered thin film SP-A, PLD thin film LSF/YSZ and the porous thick film PT-A measured at 500°C and 600°C as a function of inverse grain size (G.S.) 132

Figure 7.12 Summary of the k_1 values found in sputtered thin film SP-A, PLD thin film LSF/YSZ and the porous thick film PT-A measured at 450°C and 500°C as a function of inverse grain size (G.S.) 133

Figure 7.13 Possible surface exchange pathways. The dotted box represents the grain boundary region that induces the sub-525°C chemical stresses observed in this work. 134

KEY TO SYMBOLS AND ABBREVIATIONS

a	particle radius
A_i	area fraction corresponding to a distinct oxygen surface exchange pathway
α_c	coefficient of chemical expansion
α_T	coefficient of thermal expansion (CTE)
AFC	alkaline fuel cell
ASR	area specific resistance
b_E	material dependent constant for Young's modulus-porosity relations
BSCF	$\text{Ba}_{0.5}\text{Sr}_{0.5}\text{Co}_{0.8}\text{Fe}_{0.2}\text{O}_{3-\delta}$
c_0	initial oxygen concentration
c_{bg}	natural background concentration of ^{18}O
c_g	^{18}O concentration of the intentionally enriched atmosphere applied
c_∞	final oxygen concentration
c_o	oxygen concentration
$c(t)$	instantaneous oxygen concentration
$c(x,t)$	instantaneous ^{18}O concentration
c_v	oxygen vacancy concentration
CHP	combined heat and powder
δ	oxygen nonstoichiometry
δ_0	initial film oxygen nonstoichiometry
δ_∞	new-pO ₂ -equilibrated film oxygen nonstoichiometry

Δ	change in
$\Delta_{fitting}$	error for the exponential fitting obtained from Origin ©
D	oxygen diffusion coefficient
D_{chem}	chemical diffusion coefficient
D^*	tracer diffusion coefficient
DMFC	direct methanol fuel cell
d	instantaneous average inter-spot spacing
d_o	initial average inter-spot spacing
DBT	dibutyl phthalate
EC	electronic conductor
ECR	electrical conductivity relaxation
ε_C	chemical strain
ε_{T+C}	dilatometry-measured thermo-chemical strain
e'	electron
EC	electronic conductor
ECR	electrical conductivity relaxation
E_0	Young's modulus of a dense sample b_E is a material dependent constant
E_f	film Young's modulus
E_S	substrate Young's modulus
ϕ	angle of reflection
$\Phi_{v,tot}$	gas flow rate
F	Faraday's constant
FIB-SEM	focused ion beam-scanning electron microscope

Λ_o^*	surface permeability
G_f	activation energy for oxygen vacancy formation
$g(t)$	normalized changes in relaxation experiments
$g(x,t)$	normalized ^{18}O concentration
GDC	gadolinium doped ceria
GNP	glycine-nitrate process
h	k^* / D^*
h_f	film thickness
h_s	substrate thickness
I	current
IC	ionic conductor
IEDP	isotope exchange depth profile
IIE	isothermal isotope exchange
IPA	isopropanol
IT	intermediate temperature
j_o	net flux of oxygen
j_{o_2}	net flux of oxygen molecules
j_{ex}^0	exchange current density
k	surface exchange coefficient
k_{chem}	chemical surface exchange coefficient
k_i	an individual surface exchange coefficient corresponding to a distinct surface exchange pathway
k^*	tracer surface exchange coefficient

k^q	electrically determined surface exchange coefficient
κ	instantaneous bilayer curvature
κ_0	initial bilayer curvature
κ_∞	new- p_{O_2} -equilibrated curvature
κR	curvature relaxation
λ_c	chemical stress
λ_f	film stress
$\bar{\lambda}_{St}$	thickness averaged film stress derived from Stoney's equation
l	sample length
L	l/L_C
L_0	distance between the bilayer and the CCD camera
L_C	characteristic thickness
LSCrM	$\text{La}_{1-x}\text{Sr}_x\text{Cr}_{1-y}\text{M}_y\text{O}_{3-\delta}$
LSF	lanthanum strontium iron oxide
LSF64	$\text{La}_{0.6}\text{Sr}_{0.4}\text{FeO}_{3-\delta}$
LSGM	lanthanum strontium gallium magnesium
LSM	lanthanum strontium manganese oxide
LT	low temperature
μ_0	oxygen chemical potential
$\Delta\mu_{O_2}$	chemical potential change of an oxygen molecule
$\Delta\mu_{O_2}^{\text{int}}$	oxygen chemical potential difference at the gas-solid interface
M_f	film biaxial modulus
M_S	substrate biaxial modulus

M_t	amount of oxygen ions diffused at time t
M_∞	total amount of diffused oxygen ions
MCFC	molten carbonate fuel cell
MIEC	mixed ionic electronic conductor
MOSFET	metal-oxide-semiconductor field-effect transistor
MOSS	multi-beam optical stress sensor
N_a	Avogadro's number
ν_f	film Poisson's ratio
ν_s	substrate Poisson's ratio
ORR	oxygen reduction reaction
P	volume fraction porosity
PAFC	phosphoric acid fuel cell
PDF	powder diffraction file
PEMFC	proton exchange membrane fuel cell
PLD	pulsed laser deposition
pO_2	oxygen partial pressures
ppm	parts per million (i.e. $\times 10^{-6}$)
Q	charge
ρ_f	film relative density
R	ideal gas constant
R_s	electrical surface resistance
σ	total electrical conductivity
σ_i	ionic conductivity

$\sigma(t)$	instantaneous electrical conductivity
σ_0	initial electrical conductivity
σ_∞	final electrical conductivity
$\sigma_{V_O^{\bullet\bullet}}$	oxygen vacancy ionic conductivity
sccm	standard cubic centimeters per minute (i.e. mL/min)
SIMS	secondary ion mass spectroscopy
SOFC	solid oxide fuel cell
SDC	scandium doped ceria
SSC	$\text{Sm}_{0.5}\text{Sr}_{0.5}\text{CoO}_3$
S_V	specific pore surface area
t	time
τ_f	chamber flush time
τ_i	time constant corresponding to a distinct surface exchange pathway
T	temperature
T_r	reactor temperature
T_{STP}	room temperature
TGR	thermo-gravimetric relaxation
TPB	triple phase boundary
V	voltage
V_r	reactor volume
V_m	molar volume
$V_O^{\bullet\bullet}$	oxygen vacancy

V_V	volume fraction porosity
VLSI	very large scale integrated
w_o	thermodynamic factor
XPS	X-ray photoelectron spectroscopy
XRD	X-ray diffraction
YSZ	yttrium stabilized zirconia
8YSZ	$(Y_2O_3)_{0.08}(ZrO_2)_{0.92}$
13YSZ	$(Y_2O_3)_{0.13}(ZrO_2)_{0.87}$
c-YSZ	cubic YSZ
t-YSZ	tetragonal YSZ
z	distance from the substrate midplane

1. Motivation and Project Overview

1.1. Energy Challenges

The demand for energy is essential for humanity, and it continues to rise as industrialization and population growth increase [1]. Fossil fuels, such as coal, petroleum and natural gas, are non-renewable energy sources that provide power for manufacturing, transportation, and other aspects of modern society [1, 2]. Traditional energy production technologies (such as internal combustion engines) have low efficiencies and inherent environmental drawbacks (such as pollution and climate change). Therefore, advanced energy conversion devices are needed to improve energy efficiency and minimize negative environmental impacts.

1.2 Fuel Cells

1.2.1 Applications

Fuel cells are energy conversion devices that directly convert chemical energy into electricity, and are recognized as a superior energy conversion technology to internal combustion engines and coal-fired power plants because of their higher efficiency and lower environmental impacts [3]. They find applications in portable devices (such as auxiliary power units), stationary power generation (such as power plants and uninterruptible power supplies) and transportation (such as fuel cell electric vehicles). The past five years have seen a steady growth of both shipments and megawatts of fuel cell systems, as shown in *Figure 1.1*.

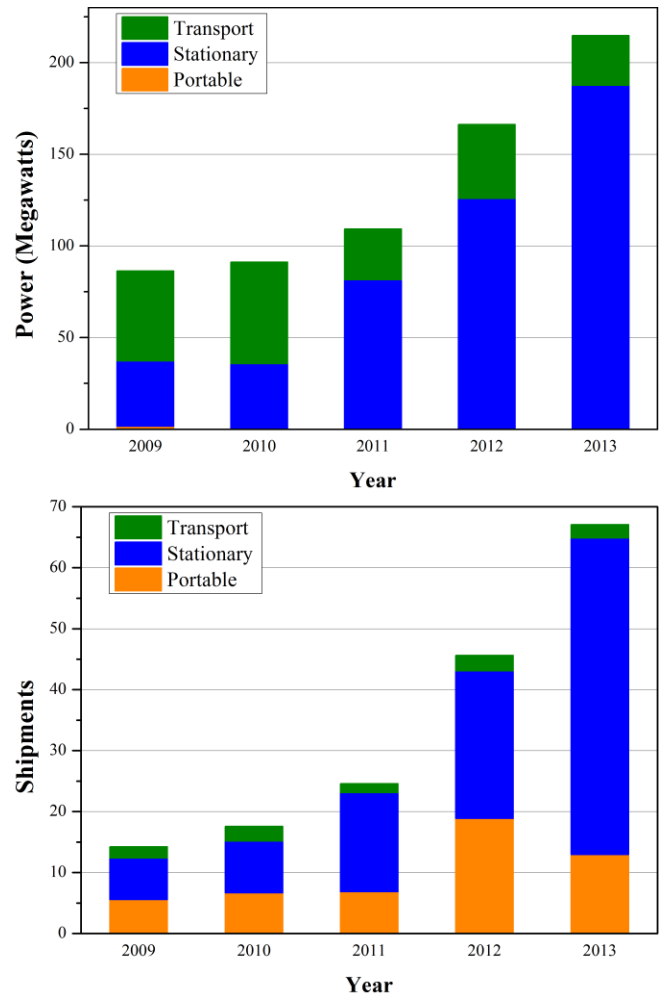


Figure 1.1 Fuel cell market growth from 2009 to 2013. [4]

1.2.2 Types of Fuel Cells

Based on the nature of the electrolyte, fuel cells can generally be categorized into proton exchange membrane fuel cells (PEMFCs), direct methanol fuel cells (DMFCs), alkaline fuel cells (AFCs), phosphoric-acid fuel cells (PAFCs), molten-carbonate fuel cells (MCFCs) and solid-oxide fuel cells (SOFCs). A comparison of the mobile ions, operating temperatures, electrode reactions, efficiencies and practical problems between these fuel cell types is summarized in *Table 1*. Among these devices, SOFCs have the highest efficiencies (45% to 65% for stand-alone applications and 70-90% for combined heat and power (CHP) applications [5,

6]) and fuel flexibility. As it remains challenging to produce and store hydrogen in a sustainable and cost-effective way [7, 8], SOFCs can serve as a bridge from the current hydrocarbon-based economy to a hydrogen or biofuel based economy (using hydrocarbons fuels derived from fossil fuels, biomass and solid waste) while using existing infrastructure (such as the natural gas distribution grid) [9].

Table 1 Selected features of different types of fuel cells. [10-13]

Type	Common Electrolyte	Operating Temperature	Fuel	Mobile Ion	Typical Electrode Reactions	Electrical/ CHP Efficiency	Practical Problems
PEMFC	Nafion™	70–110 °C	H ₂	(H ₂ O) _n H ⁺	$\frac{1}{2}O_{2(g)} + H^+ + 2e^- \rightarrow H_2O$ $H_{2(g)} \rightarrow 2H^+ + 2e^-$	40-50%/NA	H ₂ O management; CO intolerant
DMFC	Nafion™	70–110 °C	CH ₃ OH	(H ₂ O) _n H ⁺	$\frac{3}{2}O_{2(g)} + 6H^+ + 6e^- \rightarrow 3H_2O$ $CH_3OH + H_2O \rightarrow CO_2 + 6H^+ + 6e^-$	40-50%/NA	H ₂ O management; CO intolerant
AFC	Aqueous KOH	100–250 °C	H ₂	OH ⁻	$\frac{1}{2}O_{2(g)} + H_2O_{(g)} + 2e^- \rightarrow 2OH^-$ $H_{2(g)} + 2OH^- \rightarrow 2H_2O_{(g)} + 2e^-$	50%/NA	CO ₂ intolerant
PAFC	H ₃ PO ₄	150–250 °C	H ₂	H ⁺	$\frac{1}{2}O_{2(g)} + H^+ + 2e^- \rightarrow H_2O$ $H_{2(g)} \rightarrow 2H^+ + 2e^-$	40%/NA	liquid electrolyte leaks
MCFC	(Na,K) ₂ CO ₃	500–700 °C	H ₂ Cs, CO	CO ₃ ²⁻	$\frac{1}{2}O_{2(g)} + CO_{2(g)} + 2e^- \rightarrow CO_3^{2-}$ $H_{2(g)} + CO_3^{2-} \rightarrow H_2O + CO_{2(g)} + 2e^-$	50%/80%	Longer start-up; corrosive electrolyte
SOFC	(Zr,Y)O _{2-δ}	600–1000 °C	H ₂ , H ₂ Cs, CO	O ²⁻	$\frac{1}{2}O_{2(g)} + 2e^- \rightarrow O^{2-}$ $H_{2(g)} + O^{2-} \rightarrow H_2O + 2e^-$	45- 65%/90%	Longer start-up; high temperature degradation

1.2.3. SOFC Overview

1.2.3.1 Components and Operating Principles

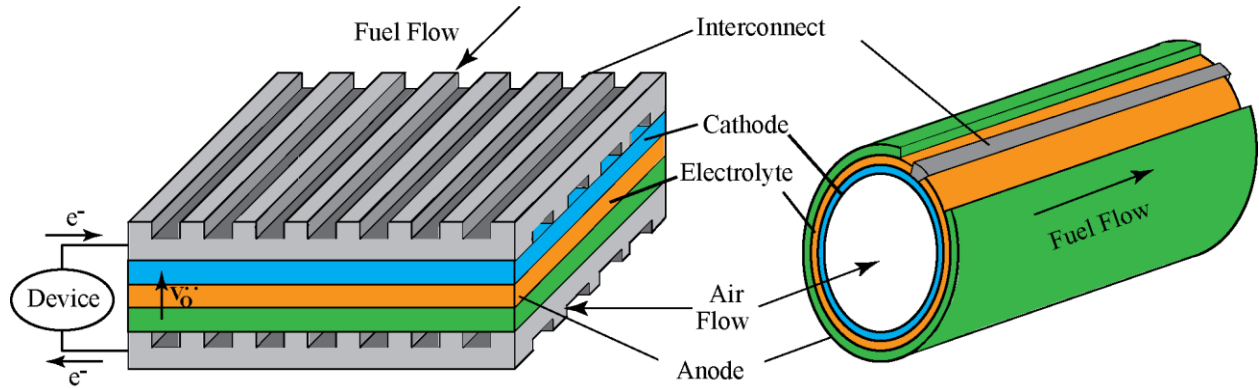
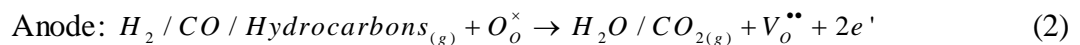
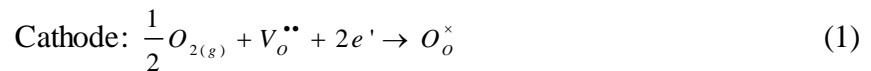


Figure 1.2 Planar (left) and tubular (right) design of SOFCs and their components.

Figure 1.2 schematically shows the two common SOFC cell designs. The planar design is easier for stacking flat plates, while the tubular design is easier for sealing. The four essential components of a single SOFC are the cathode, electrolyte, anode and interconnect. During SOFC operation, oxygen molecules (1) react with electrons and incorporate into the material structure as oxygen ions at the cathode, (2) migrate through the cathode, electrolyte and anode, and (3) combine with fuel to produce water and/or carbon dioxide at the anode, while releasing electrons that go through the external circuit and reduce more oxygen molecules. The cathodic and anodic half reactions are spatially separated and can be written using Kroger-Vink notation as [14]:



The oxygen ion conducting capability of the solid electrolyte allows for direct fuel flexibility in SOFC, compared to some of the other fuel cells (eg. PEMFCs, AFCs) that require hydrogen as an exclusive fuel source, or the use of external reformers.

1.2.3.2 Materials and Requirements of SOFC Components

1.2.3.2.1 Cathode

The SOFC cathode is required to have a high electronic conductivity, a high oxygen surface exchange coefficient, and a high activity for oxygen reduction. Traditionally, an SOFC cathode is composed of a porous layer of electronic conductor (EC), such as Pt or Lanthanum Strontium Manganese oxide (LSM), on a dense, ionic conducting (IC) electrolyte, such as yttrium stabilized zirconia (YSZ) [10, 15]. Alternatively, a two-phase, porous EC-IC composite on a dense IC electrolyte can be used to provide better ionic conductivity [3, 15]. In either scenario, the oxygen reduction reaction (ORR) takes place at the triple-phase-boundary (TPB), where the gas, EC and IC phases meet. The resulting oxygen ions are then transported through the IC phase to the electrolyte.

In order to increase the surface area over which the ORR reaction can occur, mixed ionic electronic conductors (MIECs) have been introduced to replace EC-IC cathodes [15]. The capability of conducting both electrons and ions in a single material allows the oxygen to be transported through the bulk of the cathode particles, thus extending the reaction sites over a much larger surface compared to the triple phase boundary width. Numerous studies have been conducted in the past two decades to develop MIEC oxides that considerably improve SOFC performance [16-20]. By optimizing dopants and/or doping levels in perovskite-type oxides such as $\text{Ln}_{1-x}\text{Sr}_x\text{Fe}_{1-y}\text{Co}_y\text{O}_{3-\delta}$ (where $\text{Ln}=\text{La, Sm, Nd, etc.}$) [21], $\text{Sm}_{0.5}\text{Sr}_{0.5}\text{CoO}_3$ (SSC) [22] and $\text{Ba}_{0.5}\text{Sr}_{0.5}\text{Co}_{0.8}\text{Fe}_{0.2}\text{O}_{3-\delta}$ (BSCF) [23], lower interfacial resistance and overpotential in the cathode

can be achieved. These MIECs can be used in single-phase porous cathodes, micron-sized MIEC-IC composites, or infiltrated nano-composite cathodes [24]. Thin film MIEC microelectrodes with well-defined geometries have also been made to elucidate oxygen reduction kinetics [25, 26].

1.2.3.2.2 Anode

Ni-YSZ cermets are commonly used as SOFC anodes as they provide high electronic and ionic conductivity, as well as chemical/thermal compatibility with YSZ electrolytes. For the same reason as SOFC cathodes, however, the catalytic anode reactions are limited to TPB regions in SOFC anode cermets.

Recent studies have investigated oxide based MIEC materials such as $\text{La}_{1-x}\text{Sr}_x\text{Cr}_{1-y}\text{M}_y\text{O}_{3-\delta}$ (LSCrM, where M is a transition metal such as V, Cr, Fe, Mn, Co, Ni, Cu, etc), as replacements for Ni-based anodes [27-32]. These materials have excellent redox stability and catalytic activity toward methane reforming. They also have good electrical conductivity and mechanical stability in reducing atmospheres, which are all required for SOFC anodes.

1.2.3.2.3 Electrolyte

The primary requirement for SOFC electrolytes is sufficiently high ionic conductivity and minimal electronic conductivity. Considering a target value of the area specific resistance (ASR) of $0.15 \text{ } \Omega\text{cm}^2$, and the practical lower limit of electrolyte thickness of $\sim 15 \text{ } \mu\text{m}$ by traditional colloidal fabrication techniques, the ionic conductivity must be greater than 0.01 S cm^{-1} [3], as shown in *Figure 1.3*. This requires an operating temperature $\geq 700^\circ\text{C}$ for traditional YSZ electrolytes. In order to reduce the operating temperatures to $\sim 500^\circ\text{C}$ (a temperature desirable to minimize degradation and allow the use of cheaper metallic interconnect components), other electrolytes, such as gadolinium doped ceria (GDC) and lanthanum strontium

gallium Magnesium (LSGM), have been introduced and extensively studied [33-38]. In addition to their high conductivity at intermediate/low temperatures, the thermal expansion coefficients of GDC and LSGM are chemically compatible with other SOFC components, such as stainless steel interconnects [3] and perovskite electrodes [33]. As shown in *Figure 1.3*, the ionic conductivity can generally be regarded as a figure of merit for material selection, as it largely dictates the minimum SOFC operating temperature based on practical requirements of fabrication and operation. However, other factors such as phase stability under operating conditions and chemical compatibility with other SOFC components must also be taken into consideration. $\text{Bi}_2\text{V}_{0.9}\text{Cu}_{0.1}\text{O}_{5.35}$, for example, is unstable under reduced atmosphere at the anode side despite its high conductivity [3].

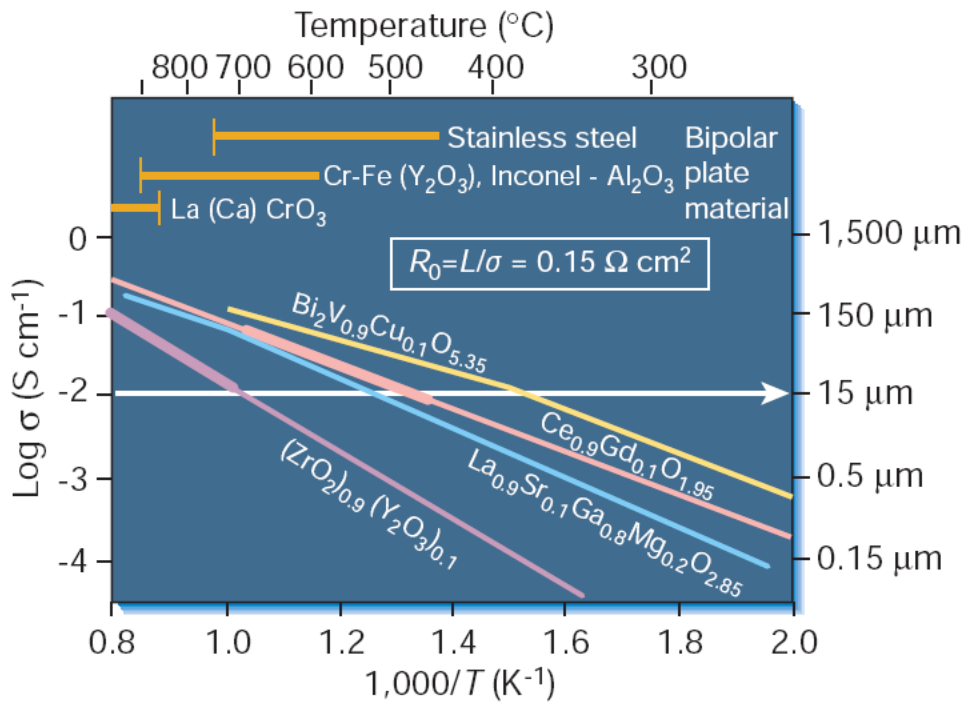


Figure 1.3 Ionic conductivity of common SOFC electrolyte materials. Practical application requires area specific resistance (ASR) values $\leq 0.15 \text{ } \Omega \text{ cm}^2$. Therefore, a minimum target conductivity value of 0.01 S cm^{-1} is necessary so inexpensive colloidal fabrication techniques producing dense electrolyte films $15 \text{ } \mu\text{m}$ thick can be used. This helps dictate the necessary SOFC operating temperature. This figure was reproduced from Ref. [3].

1.2.3.2.4 Interconnect

Interconnect materials have to be electronically conductive and also serve as sealants to spatially separate the fuel and air chambers. For reasons similar to those mentioned above, they also need to be chemically stable during SOFC operating conditions, as well as chemically/thermo-mechanically compatible with other SOFC components. Sub-600°C operating temperatures would allow the use of alloys, such as stainless steel, that are cheaper and easier to machine [10]. This, coupled with the reduced starting times and improved thermodynamic efficiencies are driving the development of low temperature (i.e. <600°C) SOFCs.

1.3 Technological Progress of SOFCs

The first operating SOFC was developed in 1937 by Bauer and Preis [39]. Since then, SOFC research and development activities have made significant progress in terms of lowering SOFC operating temperatures from 1000°C to the intermediate temperature (IT) (650°C to 800°C) range, and even down to the low temperature (LT) (<600°C) regime, while maintaining a desirable power density of >1W/cm² [3, 9, 40, 41]. SOFC lifetimes have also been extended to more than 5 years [42, 43]. These major advances are largely attributed to the development of new materials, the advancement of fabrication techniques, and the optimization of electrode microstructures [9, 41, 42, 44-46].

1.4 Current Challenges at the SOFC Cathode

Despite the encouraging improvements made during the past two decades, many technological challenges still remain in SOFCs. These challenges usually involve competing situations: (1) high operating temperatures enhance the oxygen surface exchange and diffusion kinetics but increases the long-term degradation of SOFC components, and (2) low operating

temperatures improve the long-term stability but aggravates electrode polarization losses. One of the key issues that has driven research but remains poorly understood is the reaction kinetics of oxygen reduction at the cathode. This can be demonstrated by scattered, sometimes conflicting experimental results on nominally identical bulk and thin film samples made with different fabrication techniques [47-50]. Contradictory observations on the effect of lattice strain on the oxygen surface exchange kinetics of MIEC oxides also exists in the literature [51, 52].

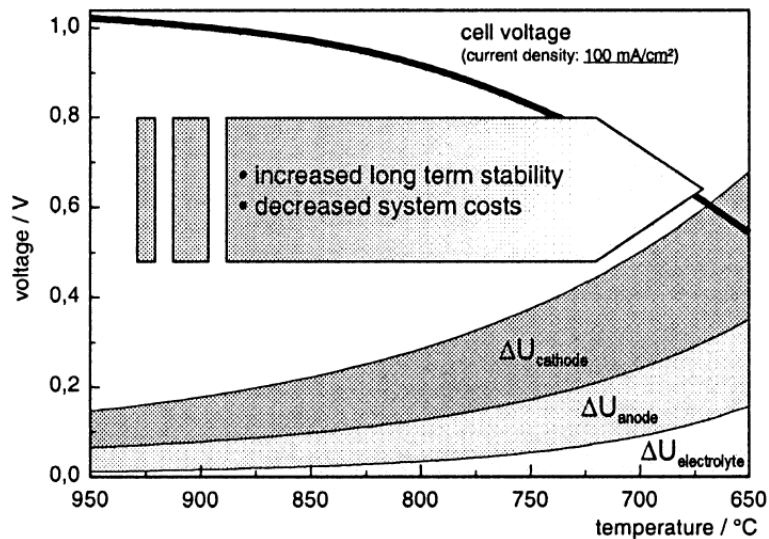


Figure 1.4 Voltage drop of a typical SOFC operated at 100 mA/cm^2 and various temperatures [53].

As depicted in *Figure 1.4*, among the three main components of SOFCs, the cathode is the most resistive part of the cell. The overpotential losses due to oxygen transport at the cathode are significant, especially when the operating temperature is lowered in order to reduce cost and maintain long-term mechanical/chemical integrity.

In general, oxygen transport can generally be considered as a combination of the following elementary steps: (1) oxygen gas diffusion, (2) oxygen surface exchange at the gas-solid interface, (3) oxygen ion diffusion through the MIEC cathode, and (4) oxygen

incorporation across the cathode/electrolyte interface. Multiple models [54, 55] show that for traditional SOFC cathodes, oxygen surface exchange is the most resistive process.

1.5 Hypothesis and Aim of this Work

Due to its important role in determining SOFC cathode performance, oxygen surface exchange has attracted great attention in the literature in terms of its fundamental mechanisms, how to measure it, and how to improve it. However, there are great discrepancies/contradictions in the literature, and debate exists on the oxygen surface exchange rates of even the most common MIEC materials. In $\text{La}_{0.6}\text{Sr}_{0.4}\text{FeO}_{3-\delta}$ (LSF64), for instance, chemical oxygen surface exchange coefficient (k_{chem}) discrepancies of up to 5 orders of magnitude are common at identical temperature and oxygen partial pressure conditions [47, 50]. Similar discrepancies have been observed for other MIEC materials such as reduced cerium oxide [56-59], lanthanum strontium cobaltite [60-62] and lanthanum strontium cobalt iron oxide [63-66].

In fact, many of the literature studies, despite investigating materials of interest with the same chemical compositions, prepare and measure the samples using different techniques. These various techniques can introduce large variations in microstructure, stress states, electrode impacts, etc. These complicating effects are hypothesized to contribute to the large surface exchange discrepancies seen in the literature. **The objective of the work presented in this thesis is to evaluate the hypothesis that (1) reliable surface exchange measurements of MIEC films can be obtained via a curvature relaxation technique (κR) based on the mechano-chemical coupling of these materials, and (2) that factors such as preparation technique and/or microstructure affect surface exchange.**

Of the following chapters, *Chapter 2* reviews the mechano-chemical coupling in SOFC materials and the traditional oxygen surface exchange coefficient measurement techniques. *Chapter 3* provides the theoretical development of the curvature relaxation (κ R) technique and summarizes the experimental methods used throughout this work. *Chapter 4* reports the mechano-chemical behavior of bulk $\text{La}_{0.6}\text{Sr}_{0.4}\text{FeO}_{3-\delta}$ (LSF64), an archetypal MIEC material. *Chapters 5, 6 and 7* use the κ R technique to experimentally investigate the surface exchange coefficients and stress of LSF64 films fabricated by sputtering, pulsed laser deposition, and colloidal spray deposition, respectively. Finally, *Chapter 8* provides a summary of the important conclusions that can be drawn from this work.

2 Literature Review

2.1 Mechano-Chemical Coupling in Solid Oxide Fuel Cell Materials

In order to better understand how oxygen surface exchange in MIEC materials can be investigated using the curvature relaxation technique developed in this work, a general background summary on mechano-chemical coupling in electroceramics is provided in this chapter.

2.1.1 Strain in Electro-ceramic Devices

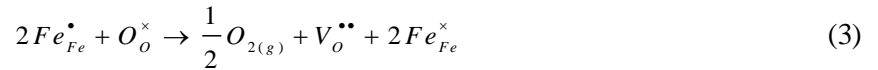
The functional ceramics used in energy, automotive and chemical applications are usually nonstoichiometric, ionically or electronically conductive, and capable of exchanging electrons or ions with the environment. These unique features allow them to: a) catalyze the removal of NO_x , CO and unreacted hydrocarbons from combustion gas streams [67], b) sense oxygen partial pressures for fuel-efficient engine operation [68], c) catalyze the dissociation of H_2O or CO_2 for alternative fuel production [69, 70], e) separate oxygen for gas purification applications [71], and f) serve as catalytically-active SOFC electrode materials [27], among other uses.

During fabrication and operation, many electronic/ionic devices undergo undesirable stress development, which is oftentimes induced by mechanical, thermal or electrochemical effects (or combinations thereof). In Li ion batteries, for example, the charge-discharge operations rely on the lithiation and delithiation of the electrodes. This repeated compositional change result in repeated volume changes that may cause large stress development and irreversible structural changes/failure [72]. In SOFCs, different components are usually manufactured under particular temperature/pressure conditions and subsequently used at others.

This can leave inherent stress caused by the constrained sintering of individual components or the thermal expansion mismatch between neighboring components. Due to the relatively high operating temperature and the varying oxygen partial pressure across an SOFC device, rapid start-up and cool-down can also cause SOFC mechanical failure [73-75].

2.1.2 Chemical Expansion in MIEC Materials

Due to the presence of multivalent cations and accommodating crystal structures, many MIEC materials can alter their bulk oxygen vacancy concentration (c_v) by changing their cation oxidation state. In bulk lanthanum strontium iron oxide (LSF), for example, these changes can be summarized via the defect reaction:



at temperatures below 625°C and oxygen partial pressures (pO_2 's) ranging from 1 to $\sim 1 \times 10^{-7}$ atm [76]. In addition to altering cation and anion defect concentrations, these internal redox reactions can affect overall lattice strain. For instance, in lanthanum strontium ferrite [49, 77], cerium oxide [78-80], lanthanum strontium cobaltite [81, 82], lanthanum strontium chromate [83], lanthanum manganate [84], lanthanum strontium cobalt iron oxide [82, 85], barium strontium cobalt iron oxide [86], strontium iron titanate [87], and other MIEC materials, the operation of reactions such as Equation (3) results in lattice expansion as the oxygen nonstoichiometry (δ) increases. This mechano-chemical coupling can be summarized as a chemically induced strain (ε_c) given as:

$$\varepsilon_c = \left. \frac{\Delta l}{l} \right|_T = \alpha_c \Delta \delta \quad (4)$$

where l is sample length, T is the temperature, and α_c is defined as the chemical expansion coefficient. δ is related to the oxygen vacancy concentration via:

$$c_v = \delta N_a / V_m \quad (5)$$

where N_a is Avogadro's number and V_m is the molar volume. As shown in *Table 2*, many MIEC oxides exhibit positive α_c values, meaning that increases in δ result in overall expansion of the lattice.

Table 2 Chemical expansion coefficients of common MIEC materials

Material	Measured Temperature (°C)	α_c
$Ce_{0.9}Gd_{0.1}O_{1.95-\delta}$	700-900	0.14 [88, 89] †
CeO_2	800	0.10 [80, 89]
$La_{0.3}Sr_{0.7}FeO_{3-\delta}$	650-875	0.017-0.047 [90]
$La_{0.6}Sr_{0.4}Co_{0.8}Fe_{0.2}O_{3-\delta}$	700-900	0.031 [91, 92]
$La_{1-x}Sr_xCoO_{3-\delta}$ $0.2 \leq x \leq 0.8$	600-900	0.023-0.024 [91, 93]
$SrFe_{1-x}Ti_xO_{3-\delta}$ $0.25 \leq x \leq 0.7$	23	0.03 [94]
$Ba_{0.6}Sr_{0.4}Co_{0.8}Fe_{0.2}O_{3-\delta}$	600-900	0.026-0.016 [95]
$La_{1-x}Sr_xCrO_{3-\delta}$ $0.16 \leq x \leq 0.3$	1000	0.024 [96]
$LaMnO_{3-\delta}$	600-1000	0.024 [84]
† For $0 \leq \delta \leq 0.05$. Although nonlinear above 0.05, α_c is linear for $\Delta\delta \leq 0.01$ [88]		

As is shown by the many studies listed in *Table 2*, the chemical expansion provides additional strain compared to pure thermal expansion and can lead to challenging stress development across the device. Understanding this combined “thermo-chemical” effect is therefore critical in material selection and system design.

2.1.3 Utilizing Mechano-chemical Coupling

Notwithstanding the challenges resulting from chemical expansion, it is also possible to take advantage of mechano-chemical coupling to improve material properties and device performance through strain engineering.

Previous experimental and computational studies have suggested that stress can affect the ionic defect concentrations [97-99], oxygen ion diffusion [100], carrier mobility [101-103], free-surface dopant/impurity buildup [104-106], catalytic activity [107], and oxygen surface exchange kinetics [100, 101, 106, 108-110] of electrochemically active ceramics. As detailed in *Section 2.3.6*, many of these properties can be positively impacted with intentionally induced tensile strain.

While bulk or micro-scale materials can sustain limited stress and therefore are more susceptible for degradation and failure, nano-scale thin films can withstand stress levels on the order of several GPa [111]. One of the main objectives of this work is the utilization of mechano-chemical coupling and the development of the curvature relaxation technique to measure MIEC films fabricated by various techniques, as detailed in Chapters 5-7.

2.2 Oxygen Surface Exchange and its Measurement

As mentioned in *Chapter 1*, high oxygen surface exchange kinetics is the key to the activity of nano-composite and thin film MIEC cathodes, and therefore the overall performance and commercial viability of low temperature SOFCs. This section provides a literature review on the definitions, derivations and traditional measurement techniques of oxygen surface exchange coefficients.

2.2.1 The Characteristic Thickness

In comparison to traditional EC cathode materials, MIEC cathodes are advantageous in that oxygen ion diffusion through the bulk is significantly enhanced. On the other hand, in MIEC materials, oxygen surface exchange, which also contributes to the overall oxygen transport in the cathode, can become rate limiting. It is therefore important to distinguish between these two processes and identify the conditions where they control the oxygen transport kinetics. The characteristic thickness, L_c , indicates the dimension where a sample is under mixed control (i.e. both bulk and surface). A given sample with thickness l , is essentially limited by surface exchange when $l/L_c < 100$ and limited by bulk diffusion when $l/L_c > 100$ [112]. The characteristic thickness can be expressed as the ratio of oxygen diffusivity over the surface exchange coefficient [112]:

$$L_c = \frac{D}{k} \quad (6)$$

2.2.2 The Different Types of Oxygen Surface Exchange Coefficients

2.2.2.1 Chemical Exchange Coefficient

When the environmental pO_2 changes by a small amount, ΔpO_2 , a corresponding oxygen chemical potential change $\Delta\mu_O$, and a net flux of oxygen, j_o , occur at the surface, These two parameters are related by:

$$j_o = 2j_{O_2} = 2j_{ex}^0 \frac{\Delta\mu_{O_2}}{RT} = 4j_{ex}^0 \frac{\Delta\mu_O}{RT} \quad (7)$$

where j_{O_2} is the net flux of oxygen molecules, j_{ex}^0 is the exchange current density, $\Delta\mu_{O_2}$ is the chemical potential change of an oxygen molecule at the surface. Given the thermodynamic factor derived by Weppner et al. [113] as:

$$w_O = \frac{1}{RT} \frac{\partial \mu_O}{\partial \ln c_O} \quad (8)$$

j_O can be rewritten as:

$$j_O = \frac{4 j_{ex}^0 w_O}{c_O} \Delta c_O \quad (9)$$

where Δc_O is the oxygen concentration change across the surface. Assuming first order kinetics, the rate constant of the surface reaction, k_{chem} , is then given by:

$$k_{chem} = \frac{j_O}{\Delta c_O} = \frac{4 j_{ex}^0 w_O}{c_O} \quad (10)$$

Or alternatively,

$$k_{chem} = \left(\frac{j_O}{\Delta \mu_O} \right) \frac{RT w_O}{c_O} \quad (11)$$

where the constant $(j_O / \Delta \mu_O)$ is termed as the surface permeability, Λ_o^* [114]. This expression defines the rate constant for the ambipolar diffusion of oxygen (i.e. the combined diffusion of oxygen vacancies and electrons) through an MIEC material, in the absence of an external electrical circuit.

2.2.2.2 Tracer Exchange Coefficient

If a sample is at chemical but not isotopic equilibrium (i.e. $j_o = 0$), tracer surface exchange occurs. The rate constant in this situation is termed as the tracer surface exchange coefficient (k^*) and is defined as:

$$k^* = \Lambda_o^* \frac{RT}{c_o} \quad (12)$$

Unlike k_{chem} which depends on the ambipolar diffusion of both electrons and oxygen vacancies, k^* is only dependent on the diffusion of oxygen vacancy species, since there is no change in the electronic concentration within the material.

2.2.2.3 Electrically Determined Surface Exchange

If a sample is under a small, steady-state applied electrical field and only ionic current is allowed through the sample, an electrically determined surface exchange coefficient defined as:

$$k^q = \Lambda_o^q \frac{RT}{c_o} \quad (13)$$

Like k_{chem} , during a k^q measurement, changes in the electronic concentration are occurring. However, since these concentration gradients are not generated by or relieved by electron movement within the material (these small electron concentration gradients are extremely imposed), the resulting oxygen flux is not dependent on electron diffusion through the material.

Although relationships exist between the three types of k 's [66], their different definitions imply the different situations they are applied to, their magnitudes (even for the same sample) can be very different, and usually different techniques are used to measure them, as detailed in the following section.

2.2.3 Literature Oxygen Surface Exchange Coefficient Measurement Techniques

As summarized in *Table 3*, there are a number of measurement techniques used for determining the various surface exchange coefficients discussed in *Section 2.2.1*. Due to various instrumental and/or mechanistic restrictions, some of the techniques have a limited temperature range, some require electrodes to be deposited on the sample (which can complicate accurate k measurements, especially in low-conductivity films), some are *ex-situ* techniques that may not reflect sample behavior under operating conditions, and some need voluminous samples so that resolvable signals can be obtained. An ideal film k measurement technique would be electrode-free, *in-situ* and suitable for both thin film and thick film analysis across a large temperature window for as many materials as possible. As discussed in *Section 3.1*, the curvature relaxation technique developed in this work is such a technique.

Table 3 Methods for determining surface exchange coefficients and a comparison of their advantages/disadvantages.

Method	Oxygen Permeation	Ionic Conductivity	Tracer Depth Profiling	Conductivity Relaxation	Isothermal Isotope Exchange	Electrical Titration	Gravimetric Relaxation	Optical Relaxation	Strain Relaxation	Curvature Relaxation
Measures the:	surface dominated through-sample surface resistivity	partial ionic conductivity using blocking electrodes or impedance spectroscopy to obtain R_S	c_o depth profile of a sample equilibrating to changes in O_2 isotope ratios	electrical conductivity of a sample equilibrating to pO_2 changes	gas composition around a sample equilibrating to changes in O_2 isotope ratios	I or V of a cell coupled to a sample equilibrating to electrically imposed c_o changes	weight change of a sample equilibrating to pO_2 changes	optical properties of a sample equilibrating to pO_2 changes	lattice strain of a sample equilibrating to pO_2 changes	lattice strain of a sample equilibrating to pO_2 changes
Reference	[115]	[116]	[117]	[118]	[119]	[120]	[121]	[122]	[123]	This Work
Type of k	k_{chem}	k^q	k^*	k_{chem}	k^*	k_{chem}	k_{chem}	k_{chem}	k_{chem}	k_{chem}
Pros	Electrode-free, Suitable for <i>in situ</i> analysis below 500°C	Suitable for <i>in situ</i> analysis	Electrode-free	Suitable for <i>in situ</i> analysis	Electrode-free	Suitable for <i>in situ</i> analysis below 500°C	Electrode-free, Suitable for <i>in situ</i> thick film analysis	Electrode-free, suitable for <i>in situ</i> analysis	Electrode-free, suitable for <i>in situ</i> analysis	Electrode-free, suitable for <i>in situ</i> analysis
Cons	Glass seals prevent higher temperature experiments	Requires electrode	High vacuum prevents <i>in situ</i> measurements	Requires electrode	Voluminous samples are required to noticeably alter gas composition	Requires electrode. Glass seals prevent higher temperature experiments	Voluminous samples are required to noticeably alter weight	Requires optical defects influenced by a change in defect concentration	Only probes the lattice response	Cannot separate the behavior of different local parts of the film

Symbol Key: k^q , k^* and k_{chem} = electrically determined, tracer determined, and chemically determined k , respectively. R_S = oxygen exchange surface resistance, R = ideal gas constant, T = temperature in Kelvin, F = Faraday's Constant, I = current, and V = voltage.

2.2.3.1 Oxygen Permeation

Oxygen permeation experiments can be used to measure the diffusion and surface exchange coefficients of a dense ceramic membrane. During the experiment, the membrane is typically sealed in a chamber and exposed to different pO_2 's on each side of the sample. The oxygen flux, j_{O_2} , can then be calculated from the gas flow rates, the membrane area, and the oxygen leakage. When the membrane is much thinner than L_c , such that the surface reactions dominate over bulk diffusion and therefore become rate limiting, the surface kinetics is related to the oxygen flux by [115]:

$$j_{O_2} = -j_{ex}^0 \frac{\Delta\mu_{O_2}^{int}}{RT} \quad (14)$$

where $\Delta\mu_{O_2}^{int}$ is the oxygen chemical potential difference at the interface calculated from the difference in pO_2 . The surface exchange coefficient is then determined using the relationship [124]:

$$k_{chem} = \frac{4j_{ex}^0}{c_o} = -\frac{4j_{O_2} RT}{c_o \Delta\mu_{O_2}^{int}} \quad (15)$$

where c_o is the oxygen ion concentration estimated from the stoichiometry of the oxide membrane.

2.2.3.2 Ionic Conductivity

Partial ionic conductivity can be measured by using blocking electrodes or impedance spectroscopy [125] to measure the ionic area-specific surface resistance, R_s . As seen in Steele [126] and Nicholas et al. [127], assuming the exchange current density is uniform across the

sample, the product of R_s and the ionic conductivity, σ_i , can be related to the characteristic thickness:

$$R_s \sigma_i = L_c = D / k \quad (16)$$

Employing the Nernst-Einstein Equation (2.6), it follows that:

$$k^q = \frac{RT}{4F^2 R_s c_o} \quad (17)$$

where k^q is the electrically determined surface exchange coefficient defined in Equation (13), and c_o is the oxygen ion concentration estimated from the stoichiometry of the oxide membrane.

Using Equation (17), one can therefore measure k^q in an ionic conductivity experiment by measuring R_s and c_o from the impedance arc width and height, respectively.

2.2.3.3 Isotope Exchange Depth Profiling

The Isotope Exchange Depth Profile (IEDP) method can be used to determine both the oxygen tracer surface exchange coefficient (k^*) and the oxygen tracer diffusion coefficient (D^*) [117]. In this technique, a dense specimen is pre-annealed in an atmosphere with normal oxygen isotopic abundance. $^{18}\text{O}/^{16}\text{O}$ isotope exchange experiments are then carried out in an atmosphere with enriched $^{18}\text{O}_2$. After sample quenching, the ^{18}O concentration profile is analyzed by Secondary Ion Mass Spectroscopy (SIMS). k^* and D^* can be extracted from least-square fit of the concentration data to a solution of Fick's Second Law [117]:

$$g(x, t) = \frac{c(x, t) - c_{bg}}{c_g - c_{bg}} = \operatorname{erfc}\left(\frac{x}{2\sqrt{D^*t}}\right) - \left[\exp(hx + h^2 D^* t) \operatorname{erfc}\left(\frac{x}{2\sqrt{D^*t}} + h\sqrt{D^*t}\right) \right] \quad (18)$$

where $g(x, t)$ is the normalized ^{18}O concentration, $c(x, t)$ is the instantaneous ^{18}O concentration, c_{bg} is the natural background concentration of ^{18}O , c_g is the ^{18}O concentration of the intentionally enriched atmosphere applied, t is time and $h = k^*/D^*$.

2.2.3.4 Electrical Conductivity Relaxation

The Electrical Conductivity Relaxation (ECR) method measures the electrical conductivity changes of dense samples subjected to step changes in pO_2 . Both the oxygen chemical surface exchange coefficient (k_{chem}) and the oxygen tracer diffusion coefficient (D_{chem}) can be determined by fitting the conductivity profile to the Fick's Second Law solution for a planar sheet under non-steady-state surface evaporation conditions [128]. Assuming the oxygen ion mobility is constant during the experiment (therefore allowing the oxygen concentration and the measured conductivity to be linearly correlated) [129],

$$g(t) = \frac{\sigma(t) - \sigma_0}{\sigma_\infty - \sigma_0} = \frac{C(t) - C_0}{C_\infty - C_0} = 1 - \sum_{n=1}^{\infty} \frac{2L^2 \exp(-4\beta_n^2 D_{\text{chem}} t / l^2)}{\beta_n^2 (\beta_n^2 + L^2 + L)} \quad (19)$$

where $g(t)$ is the normalized conductivity change, $\sigma(t)$ and $c(t)$ are the instantaneous conductivity and oxygen concentration, respectively. The subscripts 0 and ∞ denote initial and final properties, respectively. l is the sample thickness, β_n is a root of the following equation:

$$\beta_n \tan \beta_n = \frac{lk_{\text{chem}}}{2D_{\text{chem}}} = \frac{l}{2L_c} \quad (20)$$

A mathematical derivation of the above solution is detailed in Appendix A. When $l \ll L_c$, the oxygen transport is controlled by the surface, and Equation (19) can be reduced to:

$$g(t) = \frac{\sigma(t) - \sigma_0}{\sigma_\infty - \sigma_0} = \frac{C(t) - C_0}{C_\infty - C_0} = 1 - \sum_{i=1}^n A_i \exp\left(-\frac{tk_i}{l}\right) \quad (21)$$

where each individual oxygen surface exchange coefficient k_i corresponds to a distinct oxygen surface exchange pathway [130-132].

2.2.3.5 *In situ* Isothermal Isotope Exchange

The Isothermal Isotope Exchange (IIE) technique integrates the principles of IEDP and ECR, and provides an *in situ* method to measure surface exchange kinetics of powders and bulk samples [63]. It takes a similar approach to ECR, but instead measures the relaxation of oxygen concentration in the gas stream following an abrupt change in pO_2 (it is therefore an indirect measurement of oxygen concentration in the sample). The fitting equation then takes the form:

$$g(t) = \frac{c(t) - c_0}{c_\infty - c_0} = 1 - \sum_{n=1}^{\infty} \frac{6L^2 \exp(-\beta_n^2 Dt / a^2)}{\beta_n^2 [\beta_n^2 + L(L-1)]} \quad (22)$$

$$\beta_n \cot \beta_n + L - 1 = 0 \quad (23)$$

$$L = \frac{k^* a}{D^*} = \frac{a}{L_c} \quad (24)$$

where a is the radius of the particle modeled as a sphere. When using this technique to measure k^* , nanoparticles are generally used to ensure that $a \ll L_c$ and oxygen surface exchange dominates.

2.2.3.6 Electrical Titration

In electrical titration measurements, a solid-state electrochemical cell is coupled to the sealed atmosphere surrounding a sample. In response to a small potential step in the

electrochemical cell, an alteration in the atmospheric pO_2 is created, which, in turn, induces a corresponding oxygen vacancy concentration and therefore a current relaxation in the sample [120, 133, 134]. The surface exchange coefficient is then obtained by fitting a solution to Fick's Second Law:

$$I(t) = Q \sum_{n=1}^{\infty} \frac{8L^2 D \exp(-4\beta_n^2 Dt / l^2)}{l^2 [\beta_n^2 + L^2 + L]} \quad (25)$$

where Q is the total charge passed as t approaches infinity, l is the sample thickness, β_n is a root of the following equation:

$$\beta_n \tan \beta_n = L \quad (26)$$

where L is defined by:

$$L = \frac{lk_{chem}}{2D_{chem}} = \frac{l}{2L_c} \quad (27)$$

2.2.3.7 Thermogravimetric Relaxation

Thermo-Gravimetric Relaxation (TGR) measures the weight change of a sample in response to a step pO_2 change [121]. Since the oxygen is the only species exchanging with the atmosphere, and the oxygen content of the sample is linearly related to the sample weight, the time constant for this process can then be calculated for the determination of k_{chem} and D_{chem} using Equations (19)-(20) where the conductivity is replaced by the sample weight.

2.2.3.8 Optical Absorption Relaxation

The optical absorption relaxation technique is based on the fact that oxygen concentration changes in some MIEC materials are directly correlated with the changes of cation oxidation

state (such as $\text{Fe}^{4+}/\text{Fe}^{3+}$), and that certain cations have absorption bands corresponding to visible light [135]. During these experiments, a monochromatic light passes through the sample sealed in a controlled atmosphere. As a stepwise oxygen partial pressure change is applied, the change of the absorption coefficient is recorded by a spectrometer (typically a CCD camera). The time constant for this process can then be calculated for the determination of k_{chem} and D_{chem} using Equations (19)-(21) where the conductivity is replaced by the absorption coefficient.

2.2.3.9 Strain Relaxation by X-ray Diffraction

Recently, a time-resolved X-ray Diffraction (XRD) technique has been developed to measure surface exchange kinetics of epitaxial thin films subjected to $p\text{O}_2$ changes [123]. This methodology is based on the chemical expansion of these materials accompanied with the variation of transition metal ion oxidation state that result in changes in the lattice parameter. Assuming linear chemical expansion (i.e. the lattice strain is linearly proportional to the oxygen defect concentration, c), the time constant for this process can then be calculated for the determination of k_{chem} and D_{chem} using Equations (19)-(21) where the conductivity is replaced by the film lattice parameter.

2.3 The Factors Governing Oxygen Surface Exchange

With the development of new materials and optimized microstructures, researchers have measured the surface exchange coefficients of a variety of MIEC materials, using the techniques listed in *Section 2.2.3*. Many studies have systematically investigated factors (such as material composition, surface structure, crystal orientation, mechanical strain, etc.) that govern the oxygen surface exchange kinetics. However, due to varying fabrication and characterizing techniques adopted among different research groups, it is often difficult to perform direct

comparison among different data sets and draw clear conclusions. Therefore, great ambiguity still remains in terms of the k 's of many SOFC materials. A brief review and some examples of the various proposed factors affecting surface exchange are given below.

2.3.1 Material Composition (Dopants and Doping Level)

The perovskite crystal structure $ABO_{3-\delta}$ is known for its phase stability when large A-site and/or B-site substitutional cations are present and a significant amount of oxygen vacancies are generated. This enables a wide range of dopants and doping levels to be selected to tailor the oxygen nonstoichiometry, and subsequently the surface exchange kinetics.

As an archetypal family of A-site doped perovskite-type materials, $La_xSr_{1-x}BO_{3-\delta}$ have been extensively studied (B=Mn, Fe, Ti, Ga, etc.) [47, 136-138]. In order to maintain charge neutrality, the substitution of La^{3+} by divalent cation Sr^{2+} is generally accompanied by the generation of oxygen vacancies or electron holes, as described by the following defect reactions:



and $La_xSr_{1-x}BO_{3-\delta}$ materials are therefore generally p-type semiconductors. In general, a higher vacancy concentration corresponds to faster oxygen diffusion and surface exchange in that more vacancy sites facilitate the absorption and transport of oxygen ions [117]. In addition, a higher electronic conductivity is usually correlated with faster oxygen surface exchange in that more electronic carriers facilitate surface reactions that involves charge transfer in oxygen molecules/ions [15]. This is demonstrated by literature studies [139, 140] in which an increase of

the Sr content is associated with an increased oxygen surface exchange coefficient and/or decreased oxygen surface exchange activation energy.

B-site doped perovskites, such as $\text{La}_x\text{Sr}_{1-x}\text{Mn}_{1-y}\text{Co}_y\text{O}_{3-\delta}$, have also been systematically studied [117]. Similar trends are observed in that increasing Co site fraction increases the surface exchange coefficient. This can be understood by the fact that an oversized Co cation actually increases the opening between A and B cations where oxygen ions pass through (i.e. lowers the saddle point energy [141]). This can explain the slow oxygen surface exchange and diffusion of Mn-rich perovskites and the fact that $\text{La}_x\text{Sr}_{1-x}\text{MnO}_{3-\delta}$ is essentially an electronic conductor.

The composition $\text{Ba}_{0.5}\text{Sr}_{0.5}\text{Co}_{0.8}\text{Fe}_{0.2}\text{O}_{3-\delta}$ has also attracted great attention and was suggested as a high-performance cathode due to its low ASR of 0.055–0.071 Ωcm^2 at 600 °C [23]. The measured surface exchange coefficients of BSCF films are 1-3 orders of magnitude larger than contemporary, much studied lanthanum strontium cobaltites [142]. These desirable properties are attributed to mixed occupation of Ba and Sr on the A-site that provides unusually large oxygen nonstoichiometry (δ) that can exceed 0.5 without destabilizing the perovskite phase [23, 143-145].

2.3.2 Oxygen Partial Pressure

The $p\text{O}_2$ dependence of the surface exchange coefficient has been studied for a variety of perovskite materials, such as $\text{La}_{1-x}\text{Sr}_x\text{FeO}_{3-\delta}$ and $\text{La}_{1-x}\text{Sr}_x\text{CoO}_{3-\delta}$ using electrical conductivity relaxation [47, 146, 147]. It has been reported that a power law exists between k_{chem} and $p\text{O}_2$ ($k_{\text{chem}} \sim [p\text{O}_2]^n$, where n is between 0.65 and 0.85 for $\text{La}_{1-x}\text{Sr}_x\text{FeO}_{3-\delta}$ [47]) across the temperature range of 600-950 °C, indicating that k_{chem} decreases with decreasing $p\text{O}_2$. Since one would expect that lower $p\text{O}_2$ corresponds to higher oxygen vacancy concentration that would increase k , as

seen in Equation (3), it is suggested that electronic species dominate the surface exchange rate in that electron transfer at the oxide surface can be the rare-limiting step [148], especially at low pO_2 .

2.3.3 Surface and Interface Structure

A great number of studies have demonstrated that the cathode surface structure plays a key role in oxygen surface exchange. For instance, Imanishi and co-workers [149] used pulsed laser ablation techniques to epitaxially grow LSM and LSC thin films on single crystal YSZ substrates with different crystal orientations and found that the impedance spectroscopy-measured surface resistance of the films for the (111) surface was less than the (110) surface, which was less than the (100) surface. Yan *et al.* [150] also measured the surface exchange rates of LSM film with these orientations, but on $SrTiO_3$ substrates. Varying k values (1×10^{-6} to 6.5×10^{-5} cm/s) and activation energies 0.8 to 1.2 eV were found. Tsuchiya *et al.* studied the different surface exchange coefficients of textured ((111) and (110)) and polycrystalline ceria films grown by molecular beam synthesis and electron beam evaporation, respectively. The polycrystalline film showed five times larger k values than the textured films, but had very similar activation energy. This indicates that both films had similar rate limiting steps and the different surface exchange kinetics was attributed to (1) limited oxygen adsorption site at ((111) and (110) planes, and (2) the accumulation of oxygen vacancies at grain boundaries of polycrystalline films.

2.3.4 Grain Size

As shown in ion conductors such as doped zirconia and ceria [151-155], grain size can also dramatically alter mass and charge transport properties. This is explained by a space charge effect in which significant accumulation of electron carriers and depletion of the oxygen

vacancies occur near the grain boundary. One can therefore engineer the conductivity by changing the grain size, as the width of the space charge layer is on the order of a few nanometers, which is comparable to the nanostructured grains. Sase *et al.* studied the effect of grain size on the surface resistance of $\text{La}_{1-x}\text{Sr}_x\text{CoO}_{3-\delta}$ thin films and observed ~5 times performance enhancement for the nanosized film (30–50 nm grain size) compared to sub-micron-sized film (300–500 nm grain size) [156].

2.3.5 Electronic structure

The impact of the electronic structure on surface exchange kinetics has been extensively studied. The d-band model has been successful in describing the metal catalysts surface reactivity, but is not a good descriptor for oxide catalysts [157, 158]. The oxygen 2p band center energy [159] and carrier density of minority electronic species in the conduction band [160] have recently been proposed to describe the surface catalytic activity of oxides, but neither have been found to be universally applicable [161]. In $(\text{La,Sr})\text{CoO}_3$ and $(\text{La,Sr})\text{MnO}_3$ thin films at high temperature, higher density of states is observed in tensile strained films compared to compressive strained films, indicating easier charge transfer at surfaces under tension.

2.3.6 Strain

Both theoretical and experimental studies have shown that stress can affect electronic and ionic properties. In fact, strain engineering has been a common practice in the semiconductor industry, where tensile strained (up to 1GPa [162]) silicon [163] and indium gallium arsenide [164] for Metal-Oxide-Semiconductor Field-Effect Transistor (MOSFET) and Very Large Scale Integrated (VLSI) computer logic chips have achieved threefold or fourfold electronic conductivity. These enhancements can generally be understood by strain-induced electronic

band-wrapping, Jahn-Teller distortion band splitting, and/or inter-band carrier redistribution [162].

In addition, strain has been proposed to significantly impact the ionic defect concentrations [97-99], electronic structure [165], oxygen ion diffusion [100], carrier mobilities [101-103], free-surface dopant/impurity buildup [104-106], catalytic activity [107], and oxygen surface exchange kinetics [100, 101, 106, 108-110] of electrochemically active ceramics. When thin film geometries are adopted, stresses can easily be induced from film-substrate lattice mismatch [52, 100, 166], and stress level in the order of several GPa can be maintained [111]. It is generally understood that tensile strain promotes greater oxygen vacancy concentration, mobility and oxygen surface coverage [166]. That said, excessive tensile strain is reported to cause negative effects in that oxygen ion mobility is inhibited due to cation-oxygen bonding [166]. It may also be possible to improve surface exchange properties by controlling the amount of stress-induced cation surface segregation.

2.3.7 Dislocations

In addition to strain effects, misfit dislocations in ionic thin films, which act as a stress relaxation mechanism, have also been suggested to impact the ion conduction kinetics [51]. Sillassen *et al.* [167] attributed the 1000 times enhancement of conductivity to the fast conduction along epitaxial YSZ|MgO interfaces compared to bulk conductivity, especially at temperatures below 350°C, which suggested the positive effects of misfit dislocations. Li *et al.*, [168] however, observed a 5 times greater conductivity of YSZ|Gd₂Zr₂O₇ films compared to YSZ|Ceria films. The YSZ|Gd₂Zr₂O₇ films had less lattice mismatch strain and were controlled so that they were dislocation free, as opposed to the YSZ|Ceria films. Further investigation on

the mechanisms of stress relaxation through dislocation formation is needed to understand the experimental inconsistencies and optimize strain enhanced transport properties.

3 Experimental Methods

3.1 The Bilayer Curvature Relaxation Technique

3.1.1 Theoretical Background

For a mechano-chemically active film constrained by an invariant, mechano-chemically inactive substrate, changes in film oxygen vacancy concentration result in film stress and film strain that alter the bilayer curvature [169, 170]. Films with thicknesses less than $\sim 1/1000^{\text{th}}$ of the thickness of an elastically deforming substrate [171] and less than $1/100^{\text{th}}$ of the characteristic thickness (L_c) [112], maintain uniform through-thickness stress and oxygen vacancy concentrations; even as the films equilibrate with their surroundings. Therefore, the temporal changes to oxygen vacancy concentration of a sufficiently thin film are solely controlled by k , and similar to Equation (21) for ECR experiments, k can be extracted from the curvature response of a bilayer equilibrating to small step changes in pO_2 using the solution for oxygen transport into/out of a surface-controlled (Equation (21)):

$$g(t) = \frac{C - C_0}{C_\infty - C_0} = \frac{\delta - \delta_0}{\delta_\infty - \delta_0} = 1 - \sum_{n=1}^n A_n \exp\left(-\frac{tk_n}{h_f}\right) \quad (30)$$

where h_f denotes the film thickness.

The difference between the curvature relaxation (κR) and the electrical conductivity relaxation (ECR) techniques is that the latter uses electrical conductivity changes to measure $\Delta\delta$, while the former uses film stress changes. Specifically, for a film thickness to substrate thickness ratio $\leq \sim 1/1000$, the film stress (λ) is related to the bilayer curvature (κ) via Stoney's Equation:

$$\bar{\lambda}_{st} = \frac{\kappa E_s h_s^2}{6 h_f (1 - \nu_s)} \quad (31)$$

where E_s is the substrate Young's modulus, h_s is the substrate thickness, and ν_s is the substrate Poisson's ratio [171]. To determine the relationship between κ and δ for a linear elastic bilayer, Hooke's Law and Equation (4) can be combined with Equation (31) to yield:

$$\Delta \delta = \left[\frac{E_s h_s^2 (1 - \nu_f)}{6 \alpha_c \rho_f E_f h_f (1 - \nu_s)} \right] \Delta \kappa \quad (32)$$

where ρ_f , ν_f , and E_f are the film relative density, the film Poisson's ratio, and the film Young's modulus, respectively. Assuming the product in parentheses remains constant and non-zero during a small step change in atmospheric pO_2 , Equation (30) can be rewritten using Equation (32) as:

$$\frac{\kappa - \kappa_0}{\kappa_\infty - \kappa_0} = 1 - \sum_{n=1}^n A_n \exp\left(-\frac{tk_n}{h_f}\right) \quad (33)$$

Equation (33) indicates that the κR method can reliably be used to measure k as long as h_f is known, the film and substrate both deform elastically, the substrate is compositionally invariant to pO_2 changes, oxygen vacancy concentration changes are the only stress relaxation mechanism in the film, and the film chemical expansion coefficient and elastic properties are roughly constant over each pO_2 step [172-175]. As shown in Equation (33), quantitative knowledge of the film's elastic properties and/or chemical expansion coefficient is not required to measure k in κR experiments. That said, as shown in Equation (32), a large film chemical expansion coefficient, a large film Young's Modulus, and a small film Poisson ratio are desirable

because they result in large, easily-resolvable, pO_2 -induced equilibrium bilayer curvature changes.

For porous films, the effective film thickness can be expressed as the ratio of volume fraction of pores to the specific pore surface area of the film, and a fitting equation equivalent to Equation (33) can be used [176]:

$$g(t) = \frac{\kappa - \kappa_0}{\kappa_\infty - \kappa_0} = 1 - \sum_{n=1}^n A_n \exp\left(-\frac{k_n t}{\frac{1 - V_v}{S_v}}\right) \quad (34)$$

where V_v is the volume fraction porosity, S_v is the specific pore surface area, and the other symbols have their previously defined meanings, to extract k 's by fitting the ECR response of porous films with average particles sizes $\ll L_C$ [177].

3.1.2 Experimental Setup

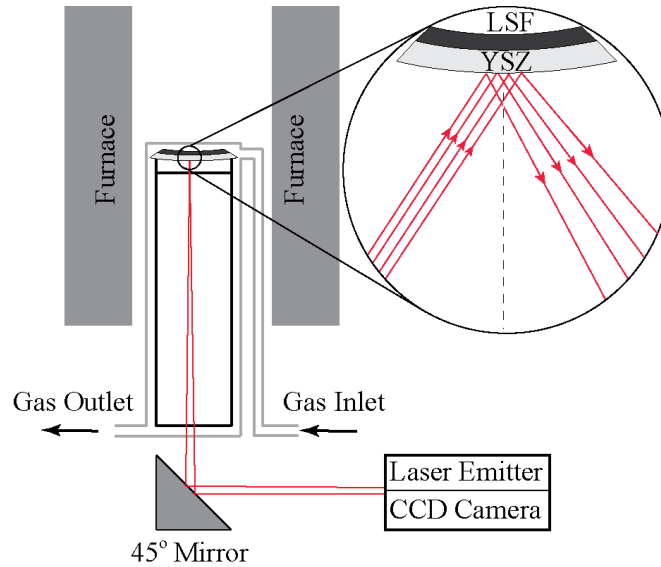


Figure 3.1 Curvature relaxation measurement apparatus schematic.

Figure 3.1 schematically shows the experimental setup for the bilayer κR technique. The multi-beam optical stress sensor (MOSS) measures the bilayer curvature based on the change of spacing between neighboring laser spots, as well as geometric parameters of the system through the following relationship [178]:

$$\kappa = \left(\frac{\cos \phi}{2L_0} \right) \left(1 - \frac{d}{d_0} \right) \quad (35)$$

where ϕ is the angle of reflection, L_0 is the distance between the bilayer and the CCD camera, d and d_0 are the instantaneous and initial average inter-spot spacing, respectively. A snapshot of the multibeam laser array is shown in *Figure 3.2*. Values for d_0 and the ratio in the first set of parentheses were obtained by taking MOSS measurements on flat and $\kappa=0.1 \text{ m}^{-1}$ calibration mirrors placed in the sample location prior to κR experiments.

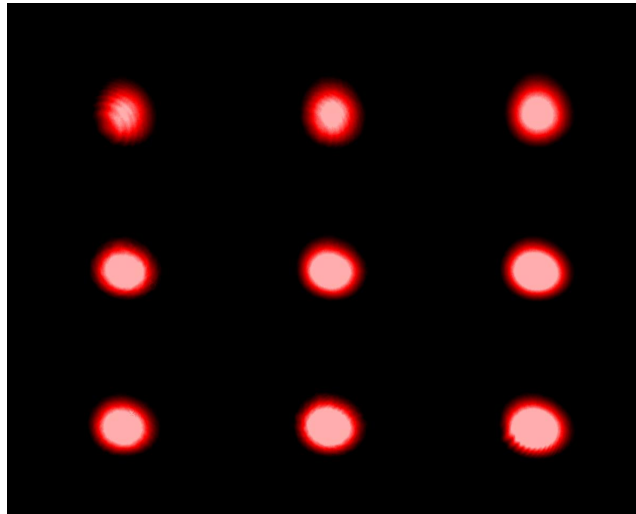


Figure 3.2 A 3×3 array of laser spots detected by the MOSS CCD camera

The multi-beam feature in MOSS analysis is beneficial in that sample vibrations have little effect on the accuracy of curvature measurements, as the inter-spot spacing remains unchanged due to the entire array of spots moving together during vibrations. Individual beam

positions are determined by the kSA MOS software package (k-Space Associates, Inc.) using a Gaussian peak profile fitting of the spot intensity. It is therefore important to have circular spots and a symmetric intensity profile, the maximum of which is at the center.

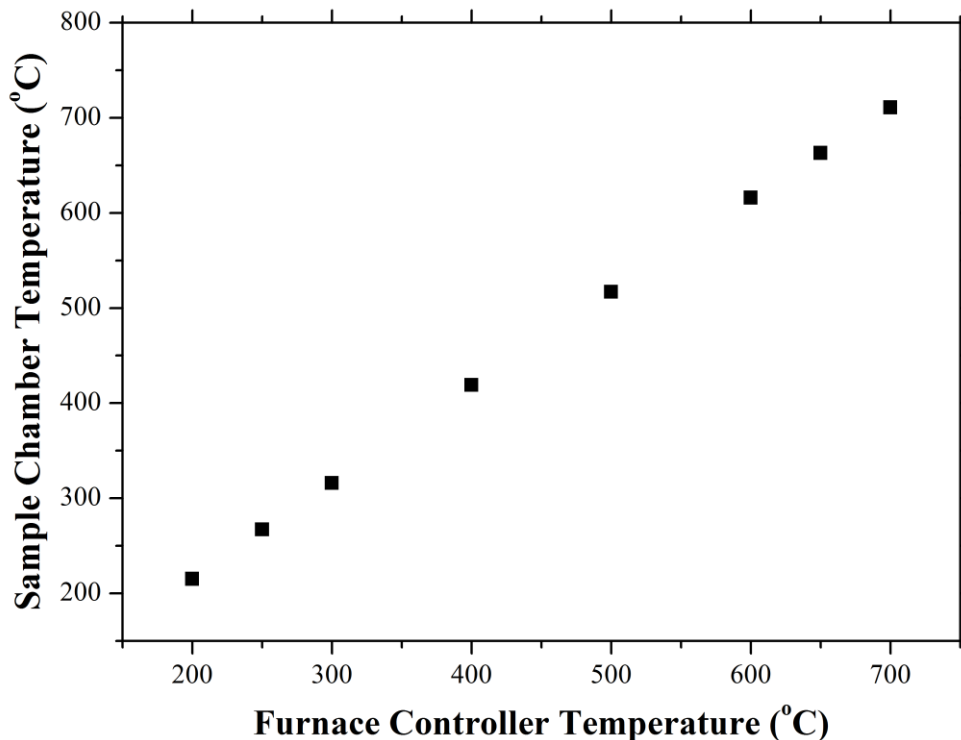


Figure 3.3 Temperature calibration of the furnace controller between 200°C and 700°C using actual sample chamber temperature measurements.

To observe *in-situ* curvature relaxations at controlled temperature and atmosphere, the bilayer samples were placed on a platform inside a sealed quartz reactor in a vertically mounted tube furnace. The outer cover of this quartz reactor contained a three meter long spiral of 1/4” quartz tubing (1.2 meters of which was in the furnace hot zone) used to preheat the incoming gas. The furnace controller temperature was calibrated by placing a thermocouple located within the sample chamber, as shown in *Figure 3.3*. On average, the deviation between the two temperature readings was 15°C, which is the offset value used throughout the κR experiments in this work. A Swagelok® four-way valve (not shown) was used to switch the gas flow of

different pO_2 's. An oxidizing to reducing oxygen partial pressure ratio of 10 (a standard pO_2 step size used in ECR experiments [179, 180]) was utilized in this work. Previous studies on lanthanum strontium cobaltite have shown that the assumption of linear exchange kinetics implicit in Equations (30) and (33) is valid for oxidizing to reducing oxygen partial pressure ratios less than 20 [147].

3.1.3 Flush Time Considerations

The reactor volume was determined to be ~ 10 mL through the flush-time dominated κR experiments detailed in *Chapter 5*. Specifically, for a continuously stirred reactor, a characteristic time (τ_f) needed to flush a reactor with volume (V_r) has the following relationship [181]:

$$\tau_f = \frac{V_r T_{STP}}{\Phi_{v,tot} T_r} \quad (36)$$

where $\Phi_{v,tot}$ is the gas flow rate, T_r is the temperature of the reactor and T_{STP} is the room temperature. By analyzing the apparent activation energy of a κR -measured k values on an Arrhenius plot and comparing that to the apparent activation energy of Equation (36), one can determine the reactor flush time. As detailed in *Chapter 5* on sputtered LSF|YSZ, the flush time dominated κR experiments had an activation energy of 0.07 eV at temperatures from 625-725°C with a gas flow rate of 100 sccm. A ~ 10 mL sample chamber volume (a reactor size commonly used in ECR experiments) [181, 182] was then determined using Equation (36).

As show in [181], only 1.83% of the original gas volume in the reactor is left after a time lapse of $4 \tau_f$. Therefore, the total duration of each curvature relaxation experiment was at least 5 times the largest fitted time constant (τ_i):

$$\tau_i = k_i / h_f \quad (37)$$

for that particular relaxation. k values were then determined by performing a least-squares regression fit of Equation (33) to normalized curvature relaxation data using the Origin © computer program.

3.1.4 Film Stress Measurement

As shown by the Stoney's Equation, Equation (31), in addition to measuring k , the κR technique also simultaneously measures the film stress as a function of temperature and oxygen partial pressure (pO_2), without requiring electronic current collecting layers or knowledge of the elastic properties of the MIEC film [183]. This provides important measurements of chemical expansion and how it is correlated with external effects like temperature, pO_2 and stress.

For dense thick films that are thicker than $1/1000^{\text{th}}$ of the substrate, stresses can be rigorously extracted from bilayer curvature measurements using a modified version of Stoney's Equation [178]:

$$\lambda(z) = M_f (\varepsilon_m + \varepsilon_0 - \kappa z) \quad (38)$$

where

$$\varepsilon_m = \frac{\kappa h_s^2 M_s}{6 h_f M_f} \left(1 + \frac{h_f}{h_s} \right)^{-1} \left[1 + 4 \frac{h_f M_f}{h_s M_s} + 6 \frac{h_f^2 M_f}{h_s^2 M_s} + 4 \frac{h_f^3 M_f}{h_s^3 M_s} + \frac{h_f^4 M_f^2}{h_s^4 M_s^2} \right] \quad (39)$$

$$\varepsilon_0 = -\varepsilon_m \frac{h_f M_f}{h_s M_s} \left(1 + \frac{h_f^3 M_f}{h_s^3 M_s} \right) \left[1 + 4 \frac{h_f M_f}{h_s M_s} + 6 \frac{h_f^2 M_f}{h_s^2 M_s} + 4 \frac{h_f^3 M_f}{h_s^3 M_s} + \frac{h_f^4 M_f^2}{h_s^4 M_s^2} \right]^{-1} \quad (40)$$

z is the distance from the substrate midplane, M_f is the film biaxial modulus defined as

$E_f / (1 - \nu_f)$, M_s is the substrate biaxial modulus defined as $E_s / (1 - \nu_s)$, and the other variables

have their previously defined meanings [178, 184].

With some algebraic manipulation, Equations (38)-(40) can be rewritten as:

$$\lambda(z) = \bar{\lambda}_{st} \left[\frac{a}{b} - \frac{M_f h_f}{b M_s h_s} \left(1 + \frac{h_f^3 M_f}{h_s^3 M_s} \right) - \frac{6 h_f}{h_s^2} \frac{M_f}{M_s} z \right] \quad (41)$$

where

$$a = \left(1 + 4 \frac{h_f}{h_s} \frac{M_f}{M_s} + 6 \frac{h_f^2}{h_s^2} \frac{M_f}{M_s} + 4 \frac{h_f^3}{h_s^3} \frac{M_f}{M_s} + \frac{h_f^4}{h_s^4} \frac{M_f^2}{M_s^2} \right) \quad (42)$$

$$b = \left(1 + \frac{h_f}{h_s} \right) \quad (43)$$

As expected, film to substrate thickness ratios $\leq 1:1000$ cause Equation (41) to collapse to Equation (31), and the thinner the film the less z-variation in the film stress.

Although Equations (41)-(43) were used to estimate the film stresses in this work, calculations made using Equations (41)-(43) indicate that dense and porous LSF64 films even several microns thick are well described by Equation (31) when deposited on commercially available 200 μm thick single crystal YSZ substrates. For instance, stress predictions made using Equations (41)-(43), literature 500°C LSF64 [172] elastic property data in air, and YSZ [185] elastic property data in air indicate that dense, 5 μm thick LSF64 films on 200 μm thick YSZ single crystal wafers have film stresses that range from 97.4% of $\bar{\lambda}_{st}$ at the film-air interface, to 97.7% of $\bar{\lambda}_{st}$ at the film-substrate interface.

3.1.5 Substrate Selection

One side polished single crystal substrates were used for this work because they have high reflectivity on one side and prevent secondary reflections on the other.

25.4 mm diameter, circular substrates were chosen in this work to avoid edge effects that may complicate the stress distribution in the bilayer and the curvature measurements [178, 186]. As discussed in Freund and Suresh [178], these edge effects only become significant when film thickness to width ratios are >50 . For reference, a $5 \mu\text{m}$ film on a 25.4 mm diameter wafer has a film thickness to width ratio of 0.0002. In addition, the 25.4 mm diameter is large enough so that the approximately 6 mm by 6 mm MOSS laser array shown in *Figure 3.2* is smaller than the sample, but the sample is small enough to fit into a quartz sample reactor with minimal chamber volume.

To prevent complications during curvature relaxation measurements, the substrates were chosen to be chemically insensitive to the gas composition, chemically compatible with the film, have high yield stress to ensure a purely elastic response, have known elastic properties, and maintain phase stability in the temperature measurement range.

3.1.6 Error Analysis

In order to analyze the measurement error of the surface exchange coefficients, standard error propagation rules were utilized [187]:

$$(\Delta f(x_1, x_2, x_i, \dots, K))^2 = \sum \left(\frac{\delta f}{\delta x_i} \right)^2 (\Delta x_i)^2 \quad (44)$$

where x_i 's are independent variables, K is a constant, and Δ quantities represent absolute errors.

Therefore, based on Equations (33) and (34) for surface exchange coefficients and Equation (44), the relative error of k 's can be estimated to be:

$$\frac{\Delta k}{k} = \sqrt{(\Delta_{fitting})^2 + \left(\frac{\Delta h_f}{h_f}\right)^2} \quad (45)$$

and

$$\frac{\Delta k}{k} = \sqrt{(\Delta_{fitting})^2 + \left(\frac{\Delta V_V}{V_V}\right)^2 + \left(\frac{\Delta S_V}{S_V}\right)^2} \quad (46)$$

for dense and porous films, respectively. $\Delta_{fitting}$ is the error for the exponential fitting obtained from Origin ©. Given the maximum errors of fitting (6.4%), film thickness (1.2%), porosity (5%) and surface area (5%), the k errors in this work are estimated to be less than 10%.

Similarly, based on the Stoney's Equation (31) and assuming the elastic properties are constants without error, the relative error of the film stress measurement can be estimated by:

$$\frac{\Delta \lambda}{\lambda} = \sqrt{\left(\frac{\Delta \kappa}{\kappa}\right)^2 + \left(\frac{\Delta h_s}{h_s}\right)^2 + \left(\frac{\Delta h_f}{h_f}\right)^2} \quad (47)$$

As shown by Stoney's Equation (31), a smaller substrate thickness results in greater bilayer sample curvature changes, and hence improves the signal resolution. Even though the manufacturer specified radius of curvature resolution is 15 km, the practical error in the curvature measurements is approximately $5 \times 10^{-5} \text{ m}^{-1}$ ($\Delta \kappa$) due to environmental vibration and gas convection. A commercially available 200- μm -thick YSZ substrate with 250-nm-thick film results in a stress resolution that can be as small as 0.38 MPa.

3.1.7 Summary

In summary, the κR technique is one of the few experimental methods to allow *in-situ* k measurements on both MIEC thin films and thick films, as shown in *Table 3*. Further, this technique has the benefit of being an electrode-free method that avoids the necessity of interdigitated electrodes for low conductivity films measurements that may: (1) cause

complicated stress distributions in an underlying MIEC film, (2) cause preferential oxygen incorporation at the MIEC-electrode-air triple phase boundary, resulting in a k measurement that reflects the properties of the triple-phase-boundary and not the MIEC surface, and/or (3) chemically react with the underlying MIEC film.

3.2 Sample Preparation

3.2.1 Powder Processing

LSF64 powder was synthesized using the glycine-nitrate process (GNP) [188]. Stoichiometric metal nitrates (>99% pure, Alfa Aesar) were dissolved in Milli-Q deionized water and mixed with glycine powder (>99% pure) in a 1:1 ratio. The solution was then transferred to a stainless steel vessel and placed on a hot plate pre-heated to 350°C to transform it on to an ash-like powder after combustion. The powder was calcined in an alumina crucible (AD-998, Coorstek) at 1000°C for 1 hour at 5°C/min heating and cooling rates.

3.2.2 Sputtering Target Preparation

A 76 mm diameter LSF64 sputtering target was prepared by hot pressing GNP-prepared LSF64 powder at 60 MPa in a nitrogen atmosphere using a graphite die. The hot pressing temperature was ramped to 300°C at 20°C/min, held there for 30 minutes, ramped to 600°C at 20°C/min, ramped to 1200°C at 10°C/min, held there for 120 minutes, and finally ramped to room temperature at a nominal cooling rate of 10°C/min in a graphite die. The as-pressed target was polished down to 600 grit SiC sandpaper to reduce surface roughness and remove surface contamination.

3.2.3 Sputter Deposition

In preparation for LSF64 thin film deposition, YSZ substrates were mounted in a high vacuum (1×10^{-5} Pa, total base pressure) sputtering chamber using double-sided tape on the underside of the substrates. LSF64 was subsequently DC plasma-sputtered onto the polished side of these substrates using an Ar background pressure of 210 Pa, and a deposition rate of 1.2-3 nm/min at room temperature. The deposition thickness was controlled using a quartz crystal thickness monitor with a tooling factor previously calibrated with a scanning electron microscope LSF64 film thickness analysis on previously deposited samples.

3.2.4 Pulsed Laser Deposition (PLD)

As a common physical vapor deposition technique, pulsed laser deposition provides an effective way to fabricate epitaxial films by laser pulsing the target material [189]. In this work, PLD LSF64 thin films on 13 mol% YSZ substrates were prepared by Dr. William Chueh and his research group at Stanford University. The substrates were pre-annealed at 1100°C for 1 hour. The PLD film deposition temperature was 700°C and the oxygen partial pressure was set at 5 mTorr. The estimated deposition rate was 0.002 nm/pulse. PLD thin films were also deposited on the polished side of the substrates.

3.2.5 Colloidal Spray Deposition

Porous LSF64 thick films were manufactured using spray deposition followed by sintering. First, colloidal suspension was produced by ball milling 6.5 g of LSF64 powder, 0.3 g of dibutyl phthalate (DBT) dispersant, 52.5 g of 3 mm YTZ® tetragonal yttria stabilized zirconia milling media (Tosoh USA), and ~18 mL of isopropanol (IPA) in a 60 mL polyethylene bottle at 70 rpm for 24 hours. After ball milling, the suspension was diluted with additional IPA to a 1 weight percent solids loading, 1/6 of which was spray deposited using an airbrush (Iwata-Medea)

onto the rough side of one-side-polished, 200- μm -thick, single crystal, (100)-oriented $(\text{Y}_2\text{O}_3)_{0.13}(\text{ZrO}_2)_{0.87}$ (YSZ) substrates (University Wafer) preheated to 100°C . The roughness of the unpolished side of the YSZ substrates was approximately $0.5\ \mu\text{m}$. To produce bonding between the film and the substrate, the porous film was sintered at 1050°C for 1 hour inside the MOSS apparatus prior to κR experiments.

3.3 Dilatometry

To prepare dense LSF64 samples for bulk dilatometry, a rectangular bar of $2.5\ \text{mm} \times 2.5\ \text{mm} \times 7.65\ \text{mm}$ was cut from a hot pressed pellet (fabrication method detailed in *Section 3.2.2*) using a diamond saw. It was then loaded into a Netzsch DIL 402 C dilatometer along the longitudinal axis, followed by flushing with 50 sccm of air ($p\text{O}_2=0.21$), air- N_2 mixtures with $p\text{O}_2=0.021$ and 0.0005 , or research-grade pure N_2 ($p\text{O}_2 < 5 \times 10^{-6}$). New, $>95\%$ dense alumina spacers were placed adjacent to both ends of the sample to prevent dilatometer contamination. Linear dilatometry experiments were performed from room temperature to 1050°C at a heating rate of $1^\circ\text{C}/\text{min}$, during a 10 minute hold at 1050°C , and during cooling down to room temperature at a nominal rate of $1^\circ\text{C}/\text{min}$.

To prepare porous LSF64 samples for bulk dilatometry, calcined LSF64 powder was uniaxially cold pressed in a $1.27\ \text{mm}$ diameter stainless steel die. The resulting $9.25\ \text{mm}$ -long cylindrical pellet had an initial relative density of 30% , and was then loaded into the dilatometer, followed by 1050°C sintering for 1 hour, with heating and cooling rates both $5^\circ\text{C}/\text{min}$.

3.4 Structural, Morphological and Compositional Characterization

3.4.1 X-ray Diffraction

Phase purity and structural analysis was conducted on the LSF64 powder, bare YSZ wafer and the bilayer samples using an x-ray diffractometer (Bruker Davinci) operated at 30 kV and 15 mA with a copper filament and a Ni filter for $20^\circ < 2\theta < 80^\circ$ with a step size of 0.005° and a 0.1 sec/step dwell time.

3.4.2 Focused Ion Beam-Scanning Electron Microscopy (FIB-SEM)

Microstructural information was obtained using a scanning electron microscope (SEM, Zeiss Auriga) at 20 kV and 50 pA. For bilayer samples, prior to SEM analysis, ~ 1.5 nm of Pt was sputtered onto fracture surfaces to prevent electrical charging, and vertically mounted onto a SEM sample holder.

In order to characterize the microstructural parameters V_V and S_V of the porous films, a post- κ -tested bilayer sample was fractured, epoxy impregnated (EpoThin™, Buehler) and polished down to a 1 μm finish using SiC sandpaper and diamond lapping films (Allied High Tech). A Zeiss Auriga Focused Ion Beam-Scanning Electron Microscope (FIB-SEM) with an x-y spatial resolution of 1 nm was used to image a series of 2D microstructural cross-sections. The z spacing between adjacent x-y FIB-SEM slices was 25 nm. FIB polishing was conducted using a final milling probe current of 600 pA. SEM micrographs were taken using a 30 kV electron excitation voltage and a 4.2 mm working distance. The 2D serial SEM images were first aligned and cropped using the open source program IMOD [190], and then segmented into binary images using the Mimics® software program (Materialise). Mimics® was then used to 1) create a 3D reconstruction from the 2D images and to 2) extract the V_V and S_V values need to extract k using

Equation (34). For all the samples, the 25 nm z resolution was less than 1/15th of the particle size, ensuring 3D reconstruction V_V and S_V errors less than 5% [191].

3.4.3 X-ray Photoelectron Spectroscopy (XPS)

As a highly sensitive tool suitable for investigating solid-state surfaces, X-ray photoelectron spectroscopy (XPS) is a commonly used quantitative technique to probe the elemental composition at the surface by measuring the kinetic energy of escaped electrons from the top 2 to 5 atomic layers of the material optically excited by soft X-rays [192]. In this work, a Perkin Elmer Phi 5400 ESCA system with a magnesium $K\alpha$ X-ray source was used for XPS experiments. Samples were analyzed at pressures between 10^{-9} and 10^{-8} Torr with a pass energy of 29.35 eV and a take-off angle of 45° . The areal spot size was roughly $250 \mu\text{m}^2$. Atomic concentrations were determined using previously determined sensitivity factors. All peaks were referenced to the signature C1s peak for adventitious carbon at 284.6 eV.

4. Dilatometry Measurements on Bulk LSF64

4.1 Introduction

Before measuring the oxygen surface exchange and stress of mechano-chemically coupled films using the curvature relaxation technique, a better understanding of the chemical expansion of bulk material with the same composition is desirable. This chapter investigates the linear dilatometric behavior of $\text{La}_{0.6}\text{Sr}_{0.4}\text{FeO}_{3-\delta}$ (LSF64) between room temperature and 1000°C under various oxygen partial pressures. The results are fit to a thermo-chemical model, and used to extract both the thermal and chemical expansion coefficients.

4.2 Experimental

A $2.5\text{ mm} \times 2.5\text{ mm} \times 7.65\text{ mm}$ rectangular dilatometry sample was prepared by cutting a sample from a hot pressed, GNP-processed LSF64 puck, as detailed in *Sections 3.2.1* and *3.2.2*. The sample density prior to dilatometry was determined to be 95% using mass and dimension measurements.

Dilatometry measurements were performed following the procedures detailed in *Section 3.3*. Between individual measurements with different $p\text{O}_2$, a single dilatometry experiment was conducted in air under identical heating/cooling schedules. This was done to ensure the same starting level of initial LSF sample oxygen nonstoichiometry in each experiment.

4.3 Results and Discussion

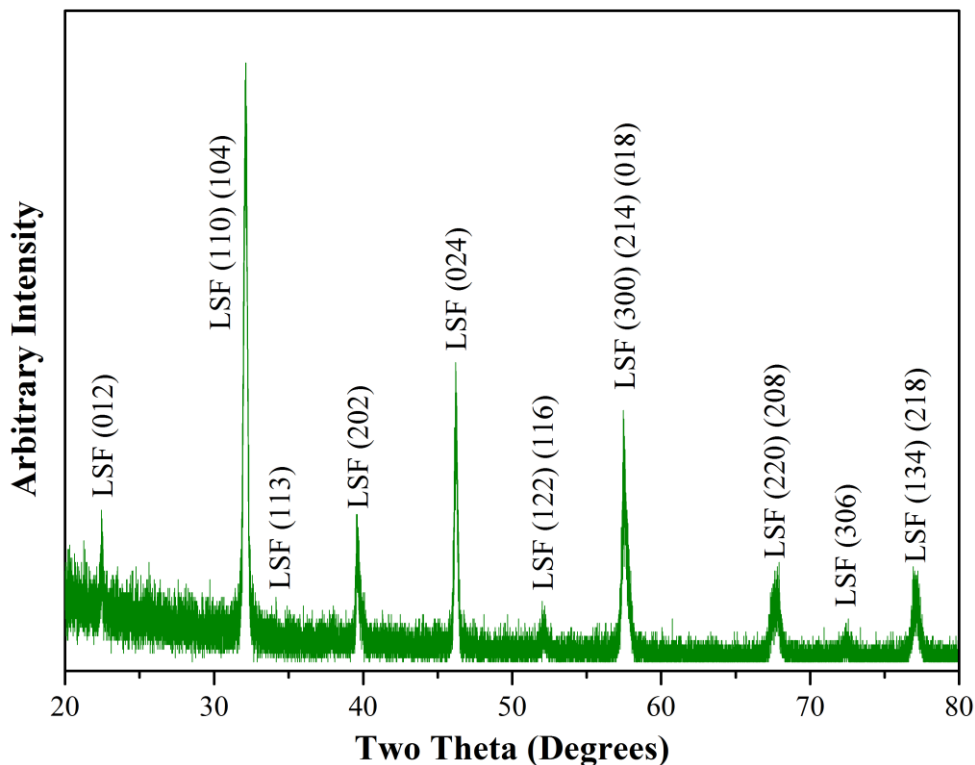


Figure 4.1 X-ray diffraction scans of calcined LSF64 powder. Peak indexing was performed using LSF64 PDF # 01-082-1961.

Figure 4.1 shows the X-ray diffraction spectrum of the LSF64 powder after calcination. All peaks indexed belong to PDF # 01-082-1961 for LSF64, indicating phase purity. The near cubic crystal structure of rhombohedral LSF64 [193] causes many of the rhombohedral XRD peaks to overlap.

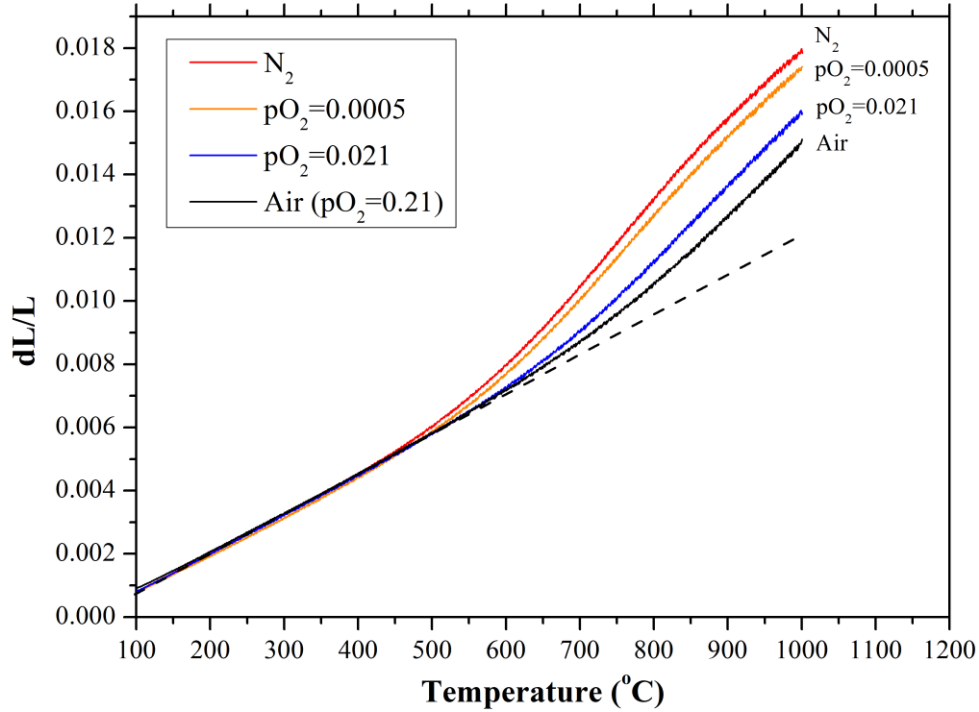


Figure 4.2 Bulk, dense LSF64 sample dilatometry under $pO_2=0.21$ (black), $pO_2=0.021$ (blue), $pO_2=0.0005$ (orange) and N_2 (red). The dashed line represents the fitted linear thermal expansion.

Figure 4.2 shows the one-dimensional dilatometry data of the bulk LSF64 sample under various oxygen partial pressures. It is clearly seen that for all the dilatometry curves, strain becomes non-linear at elevated temperatures, indicating the presence of chemical expansion as oxygen vacancies become prevalent. For the experiment under $pO_2=0.21$, the onset temperature of chemical expansion (where the deviation from pure thermal expansion occurs) is $\sim 525^\circ\text{C}$. The oxygen partial pressure in the testing atmosphere also impacts the chemical expansion (which is related to the distance from the extrapolation of the thermal expansion curve), which at first increases and then decreases as the pO_2 decreases. It also demonstrates that the thermal expansion coefficient of LSF64 is essentially independent of the pO_2 used in the film stress estimations in the following chapters.

Using the data in *Figure 4.2*, the thermal expansion coefficient (α_T) and the chemical expansion coefficient (α_C) of bulk LSF64 under $pO_2=0.21$ and $pO_2=0.021$ were fit using a thermo-chemical model proposed in the literature [82, 85] for mechano-chemically coupled materials:

$$\left(\frac{\partial \varepsilon_{T+C}}{\partial T} \right)_{pO_2} = \alpha_T + \alpha_C \left(\frac{\partial \delta}{\partial T} \right)_{pO_2} \quad (48)$$

where ε_{T+C} is the thermo-chemical expansion directly measured from dilatometry. Based on the linear regime of the dilatometry curves in *Figure 4.2* and a chemical expansion onset temperature of 525°C, α_T was determined to be 12.4 ppm/K by analyzing both expansion data sets from 100°C to 500°C. The temperature dependence of $\left(\frac{\partial \delta}{\partial T} \right)$ was estimated by analyzing the oxygen nonstoichiometry data from Mosleh *et al.* [50] and Equation (48). The first derivative of the thermo-chemical expansion data between 500°C and 1000°C was then fitted to Equation (48) and α_C was determined to be 0.0101 and 0.00867 for $pO_2=0.21$ and $pO_2=0.021$, respectively. These α_T and α_C are comparable to literature reports on similar LSF systems, such as $La_{0.6}Sr_{0.4}FeO_{3-\delta}$ at 500-900°C ($\alpha_T = 11.052$ ppm/K, $\alpha_C = 0.01994$) [194] and $La_{0.3}Sr_{0.7}FeO_{3-\delta}$ ($\alpha_T = 12.98$ ppm/K at 25-500°C, $\alpha_C = 0.017-0.047$ at 650-900°C) [195].

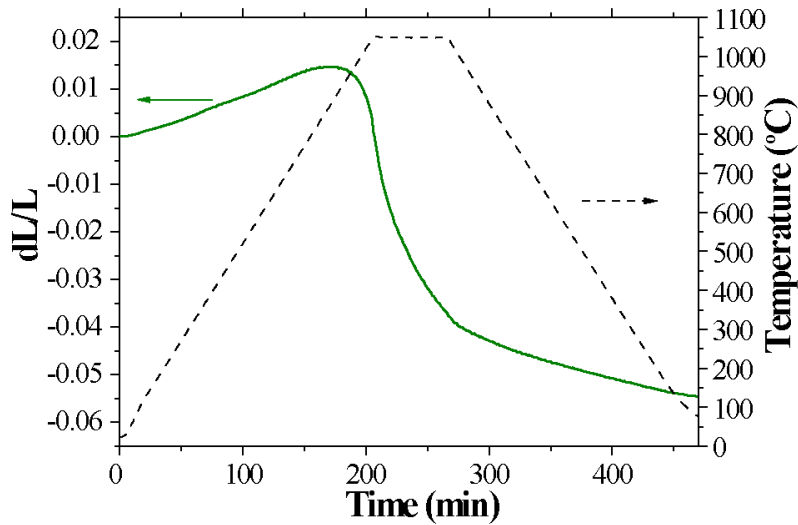


Figure 4.3 Bulk, porous LSF64 sample dilatometry in air ($pO_2=0.21$). The dashed line denotes the temperature schedule and the solid line denotes the measured linear strain.

Unlike the previous figure which analyzed the behavior of dense LSF64 samples, *Figure 4.3* shows the sintering behavior of a porous LSF64 bulk sample prepared in a manner described in *Section 3.3*. As indicated by the strain curve, the porous samples initially exhibited linear thermal expansion, and sintering did not start until around 850°C. This behavior is in agreement with the LSF sintering onset temperatures reported in the literature [196]. The fastest sintering rates were observed during the 1050°C hold, and linear thermal contraction occurred below 800°C during cooling. This suggests that porous films sintered at 1050°C and subsequently κR -tested at and below 700°C should remain microstructurally stable during κR measurements.

4.4 Conclusions

Thermo-chemical expansion of bulk LSF64 samples were measured using dilatometry under various oxygen partial pressures ranging from air to N_2 for the first time. The chemical expansion onset temperature decreases with decreasing pO_2 . The thermo-chemical analysis verifies that LSF64 is a mechano-chemical coupler, and determines the thermo-chemical

expansion coefficient for bulk LSF-64 ($\alpha_T=12.4$ ppm/K, α_C is 0.0101 and 0.00867 for $pO_2=0.21$ and $pO_2=0.021$, respectively). As it relates to the discussions in the following chapters, chemical expansion is not expected to occur in bulk LSF64 samples until 525°C in air. These results help inform the curvature relaxation experiments on LSF64 thin films under controlled temperature and oxygen partial pressure.

5. Oxygen Surface Exchange and Stress Measurements on Sputtered LSF64 Dense Thin Films

5.1 Introduction

In this chapter, the curvature relaxation technique was used to simultaneously measure reliable surface exchange and stress of sputtered $\text{La}_{0.6}\text{Sr}_{0.4}\text{FeO}_{3.8}$ (LSF64) thin films. LSF64 was chosen for these experiments because:

- (1) It has high oxygen ion ionic conductivity and oxygen exchange coefficient, which makes it important as a solid oxide fuel cell cathode material [197-199].
- (2) As a common oxygen exchange material, its chemical expansion coefficient ($\alpha_c = 0.01994$) [200] suggests large strains with small pO_2 changes, making it suitable for curvature relaxation measurements.
- (3) It has a single-phase rhombohedral crystal structure over the 25-800°C and $1 \times 10^{-12} \leq pO_2 \leq 1$ atm range [193, 200, 201], avoiding phase transformations due to temperature and oxygen partial pressure variations during the curvature relaxation experiments.
- (4) Its Young's modulus and Poisson's ratio are known as a function of temperature and pO_2 over the 25-900°C and $1 \times 10^{-4} \leq pO_2 \leq 1 \times 10^{-1}$ atm range [172], allowing literature-based thermo-chemical strain measurements to be converted in to film stress measurements.

5.2 Experimental

5.2.1 Sample Preparation

LSF64 powder synthesis and sputtering target fabrication techniques were detailed in *Sections 3.2.1* and *3.2.2*.

For the experiments in this chapter, 25.4 mm diameter, 200 μm thick, single crystal, 100-oriented $(\text{Y}_2\text{O}_3)_{0.08}(\text{ZrO}_2)_{0.92}$ (8YSZ) wafers were used as substrates for thin film LSF deposition. The smoothness of the polished deposition surface of the YSZ substrate (the root mean square polished side roughness was 1 nm according to manufacturer specifications) ensured desirable film uniformity and allowed high quality beam reflection during the κR experiments. Single crystal YSZ was chosen as a substrate material because:

- (1) It is chemically compatible with LSF. LSF-YSZ cation intermixing and/or interphase formation only occurs above 1000°C in air [202].
- (2) It has a high yield stress (>400 MPa below 800°C in air) [174], which ensured the elasticity of the substrate during the bilayer curvature experiments.
- (3) It has a fixed oxygen stoichiometry and a known elastic modulus in the 25-800°C and $1 \times 10^{-25} \leq pO_2 \leq 1$ atm range [175].

Prior to thin film deposition, the 8YSZ substrates were annealed at 1100°C for 1 hour to relieve residual stress within the substrates. To ensure adequate residual stress relaxation within the substrates during the annealed process, previously annealed bare 8YSZ wafers were tested from 25-800°C and showed no curvature changes with heating.

Experimental conditions for LSF64 thin film deposition are detailed in *Section 3.2.3*. For the experiments reported here, three simultaneously-prepared sputtered samples (SP-A, SP-B and

SP-C) with 250 nm thick LSF64 films were prepared by the Richard Lunt research group at Michigan State University.

5.2.2 Curvature Relaxation (κ R) Measurements

Prior to κ R experiments, LSF64|YSZ samples were annealed in the MOSS setup at 600°C for 1 hour to crystallize the as-deposited, amorphous LSF64. κ R experiments were then conducted at various temperatures by switching the atmosphere between pure air (Zero grade, Airgas, $pO_2=0.21$) and a gas mixture ($pO_2=0.021$) composed of pure air and pure nitrogen (99.9995% Research grade, Airgas) by abruptly turning a four-way valve. The duration of each relaxation experiment was more than five times the time constants fitted at a given temperature, ensuring the sufficient equilibration of the film to a new pO_2 (as explained in den Otter *et al.* [181]) and a good fit for transient kinetic analysis. The normalized LSF64|YSZ bilayer curvature vs. time was then plotted and least square fitted to Equation (33), using the Origin computer program, to extract surface exchange coefficients. Equilibrium stresses of all samples were measured using Stoney's equation (31) and averaging the equilibrium curvature values at each temperature, pO_2 and thermal segment, and plugging into. Of the 3 samples from the same batch, SP-A was κ R-tested for only one thermal segment, while SP-B and SP-C were κ R-tested for a total of 7 thermal segments.

5.2.3 Structural and Compositional Characterization

After *in-situ* testing, microstructural information was obtained on the fracture surface of each bilayer sample using a scanning electron microscope. Crystal structure characterization was also conducted on the top surface of the bilayer samples before and after MOSS tests, using an X-ray diffractometer. The experimental conditions used for both techniques are detailed in *Section 3.4*.

5.3 Results and Discussion

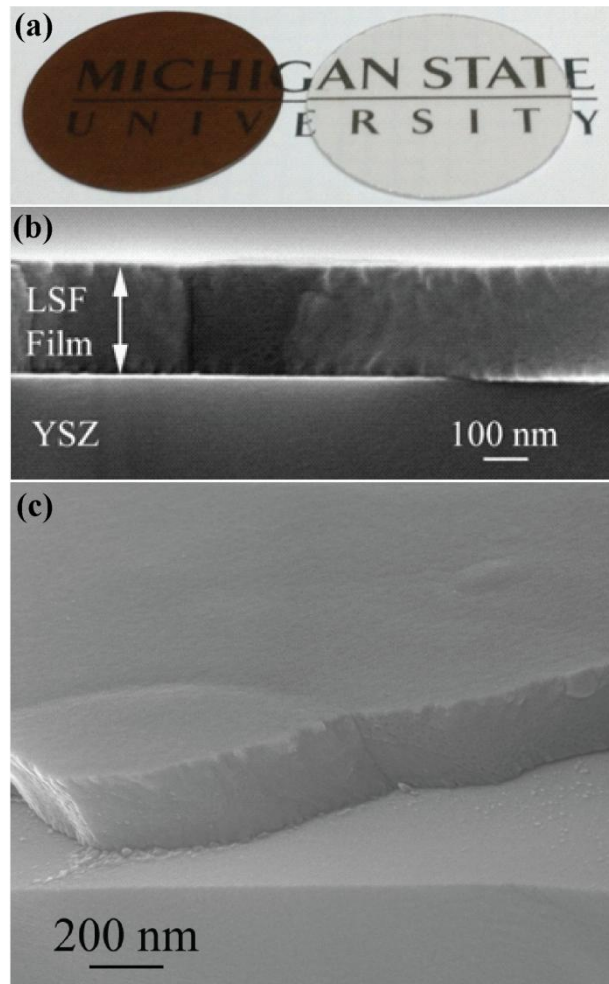


Figure 5.1 (a) Macroscale morphology of YSZ substrates with (left) and without (right) a LSF64 film. (b) cross section and (c) 45° view of the fracture surface morphology of the LSF64/YSZ bilayer after κR testing.

As shown in *Figure 5.1* (a), the LSF64 films studied here had a brown color and were translucent, while the bare 25.4 mm diameter YSZ substrates were colorless and transparent. *Figure 5.1* (b) and (c) show the microstructure of the LSF64|YSZ cross section, indicating a uniform, crack-free film thickness of 250 ± 3 nm.

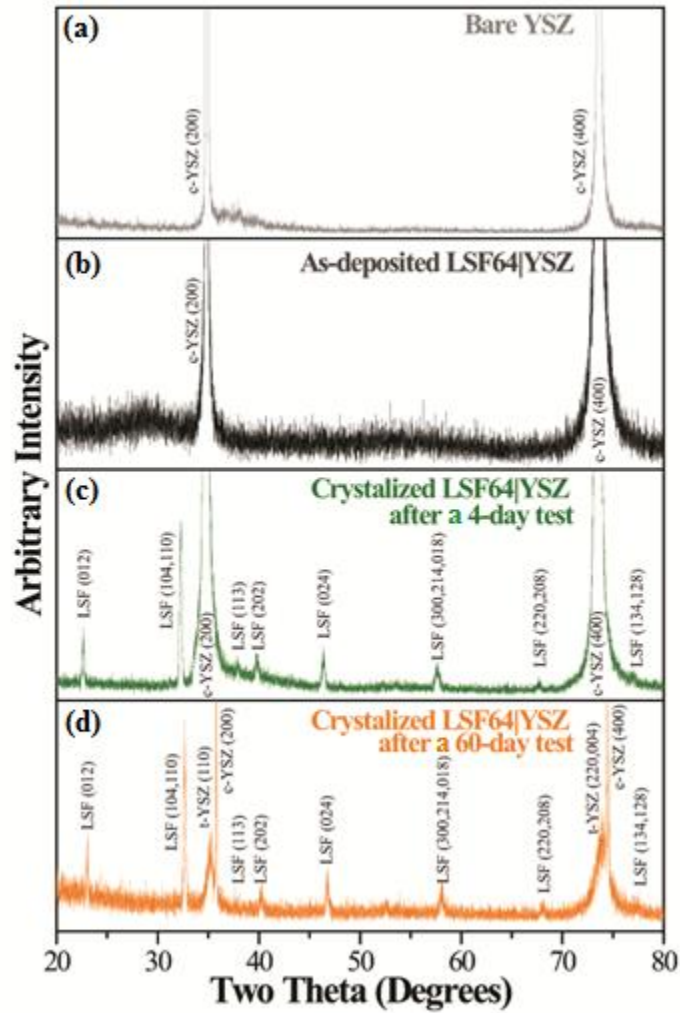


Figure 5.2 X-ray diffraction scans of YSZ substrates (a) without any coating, (b) with as-sputtered with LSF64 film, (c) with a 4-day MOSS tested LSF64 film [203] and (d) with a 60-day MOSS tested LSF64 film (this study). Peak indexing was obtained from PDF # 01-082-1961 for LSF64, 01-070-4436 for cubic YSZ (c-YSZ) and 01-070-4431 for tetragonal YSZ (t-YSZ).

As shown in *Figure 5.2*, the sputtered LSF64 films were initially amorphous, and became phase pure after crystallization at 600°C. All the indexed peak intensities were consistent with

the major peaks in LSF64 Powder Diffraction File (PDF) # 01-082-1961, indicating that the films were polycrystalline and without preferred orientation. While the x-ray diffraction profiles of the YSZ substrates before and after a short-term κ R test were consistent with the (100)-oriented single crystal specification, the long-term tested sample showed a cubic-to-tetragonal phase transformation (known to occur for 8 mol% YSZ [204]) after long times at elevated temperature, indicated by YSZ peak splitting in *Figure 5.2(d)*. No other peaks other than those belonging to LSF and YSZ were observed, indicating that the film and the YSZ substrate had good chemical compatibility. Additional tests on 13 mol% YSZ substrates (not shown) gave identical k results as those reported here, but did not show a cubic-to-tetragonal phase transformation.

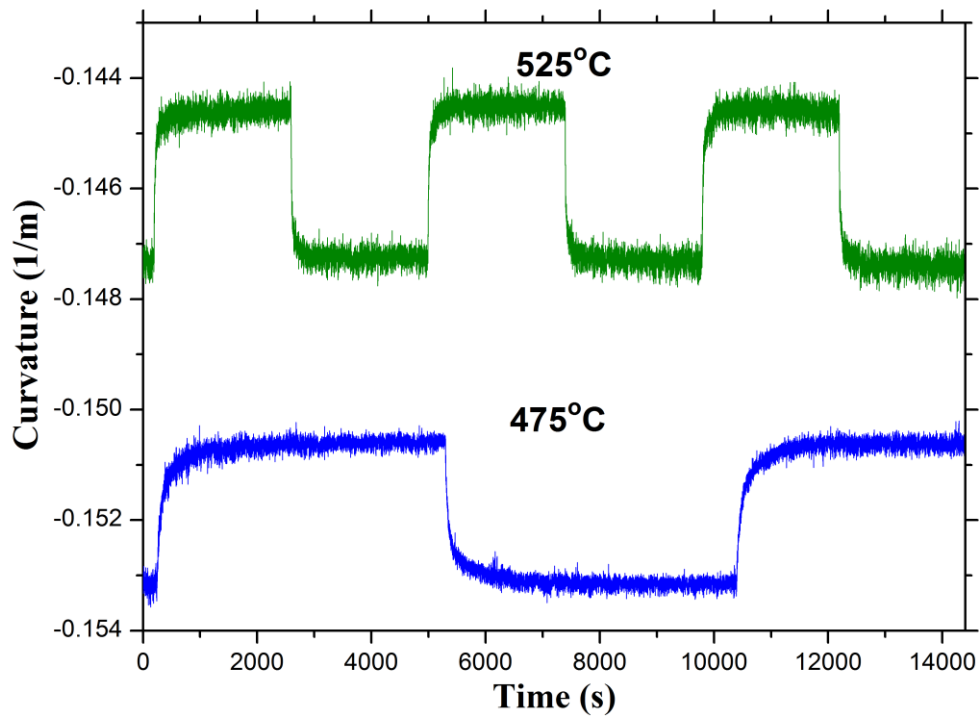


Figure 5.3 Representative multiple curvature relaxation cycles between $pO_2=0.21$ (air) and $pO_2=0.021$ (N_2 -air) at $525^\circ C$ and $475^\circ C$. The difference in equilibrium curvature levels between the two temperatures stems from the film-substrate thermal expansion mismatch [193, 205].

Figure 5.3 shows multiple κR cycles upon switching between $pO_2=0.21$ and $pO_2=0.021$. Reproducible relaxation kinetics and equilibrium curvature levels were observed for multiple isothermal relaxations. This indicates that the LSF64 oxygen nonstoichiometry changes were reversible as the atmosphere pO_2 changed, and that no significant film cracking or delamination occurred. The different equilibrium curvatures at different temperature were as expected from the thermal expansion mismatch between the LSF64 (~ 14 ppm/K [193]) and the YSZ (9.4-9.5ppm/K [205]). Also shown is the clear temperature dependence of the relaxation time.

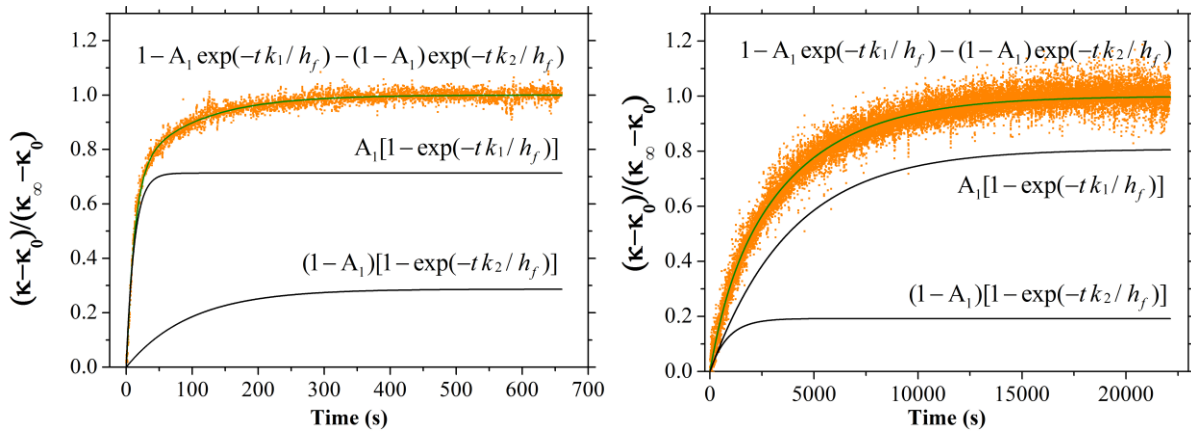


Figure 5.4 Normalized curvature relaxation data (dots) of the LSF64 film SP-C on reduction at 525°C (left) and on oxidation at 375°C (right). The top line is the combined fit to the data, while the lower lines show the separate contributions of each relaxation rate.

Figure 5.4 shows representative normalized curvature spectra at 525°C on reduction and 375°C on oxidation. Surprisingly, at all tested temperatures, (i.e. between 350°C and 600°C, the κR spectra were well fit to two surface exchange coefficients (k_1 and k_2) using Equation (33), indicating the presence of two distinct oxygen incorporation pathways.

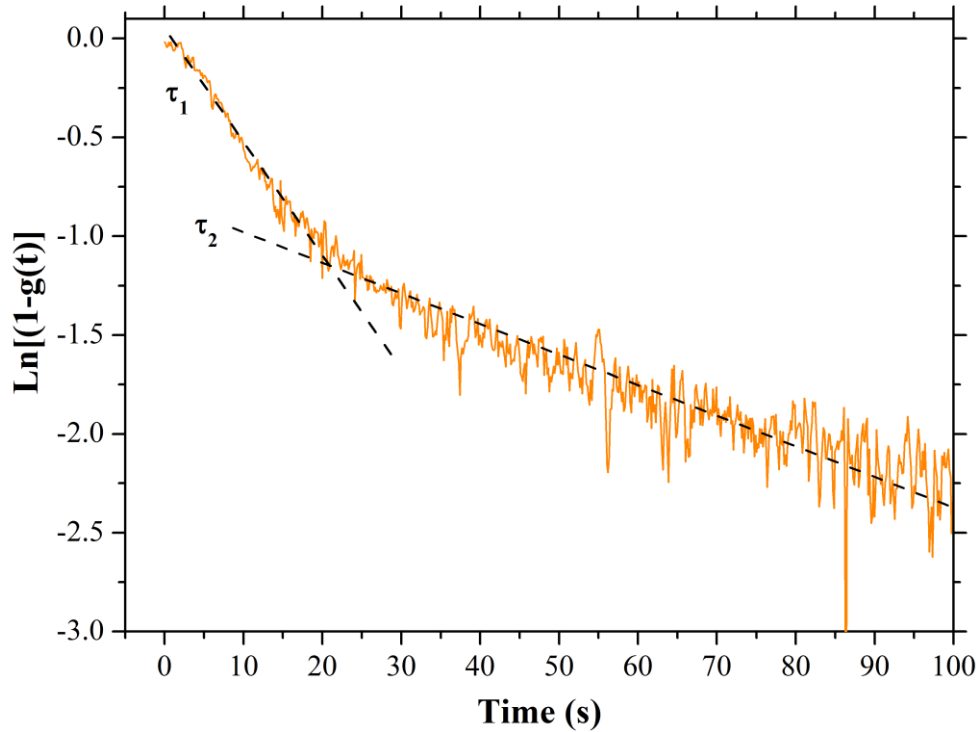


Figure 5.5 The κR data of 525°C on reduction plotted on a semi-log plot to illustrate that two relaxation times, τ_1 and τ_2 , are present.

Figure 5.5 demonstrates the two distinct time constants in a semi-logarithm plot of the κR data at 525°C on reduction. Similar two-fold relaxation behavior of electrical conductivity has been reported on MIEC single crystals [131] and epitaxial MIEC thin films [132, 206]. In these literature reports, this dual-time-constant behavior was attributed to either (a) surface regions with different crystallographic orientations [131], or (b) surfaces with different contributions from the bulk and grain boundaries [207].

For the reasons that will be discussed later in *Chapter 7*, the two distinct surface exchange coefficients, k_1 and k_2 , were attributed to bulk grains and grain boundaries, respectively, as shown in *Figure 5.6*.

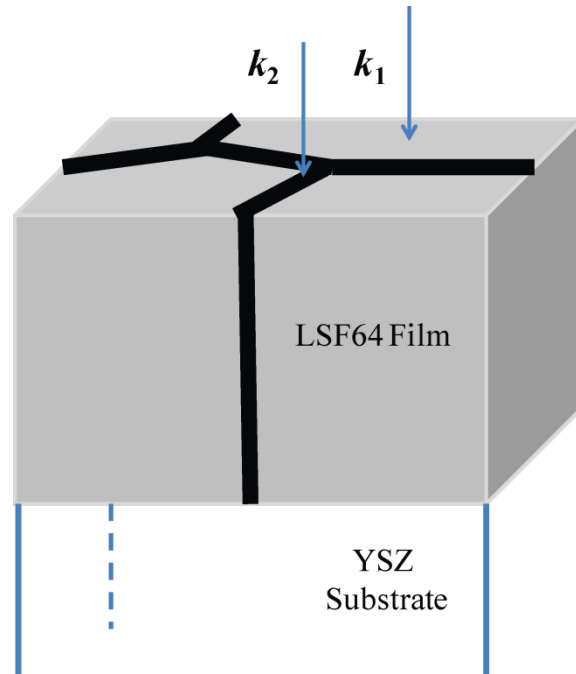


Figure 5.6 Schematic of the surface exchange process in the sputtered thin film. k_1 and k_2 , can be attributed to bulk grains and grain boundaries, respectively.

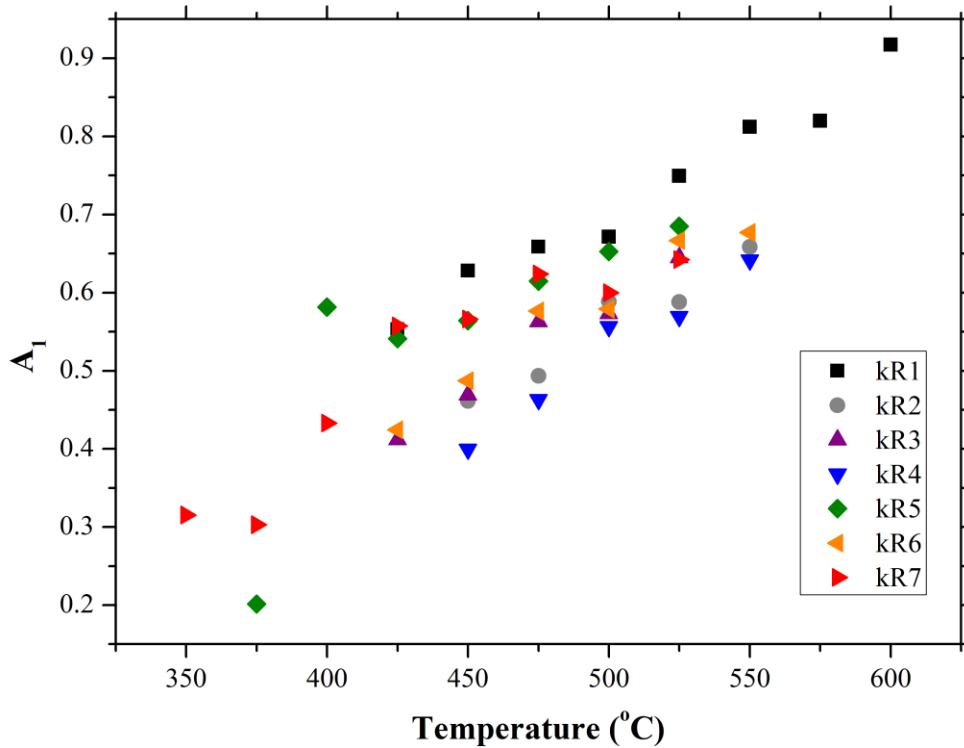


Figure 5.7 A_1 values of the sputtered LSF64 thin film SP-C as a function of temperature across all seven thermal segments. Each value is averaged from its corresponding oxidation and reduction relaxation processes.

Figure 5.7 shows the A_1 values of sample *SP-C* fitted to Equation (33), indicating that the ratio between the two exchange rates changes with temperature. The faster surface exchange process (assigned to the exposed bulk grain surface) dominates at higher temperature, while the slower surface exchange process (assigned to the exposed grain boundaries) makes greater contribution as the temperature is reduced.

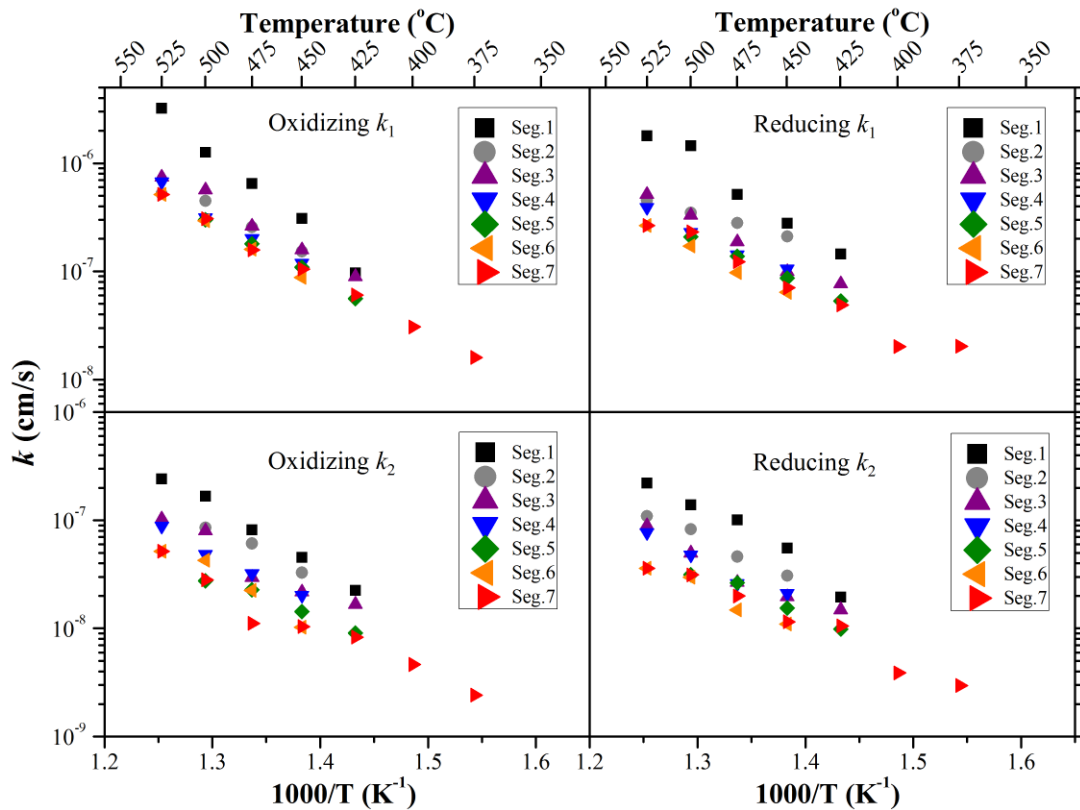


Figure 5.8 Arrhenius plots of both k_1 and k_2 in LSF64 thin film sample *SP-B* under oxidation and reduction conditions. Segment numbers follow the chronological order of the experiment. Segments 1, 3, 5 and 7 were measurements as the sample was cooling down, while segments 2, 4 and 6 were measurements as the sample was heating up.

Figure 5.8 shows the Arrhenius behavior of the κR -measured k 's under multiple thermal cycles. The sequentially numbered thermal segments represent the first time the electrochemical properties of LSF have been analyzed as a function of thermal cycling. Given the 1.2% error of

the film thickness estimated from the standard deviation of SEM measurements at 5 different locations and the <6.4% error of the fitting procedure of the normalized curvature data according to Origin ©, the estimated error bars of all data points based on the error analysis method in *Section 3.1.6* are smaller than the size of the symbols.

As shown in *Figure 5.8*, degradations of up to a factor of 8 in the oxygen surface coefficient were observed with multiple thermal segments. The activation energies of both k_1 and k_2 measured in this study, $\sim 1.1 \pm 0.3$ eV, were reproducible across multiple thermal segments, and are close to the 1.3 eV of bulk LSF64 sample measured by ten Elshof et al. [47]. Although there is considerable spread in some of the data, it seems that after an initial break-in period during the first thermal segment (a common occurrence for MIEC materials [198]), subsequent thermal cycling between 425 and 525°C only produced minor changes in k .

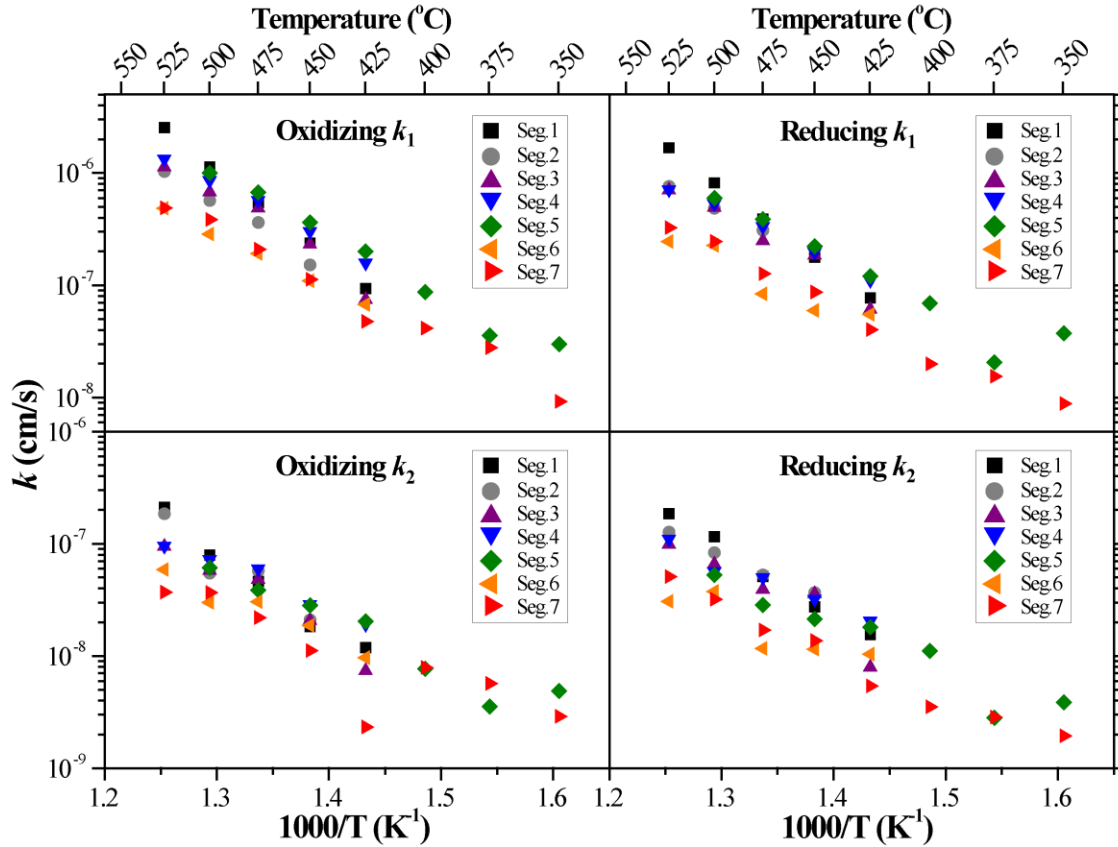


Figure 5.9 Arrhenius plot of both k_1 and k_2 of LSF64 thin film sample SP-C under oxidation and reduction conditions.

Similar measurements were conducted on sample SP-C and similar magnitude oxygen surface exchange coefficients were observed, as shown in *Figure 5.9*. Further, like sample SP-B, k did not degrade with multiple thermal cycling when cycled between 525 and 425°C, but did experience k degradation when cycled below 425°C and heated back up to elevated temperature. This indicates some irreversible changes occurred in the film are possibly associated with inelastic deformation at higher stress states. This idea is discussed in detail in the stress measurements of *Figure 5.13*. The similar behavior between both samples indicates the reproducibility of measurements on samples prepared simultaneously.

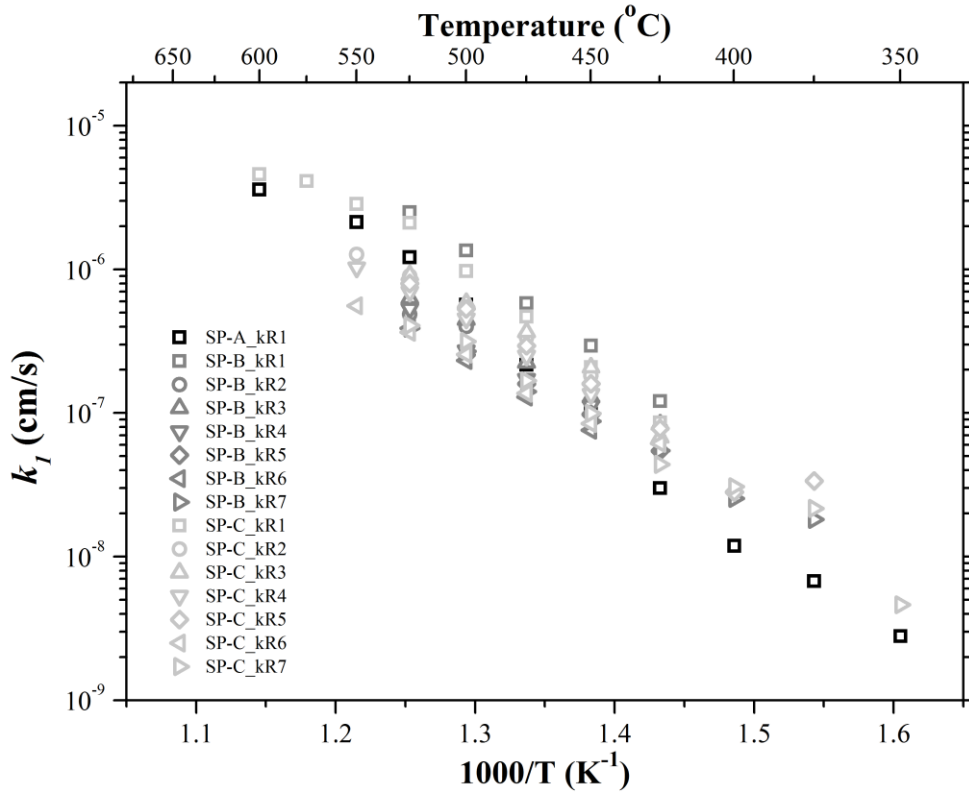


Figure 5.10 κR -determined k_1 values of sputtered LSF64 thin film samples SP-A, SP-B and SP-C as a function of inverse temperature across multiple thermal cycles. k values are averaged from oxidation and reduction k 's.

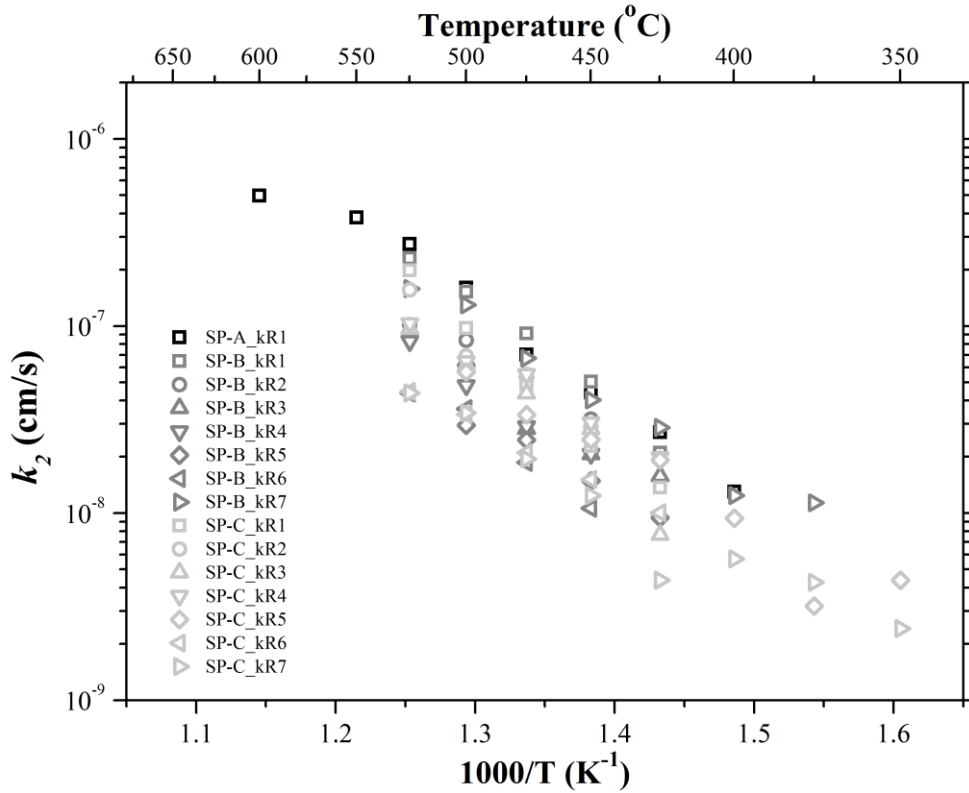


Figure 5.11 κR -determined k_2 values of sputtered LSF64 thin film samples SP-A, SP-B and SP-C as a function of inverse temperature across multiple thermal cycles. k values are averaged from oxidation and reduction k 's.

Figure 5.10 and Figure 5.11 summarize the surface exchange coefficient measurements of three sputtered samples from the same batch. Compared to the 5 orders of magnitude k variation observed for LSF64 in the literature, the k 's obtained here agree well with each other.

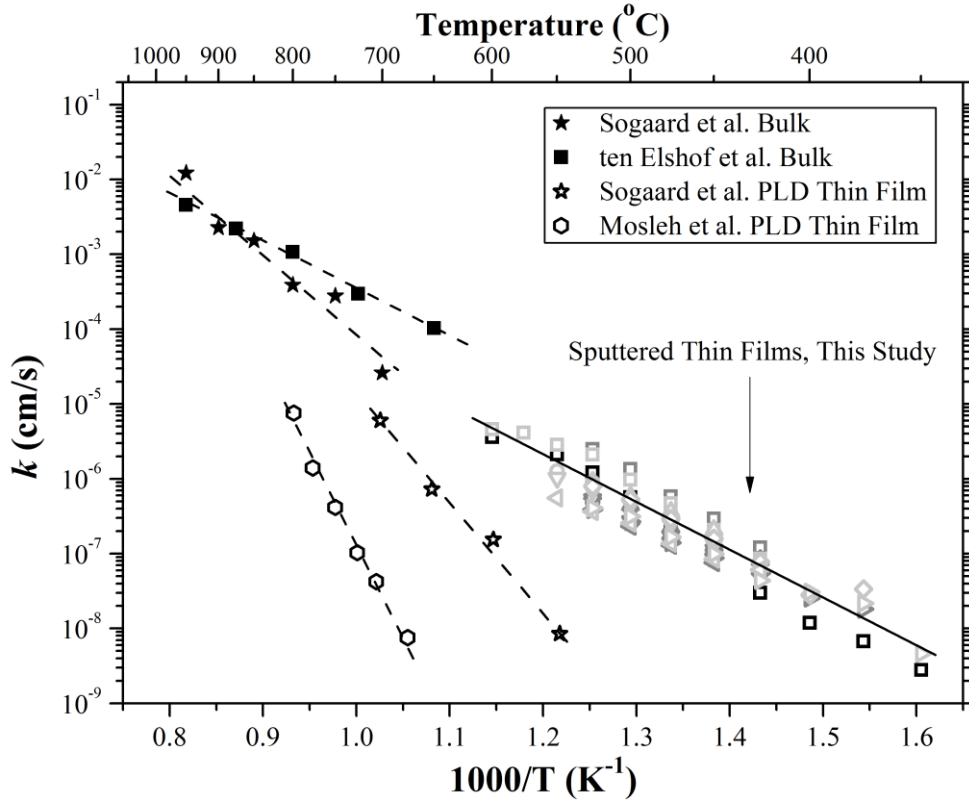


Figure 5.12 LSF64 κR -determined k_1 values compared with those in the literature [47-50]. Open symbols denote literature values.

Figure 5.12 shows how the k_1 values (lattice surface exchange coefficients) of sputtered LSF64 thin films obtained here via κR compared to those available in the literature. The activation energy of the sputtered thin films ranges from 1.2 eV to 1.4 eV. These values are close to the 1.3 eV activation energy observed for bulk LSF64 by ten Elshof et al. [47]. These ~1.3 eV activation energies, which were very different than the apparent 0.07 eV expected for an atmospheric flushing process [181], indicate that reactor volume flushing limitations were not present in these κR experiments. The sputtered films tested here exhibited k_1 values that were consistent with low-temperature extrapolations of bulk LSF64 k values [47, 49], and inconsistent with literature pulsed laser deposited LSF64 films [48, 208]. The close k agreement between the sputtered films and bulk samples may be because the non-epitaxial, polycrystalline sputtered

films tested here without electrodes more closely resembled the structure of the bulk LSF64 samples [49, 208] than the epitaxial PLD thin films [48, 208] previously measured via ECR in the literature. For example, these literature films may have had a different surface structure or stress state because of the electrodes used to measure them, their epitaxial nature, and/or a different stress/strain history.

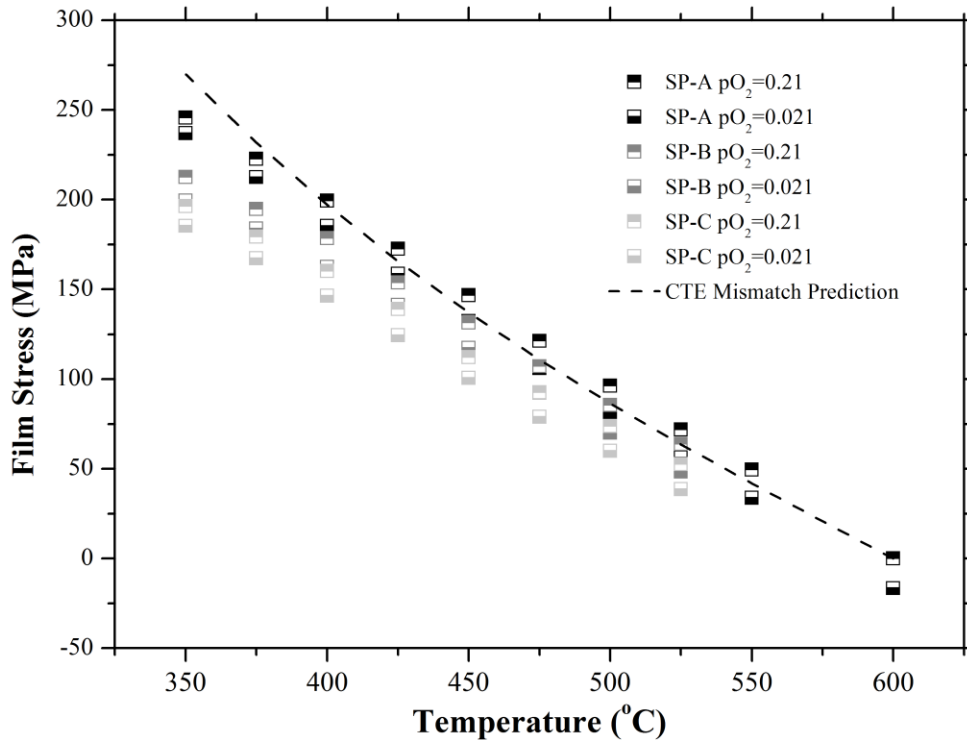


Figure 5.13 Average equilibrium stress levels of the LSF64 film as a function of pO_2 and temperature. The dashed lines represent thermal expansion mismatch induced stress, based on coefficient of thermal expansion (CTE) and elastic constants of YSZ and LSF64 available in the literature [193, 205].

Figure 5.13 shows the equilibrium stress of samples SP-A, SP-B and SP-C as a function of temperature compared to the stress expected from the coefficient of thermal expansion (CTE) mismatch between LSF64 [193] and YSZ [194]. The observed chemical stress induced by pO_2 changes is in agreement with the chemical expansion effect, where reducing pO_2 causes expansion of the LSF film, thus inducing less tensile stress in the film. Given the $\sim 1.2\%$ error of

the film thickness and the ~1% error of the substrate thickness estimated from the standard deviation of SEM measurements at 5 different locations, and the <0.1% standard error of the equilibrium curvature measurement across the temperature range, the estimated error bars of all data points based on the error analysis method in *Section 3.1.6* are smaller than the size of the symbols.

General agreement is observed compared to the CTE mismatch predictions, except for deviations below 425°C. This indicates that the bilayer started to deform inelastically, as the thin film stress became larger than ~200 MPa. This behavior is consistent with the 100 MPa yield stress measured in bulk LSF64 [209]. This may have been caused by (a) Sr segregation to the surface of LSF64, (b) ferroelastic domain switching occurring at higher level of stress (which has been observed in LSF64 [210, 211]), (c) dislocation formation as a stress relaxation mechanism, or a combination of multiple effects. This may also explain why reproducible k 's were observed in samples that were cycled between 600°C and 425°C, but were not obtained in samples cooled down below 425°C and then retested at elevated temperatures.

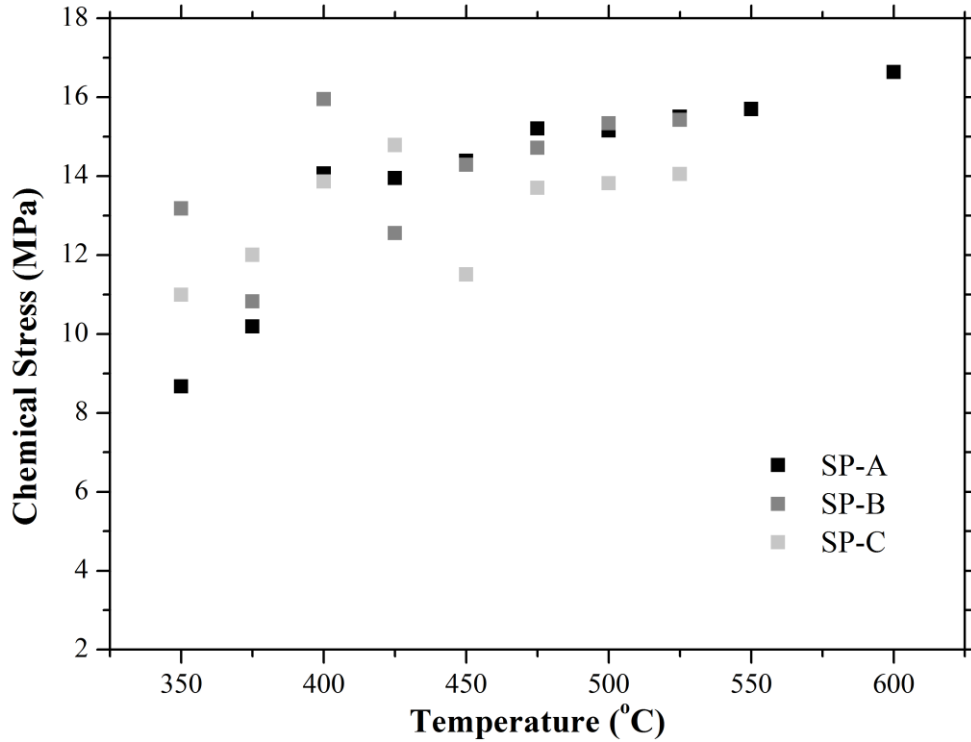


Figure 5.14 Chemical stress of sputtered LSF64 films induced by pO_2 changes between 0.21 and 0.021 as a function of temperature.

Figure 5.14 shows the chemical stress induced by switching between $pO_2=0.21$ and $pO_2=0.021$ across the temperature measurement range, which decreases with decreasing temperature. Similar to the film stress measurement, the chemical stresses of samples SP-A, SP-B and SP-C are generally consistent with each other. In contrast to dilatometry measurements in Chapter 4 and literature thermo-chemical studies [49, 193] on bulk samples indicating that mechano-chemical coupling in LSF64 only occurs above 525°C , non-zero chemical stresses were observed as low as 350°C in the sputtered films measured here. As will be discussed further in Chapter 7, this is likely due to grain boundaries and grain interiors displaying different chemical expansion behavior.

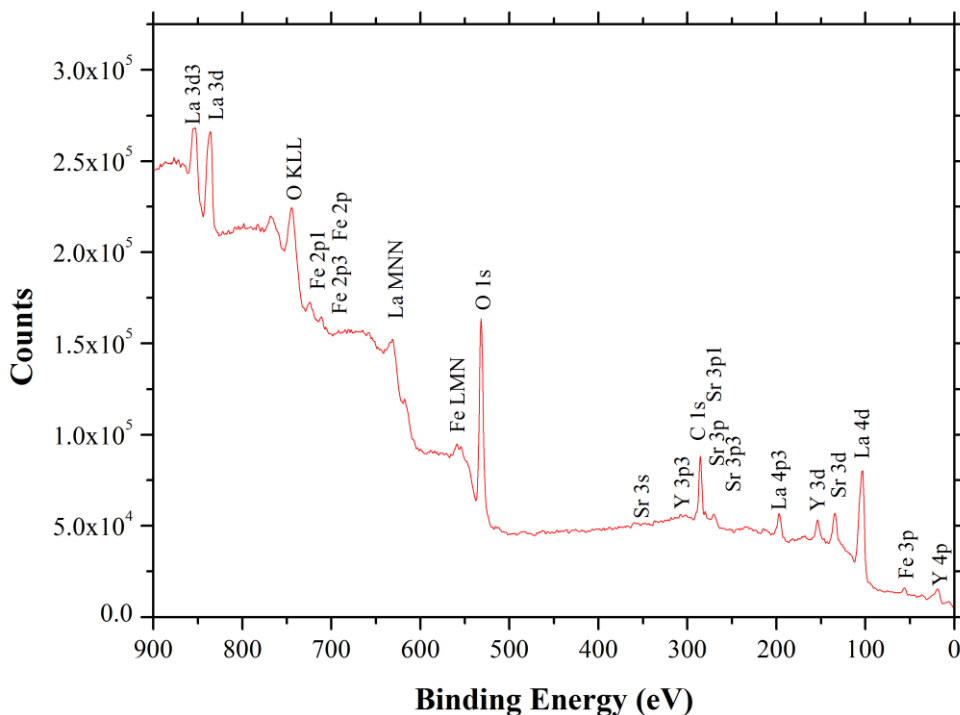


Figure 5.15 X-ray photoelectron spectroscopy (XPS) measurements on the sputtered LSF64 thin film SP-A after κ R testing.

Table 4 Atomic fractions of cation species at the surface of sputtered thin film SP-A

		La	Sr	Fe	Y	La:Sr:Fe ratio
Atomic Fraction (%)	Nominal	--	--	--	--	0.6 : 0.4 : 1
	LSF64 8YSZ (SP-A) after κ R test	2.66	3.30	2.24	0.11	1.19 : 1.47 : 1

Figure 5.15 and Table 4 show the XPS measurements on the sputtered thin film SP-A, which was κ R-tested for only 1 thermal segment. La and Sr surface enrichment were observed after the κ R-test. A small amount of Y impurities were also detected. Although XPS measurements on SP-B and SP-C were not performed, cation segregation of sputtered LSF64 thin films may be one of the reasons for the degradation in surface exchange kinetics with multiple thermal cycling, as discussed in Section 2.3.6. Future XPS measurements on samples analyzed before and after κ R are needed.

5.4 Conclusions

Here, for the first time, *in situ* stress and oxygen surface exchange coefficients were simultaneously measured on an MIEC thin film using the curvature relaxation technique. In addition, mechano-chemical coupling of LSF64 was observed below 525°C for the first time. Sub-525°C k values were reported for this material for the first time, and were consistent with low temperature extrapolations of bulk LSF64 sample behavior reported in the literature. A slight degradation in the measured surface exchange coefficients was observed over multiple thermal cycles for all samples from different batches, and was attributed to inelastic deformation in the film possibly caused by Sr segregation, ferroelastic domain switching, and/or dislocation formation. This significant amount of chemical stress observed at low temperatures in the sputtered films was in contrast to chemical expansion behavior of bulk LSF64, and was attributed to the small grain size of the sputtered LSF64. This small grain size also allowed the k 's for oxygen exchange directly into the lattice and the grain boundaries to be observed. As demonstrated here, the κ R technique provides insights towards understanding the surface exchange mechanisms and their relation to internal and external stress, as well as opportunities to characterize a range of mechano-chemically coupled ion-exchange materials.

6. Oxygen Surface Exchange and Stress Measurements on Pulsed Laser Deposited LSF64 Dense Thin Films

6.1 Introduction

In this Chapter, the κ R technique was used to simultaneously measure the *in situ* stress and k of pulsed laser deposited (PLD) thin films LSF64 on 13mol% YSZ substrates. The results demonstrate the applicability of the κ R method on thin films produced via various deposition techniques, and provide a deeper insight into how different processing histories and/or stress states that alter oxygen surface exchange kinetics.

6.2 Experimental

6.2.1 Sample Fabrication

Two types of PLD LSF64 thin films were prepared by Dr. William Chueh and his research group at Stanford University. The first type was deposited directly on (100) oriented 13mol% YSZ (LSF64|YSZ), and the second type was deposited on a (100) oriented 13mol% YSZ substrate coated with a 5-nm layer of scandium doped ceria (LSF64|SDC|YSZ) to prevent cation diffusion from the YSZ substrate to the surface of the LSF film. All YSZ substrates were pre-annealed at 1100°C for 1 hour. The annealing procedures of the YSZ substrates were identical to those listed in *Chapter 6*, the PLD film deposition temperature was 700°C and the oxygen partial pressure was set at 5 mTorr. The estimated deposition rate was 0.002 nm/pulse. Even though the stress evolution behavior of the annealed bare 13 mol% YSZ wafers were not tested, because a 1-hour hold at 1100°C was enough to remove the residual stress in the 8 mol%

YSZ wafers of *Chapter 5*, the same annealing schedule was assumed to have a similar effect on the 13 mol% YSZ wafers.

6.2.2 Curvature Relaxation Measurements

Details about the experimental setup of the curvature relaxation (κ R) technique can be found in *Section 3.1*. Prior to κ R experiments, the LSF64|YSZ samples were heated to 800°C at a rate of 5°C/min, and the first thermal segment was conducted during cool-down. The bilayer samples were subjected to abrupt switching between air (Airgas, $pO_2=0.21$) and 2.1% O_2 -97.9% N_2 mixture (Airgas, $pO_2=0.021$) controlled by a four-way valve. Relaxation experiments under both 100 and 500 sccm flow rate were also conducted to determine if there were reactor flush time limitations. The normalized curvature data processing was done in the same manner as the sputtered films.

6.2.3 Structural and Compositional Characterization

SEM, XRD and XPS experiments adopted the same conditions as those for the sputtered films, as shown in *Section 5.2.3*.

6.3 Results and Discussion

6.3.1 LSF64|YSZ

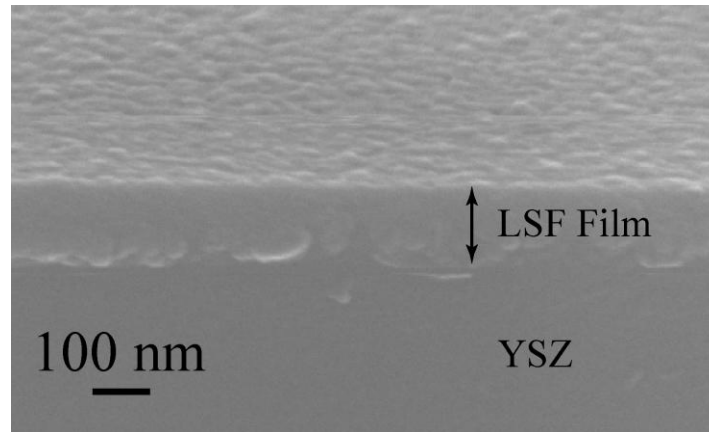


Figure 6.1 Fracture surface morphology of the PLD LSF64|YSZ bilayer after κR testing.

Figure 6.1 shows the microstructure of a LSF64|YSZ cross section, indicating a uniform film thickness of 135 ± 3 nm, and a columnar grain structure.

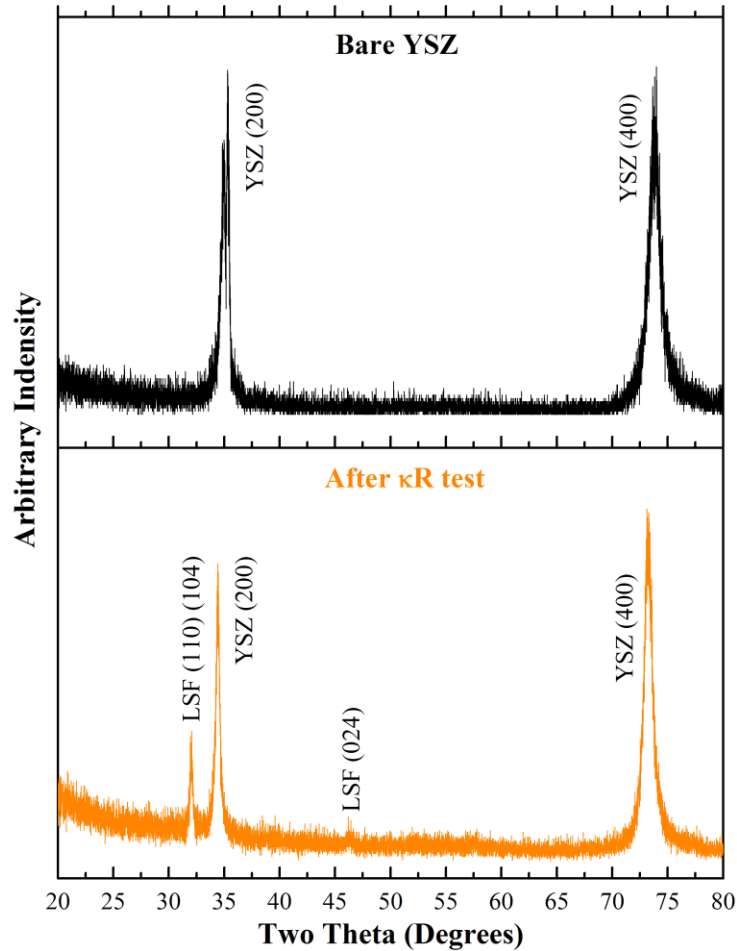


Figure 6.2 X-ray diffraction scans of the PLD LSF64/YSZ before and after κ R testing. Peak indexing was performed using LSF64 PDF # 01-082-1961 for LSF64 and cubic YSZ PDF# 01-070-4436.

As shown in *Figure 6.2*, the PLD thin film LSF64 exhibits epitaxial features with (110) (104) as the main orientation. From the indexed d-spacings of LSF64 (110) (2.7636 \AA) and YSZ (200) (2.5689 \AA), a $\sim 7.5\%$ mismatch between the film and the substrate was estimated. Small peaks corresponding to (024) of LSF64 were also observed, indicating formation of limited polycrystals. No impurity phase peaks were observed. The grain size was estimated to be $\sim 52 \text{ nm}$ using the William-Hall method [212].

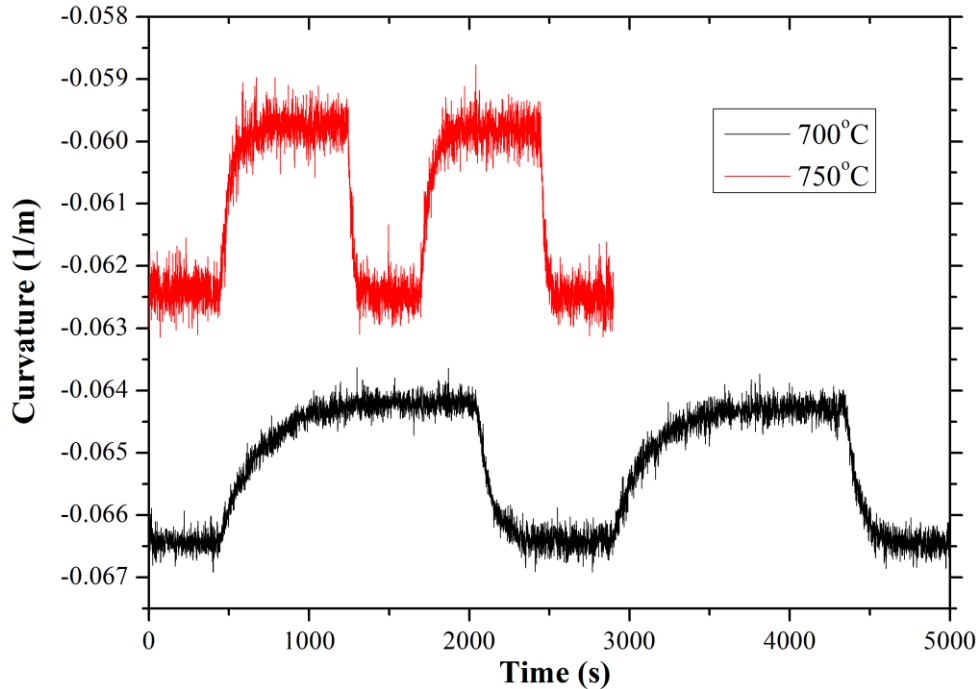


Figure 6.3 Multiple curvature relaxation cycles of the LSF64/YSZ sample at 700°C and 750°C between $pO_2=0.21$ and $pO_2=0.021$. The difference in equilibrium curvature levels between the two temperatures is a result of the film-substrate thermal expansion mismatch.

Figure 6.3 shows multiple κR cycles upon switching between $pO_2=0.21$ and $pO_2=0.021$ at 700°C and 750°C. Reproducible relaxation kinetics and equilibrium curvature levels were observed for multiple isothermal relaxations. This indicates that oxygen nonstoichiometry changes in the PLD LSF64/YSZ thin film were reversible as the atmosphere pO_2 was changed, and that no significant film cracking or delamination occurred. Similar to the sputtered thin films, the different equilibrium curvatures at different temperature were as expected from the thermal expansion mismatch between the LSF64 and the YSZ. In contrast to the sputtered films described in Chapter 5, only one relaxation time constant was observed at all temperatures, as demonstrated in Figure 6.4, indicating that only one surface exchange process dominated during the κR experiments. Given the larger grain size of the PLD films (52 nm) compared to those of the sputtered films (43 nm), this k was assigned to oxygen incorporation directly into the grain

interior lattice (i.e. not into the grain boundaries). Identical $\text{Ln}[1-g(t)]$ analysis at all other tested temperatures yielded similar results.

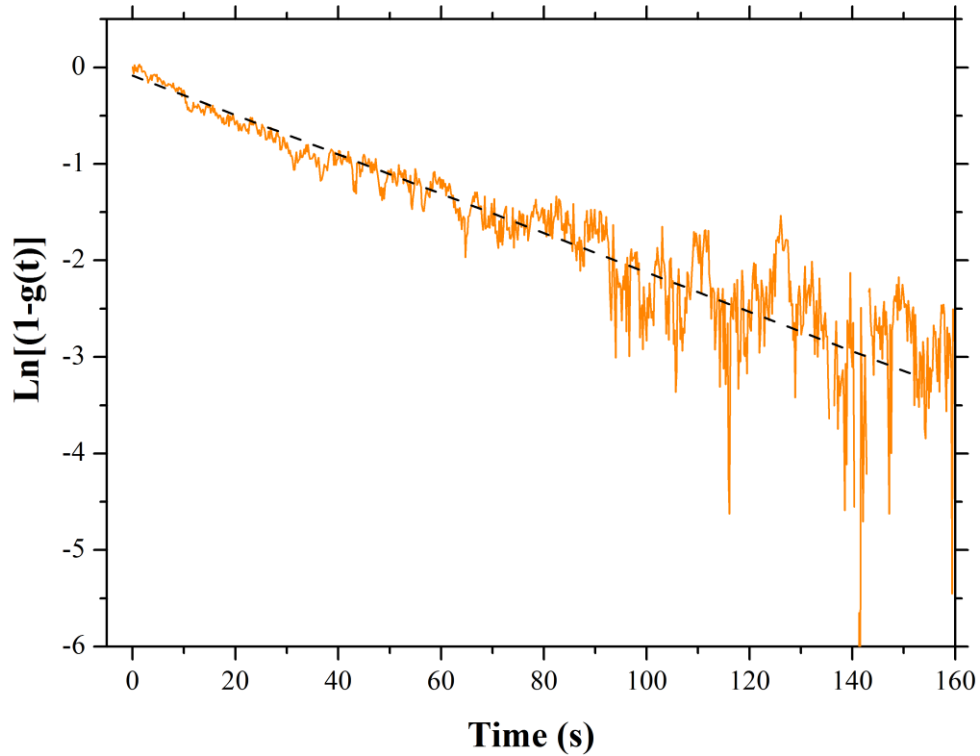


Figure 6.4 Representative κR data of 700°C on reduction shown in Figure 6.3 replotted on a semi-log plot, and showing only one time constant. κR data of other temperatures showed similar single time constant behavior.

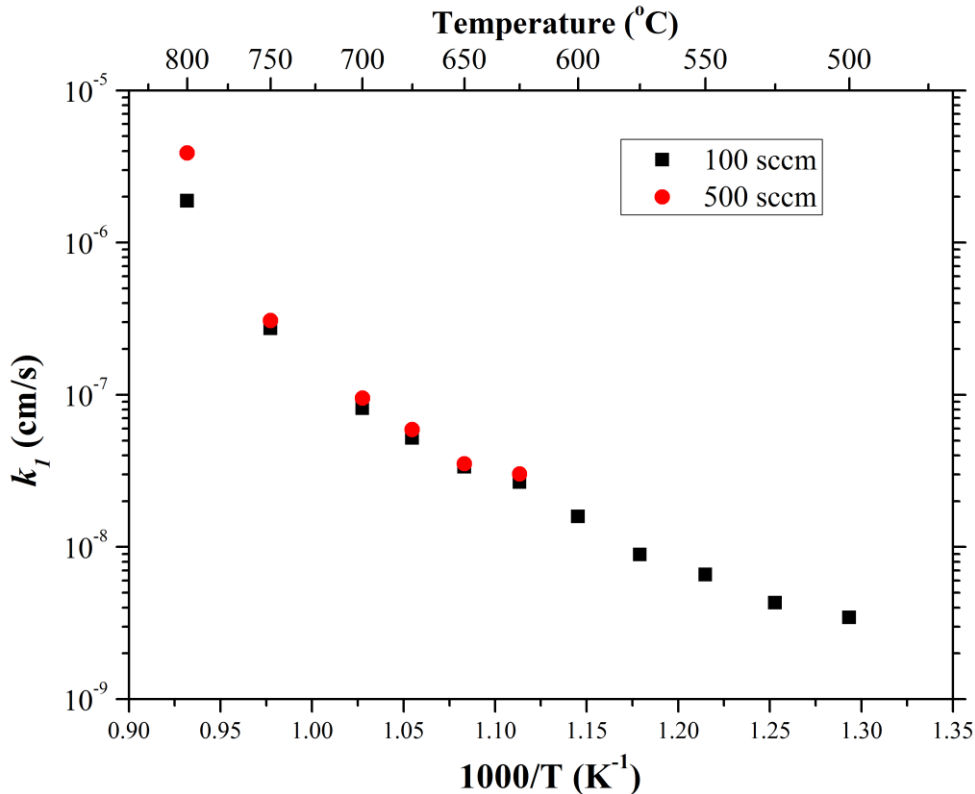


Figure 6.5 κ R-measured surface exchange coefficients of LSF64/YSZ as a function of temperature and flow rate.

As shown in *Figure 6.5*, the κ R-determined surface exchange coefficients were relatively insensitive to the flow rate, indicating that reactor flush time was not an issue at temperatures as high as 750°C. This is also demonstrated by the measured time constants (10 to 5500 s between 500°C and 800°C at 100 sccm, and 5 to 800 s between 625°C and 800°C at 500 sccm), which are 5 times smaller than their respective reactor flush times of 1.7-2.3 s and 0.3-0.4 s estimated from the reactor volume calculations and Equation (36).

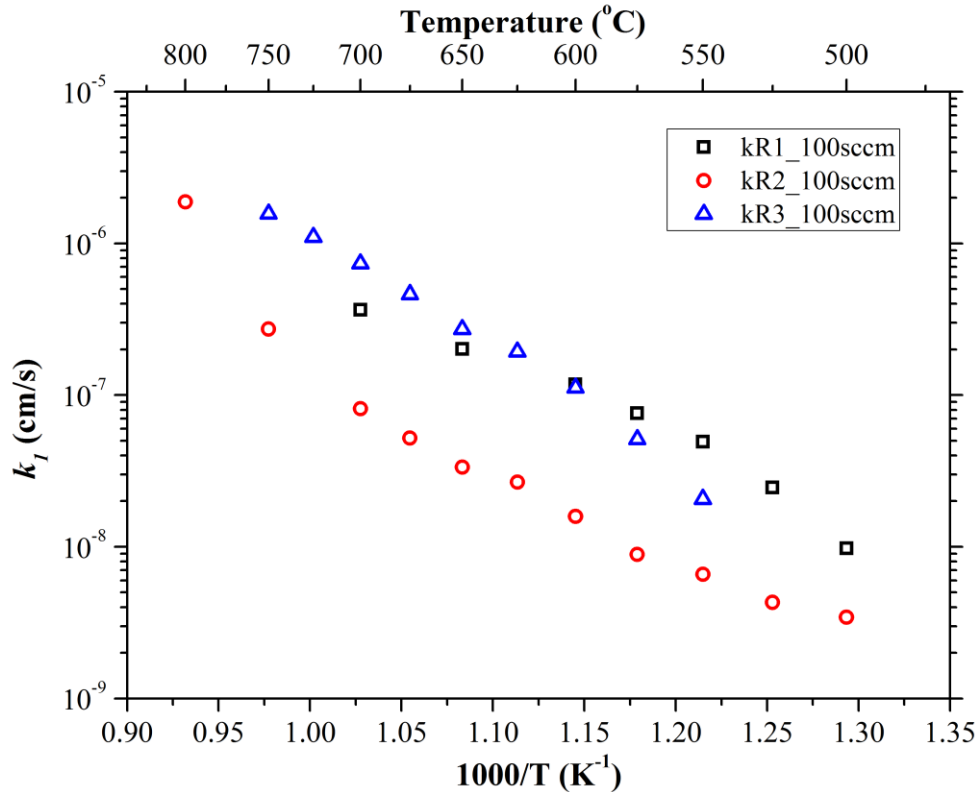


Figure 6.6 κ R-measured k values of LSF64/YSZ across multiple thermal segments at a flow rate of 100 sccm.

Figure 6.6 shows the κ R-measured oxygen surface exchange coefficients as a function of inverse temperature with multiple thermal cycling between 800°C and 500°C. Hysteresis of the measured k values was observed across multiple thermal segments, where k values of the two cooling segments (kR1 and kR3) were similar but 0.5-1 order of magnitude larger than the heating segment (kR2). Although further study is needed, this phenomenon may be related to changes of electronic structure, cation segregation, and/or dislocation density in the film, all of which can impact the ionic transport kinetics, as discussed in Section 2.3 [51, 165, 166, 168, 213, 214]. *In-situ* investigations on the compositional and structure changes at the film surface are also needed to provide better understanding of this behavior.

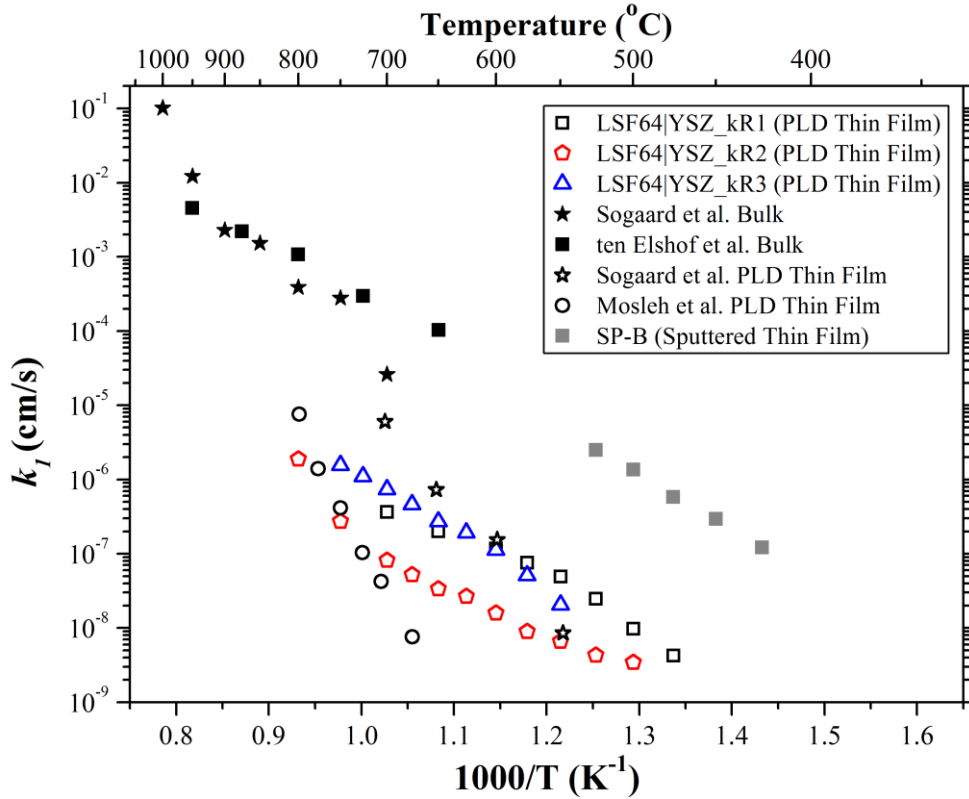


Figure 6.7 κR -determined k values of LSF64|YSZ compared with those in the literature [47-50] and the sputtered thin films in this work.

Figure 6.7 shows how the k values of the PLD LSF64|YSZ thin films obtained via κR compared to those available in the literature, as well as a representative dataset of the sputtered thin films from Chapter 5. The PLD k values are almost 2 orders of magnitude lower than those of the sputtered thin films, and 2 orders of magnitude lower than low temperature extrapolations of the literature bulk samples. However, the PLD k 's measured via the κR technique are similar in magnitude to the PLD thin film measurements from the literature. Due to the hysteresis behavior, the activation energy of the PLD thin film k 's is not constant across the entire temperature range (1.2 eV, 1.0 eV and 1.6 eV for kR1, kR2 and kR3, respectively), but generally shows similar values below 700°C compared to sputtered thin films and bulk samples in the literature. Still, these activation energies are much smaller than the incredibly large 4.7 eV

activation energy reported for PLD thin films in the literature. Effects such as film stress state and substrate identity are possible reasons for this discrepancy, but further study is needed to understand these differences.

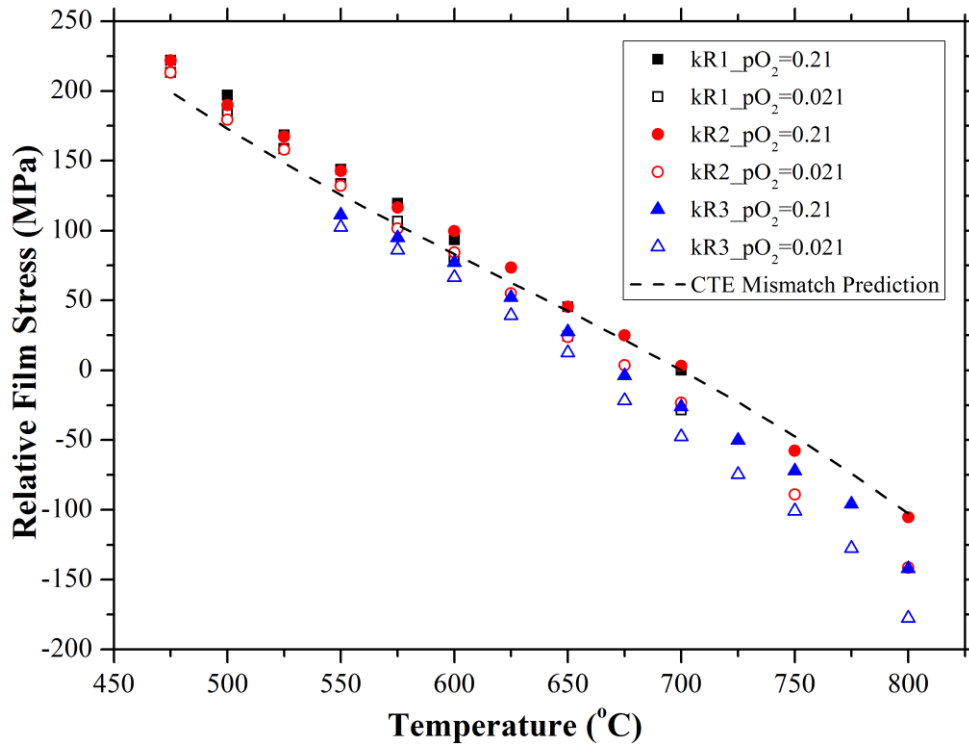


Figure 6.8 Average equilibrium stress levels of the PLD LSF64 thin film as a function of pO_2 and temperature. The dashed lines represent thermal expansion mismatch induced stress, based on coefficient of thermal expansion (CTE) and elastic constants of YSZ and LSF64 available in the literature [193, 194]. 700°C was chosen as the stress-free state in line with the film deposition temperature.

Figure 6.8 shows the equilibrium stress of the PLD thin film as a function of temperature compared to the stress expected from the coefficient of thermal expansion (CTE) mismatch between LSF64 [193] and YSZ [215]. 700°C was chosen as the stress-free state because this was the deposition temperature of the film. General agreement is observed between the measured and the CTE mismatch predicted stresses. The stress level at 800°C and $pO_2 = 0.021$ approached nearly 180 MPa in compressive nature, in contrast to a tensile stress of ~ 220 MPa at 475°C . The

slight drift of the stress state towards the compressive direction was observed from kR1 to kR3, which may be caused by one or more of the effects (changes of electronic structure, cation segregation, and/or dislocation density in the film) discussed previously.

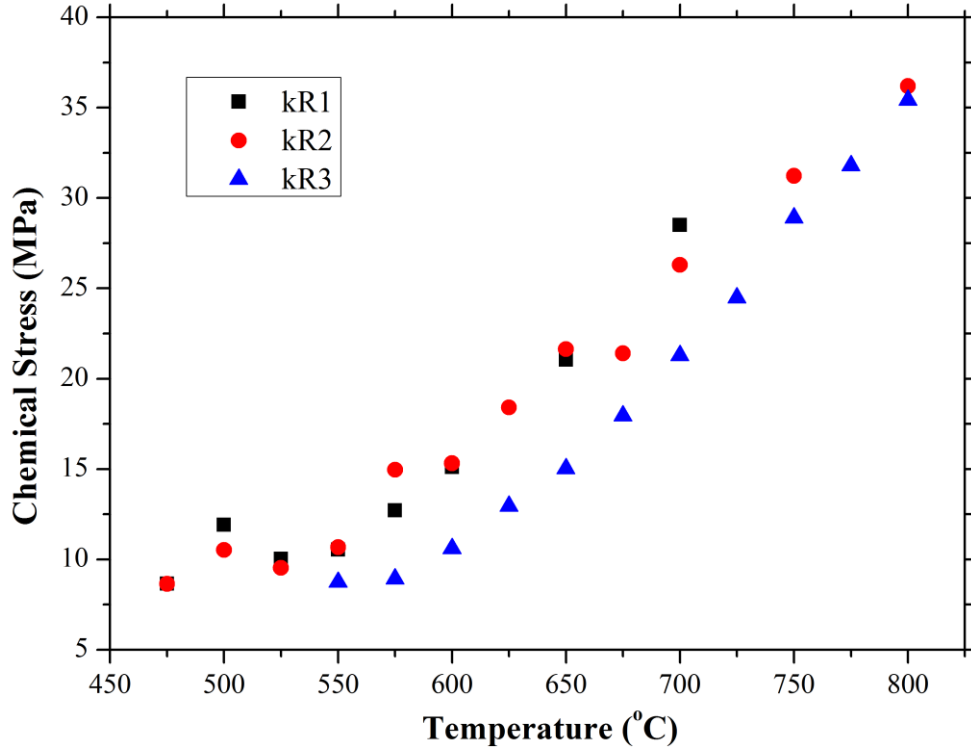


Figure 6.9 Chemical stress of the PLD thin film LSF64/YSZ induced by pO_2 changes between 0.21 and 0.021 as a function of temperature.

Figure 6.9 shows the chemical stress of the PLD LSF64 thin film induced by switching between $pO_2=0.21$ and $pO_2=0.021$ across all three thermal segments. Consistent with the behavior of large-grained LSF shown in Chapter 5 and in the literature [49, 193], a nearly linear relationship between the chemical stress and the temperature is observed above 525°C . The sub- 525°C chemical stresses are smaller than those of the sputtered films, consistent with (1) the interpretation that the sub- 525°C chemical stress is controlled by grain boundary expansion, and (2) the larger grain size of the PLD films (~ 52 nm) compared to those of the sputtered films (43

nm). For unknown reasons, a slight reduction of chemical stress was also shown for the third thermal segment (kR3) compared to kR1 and kR2.

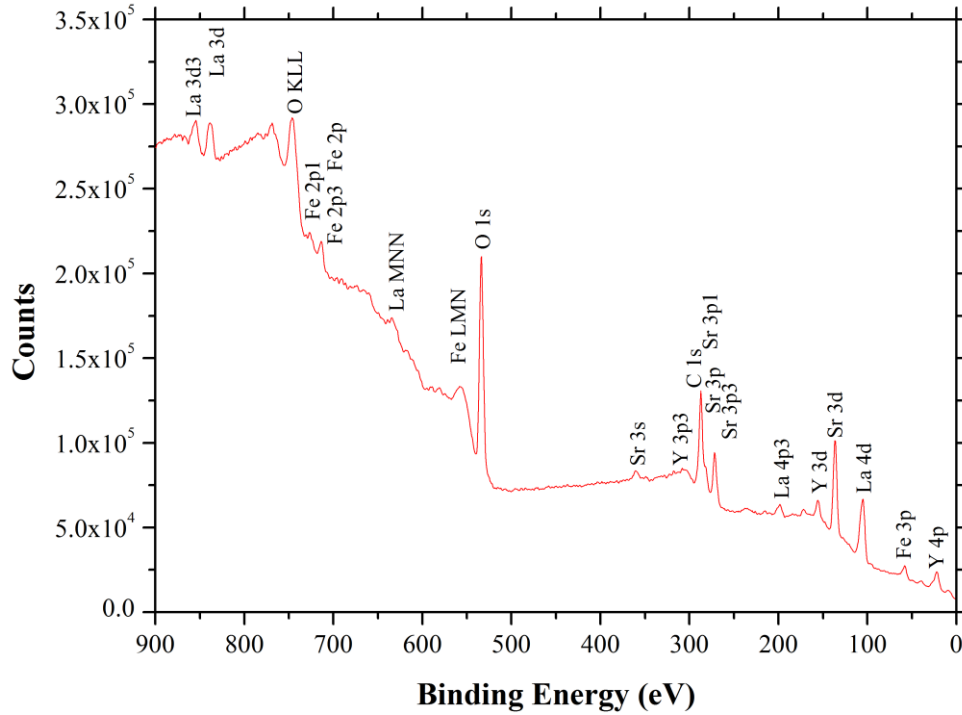


Figure 6.10 X-ray photoelectron spectroscopy (XPS) measurements of a PLD LSF64/YSZ sample.

Table 5 XPS measurement on the PLD LSF64/YSZ thin film after κR testing.

	La	Sr	Fe	Y	La:Sr:Fe ratio
Atomic Fraction (%)	0.78	7.46	2.61	1.06	0.30:2.86 : 1

Figure 6.10 and Table 5 show the XPS measurement on the PLD LSF64/YSZ sample. Significant Sr enrichment and La depletion were measured at the surface, a commonly observed phenomenon in the literature [213, 216, 217]. In addition, a significant amount of Y was also found at the surface, indicating cation diffusion from the YSZ substrate. Compared to the

La:Sr:Fe ratio of 1.19:1.47:1 observed for the sputtered thin film SP-A, a greater amount of Sr surface segregation was observed in the PLD film.

6.3.2 LSF64|SDC|YSZ

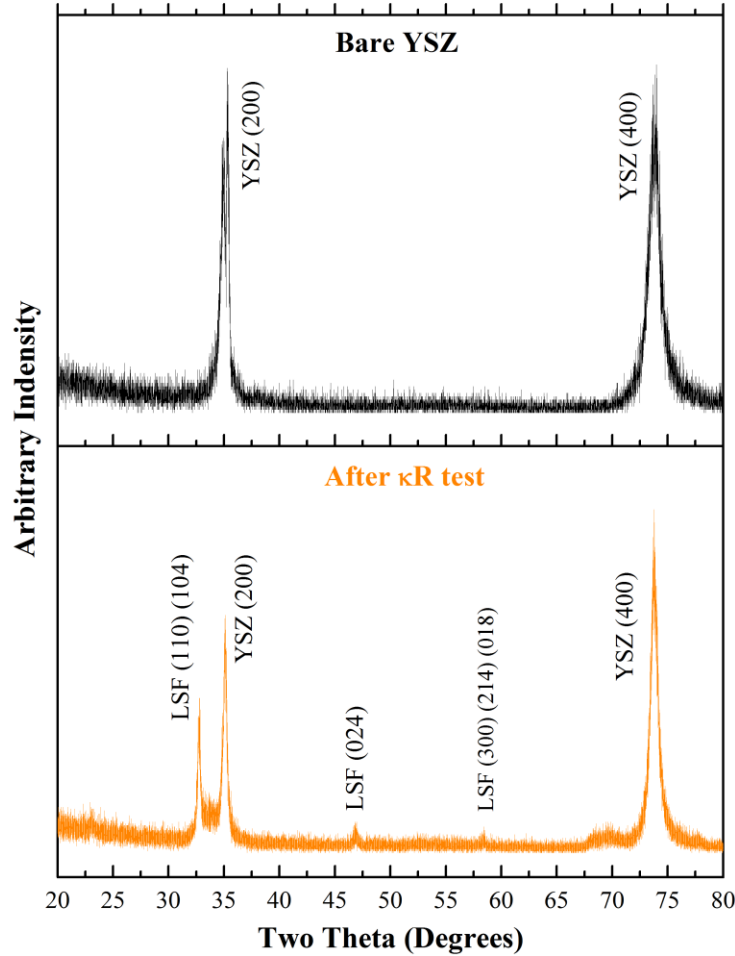


Figure 6.11 X-ray diffraction scans of the PLD LSF64|SDC|YSZ before and after κ R test. Peak indexing was obtained from PDF # 01-082-1961 for LSF64 and 01-070-4436 for YSZ.

As shown in *Figure 6.11*, PLD thin film LSF64|SDC|YSZ exhibits epitaxial features similar to LSF64|YSZ, with (110) (104) as the main orientations. Small peaks corresponding to the (024) orientation of LSF64 were also observed. No impurity phase peaks were observed. Williamson-Hall grain size estimation was not available for this sample due to the LSF-YSZ

peak convolution, but the grain size of this film should be similar to 52 nm determined for the LSF64|YSZ sample given the similar XRD line broadening.

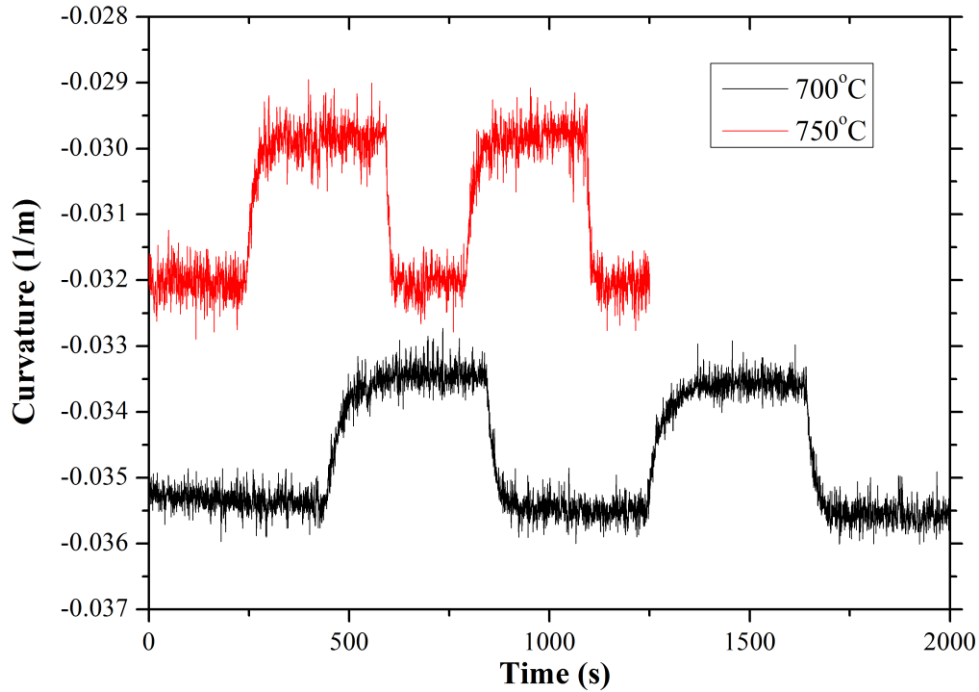


Figure 6.12 Multiple curvature relaxation cycles of the LSF64|SDC|YSZ sample at 700°C and 750°C between $pO_2=0.21$ and $pO_2=0.021$. The difference in equilibrium curvature levels between the two temperatures is a result of the film-substrate thermal expansion mismatch.

Similar to the LSF64|YSZ sample, the multiple κR cycles of the LSF64|SDC|YSZ thin film shown in *Figure 6.12* indicate reproducible relaxation kinetics and equilibrium curvature levels for multiple isothermal relaxations. This indicates that oxygen nonstoichiometry changes in the PLD LSF64|YSZ thin film were reversible as the atmosphere pO_2 was changed, and that no significant film cracking or delamination occurred. In contrast to the sputtered films described in *Chapter 5*, but similar to the LSF64|YSZ sample, only one relaxation time constant was observed at all temperatures, as demonstrated in *Figure 6.13*, indicating that only one surface

exchange process dominated during the κR experiments. Identical $\text{Ln}[1-g(t)]$ analysis at all other tested temperatures yielded similar results.

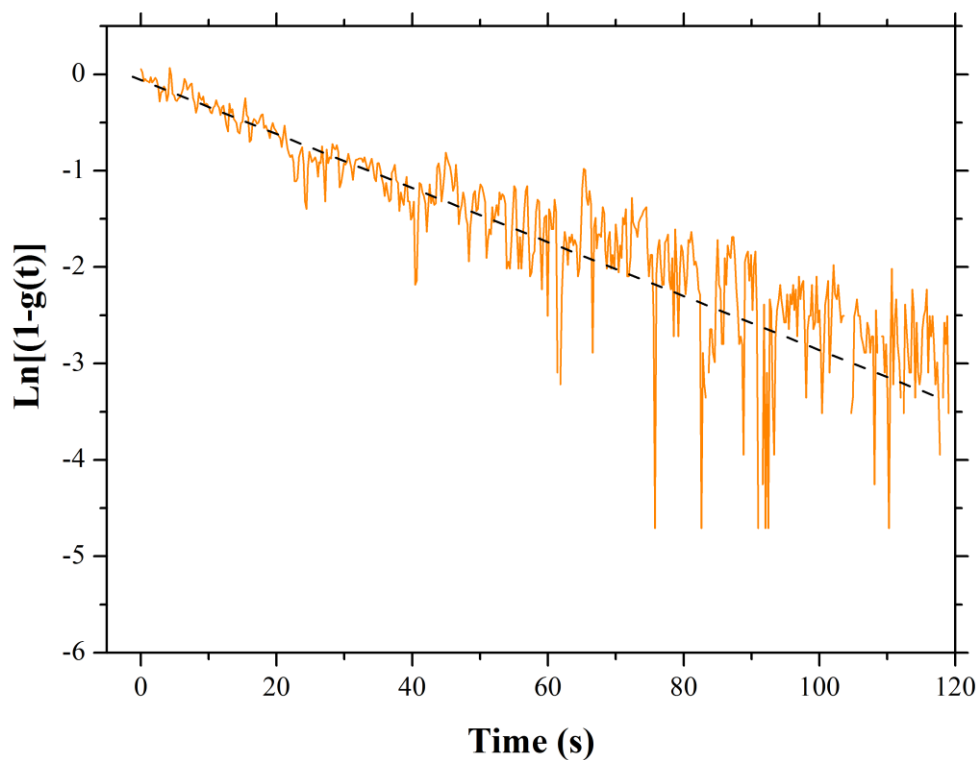


Figure 6.13 Representative κR data of 700°C on reduction shown in Figure 6.14 replotted on a semi-log plot, and showing only one time constant. κR data of other temperatures showed similar single time constant behavior.

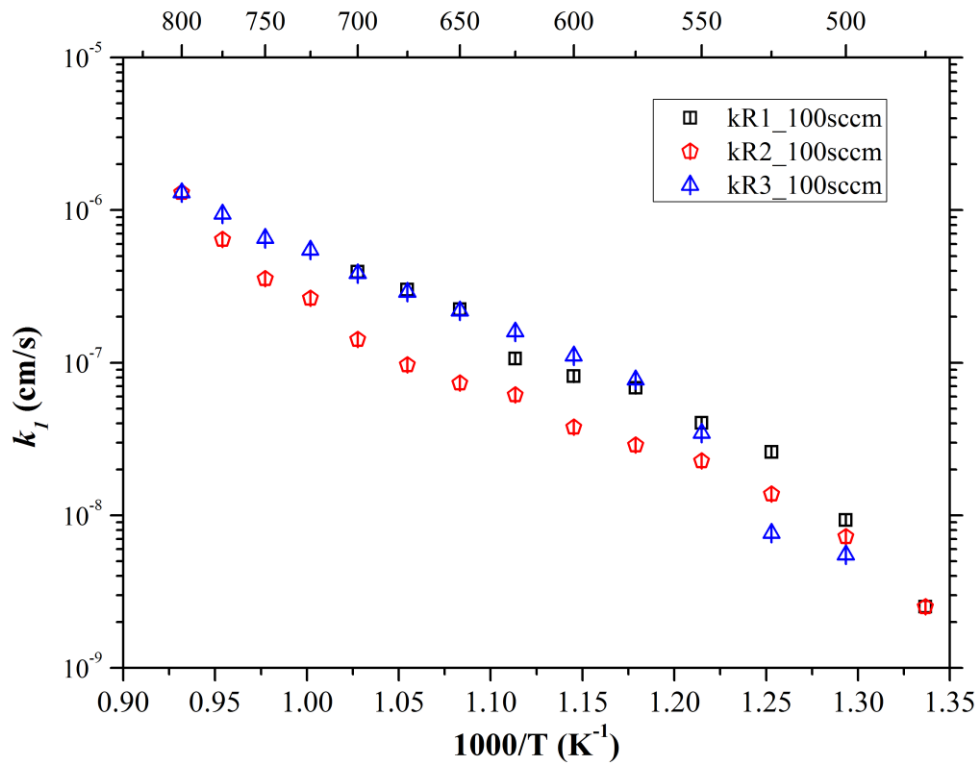


Figure 6.14 κ R-measured k values of LSF64/SDC/YSZ across multiple thermal segments at a flow rate of 100 sccm.

Figure 6.14 shows the κ R-measured k 's of LSF|SDC|YSZ as a function of inverse temperature. Comparing to LSF|YSZ, reduced hysteresis behavior of the measured k values was observed in the LSF|SDC|YSZ sample across multiple thermal segments.

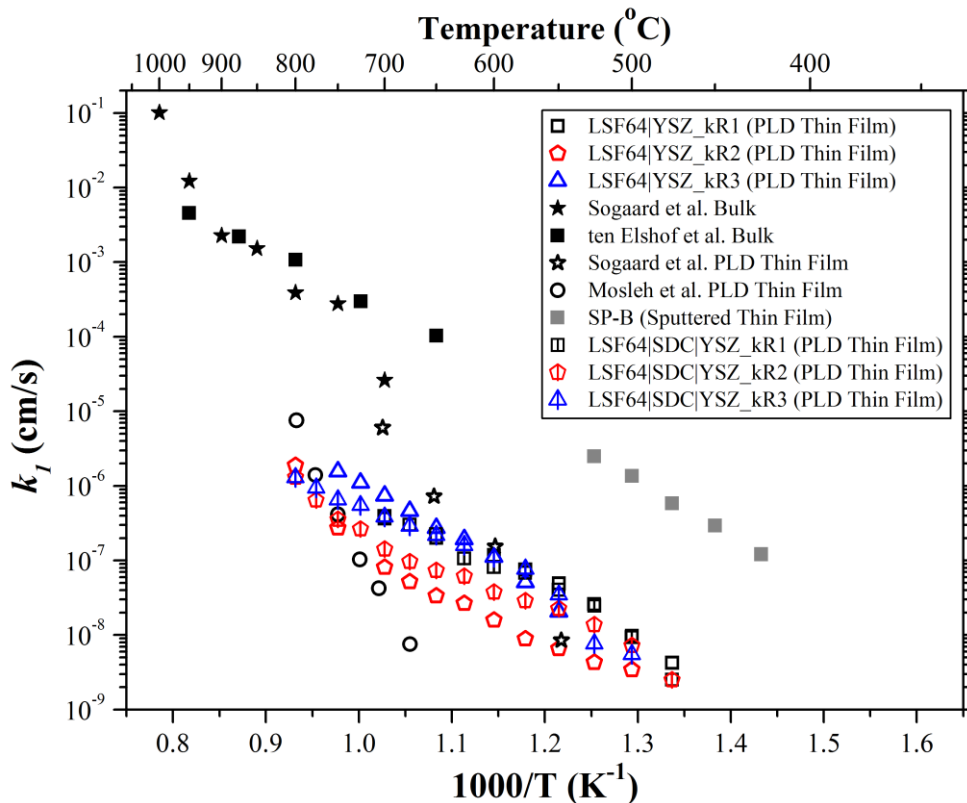


Figure 6.15 κR -determined k values of PLD LSF64 thin films compared with those in the literature [47-50] and the sputtered thin films in this work.

Figure 6.15 shows the comparison between the k values of the two PLD LSF64 thin films obtained via κR and those available in the literature, as well as a representative dataset of the sputtered thin films in this study. The magnitude of k 's was similar between LSF64|YSZ and LSF64|SDC|YSZ, and also close to the PLD thin film measurements from the literature. The activation energy of LSF64|SDC|YSZ k 's below $700^{\circ}C$ was 1.1 eV, 1.0 eV and 1.4 eV for kR1, kR2 and kR3, respectively and similar to those of LSF64|YSZ. However, the LSF|SDC|YSZ sample showed slightly less hysteresis during the second thermal segment (kR2). Possible reasons for this behavior are found in the XPS results presented later in this section.

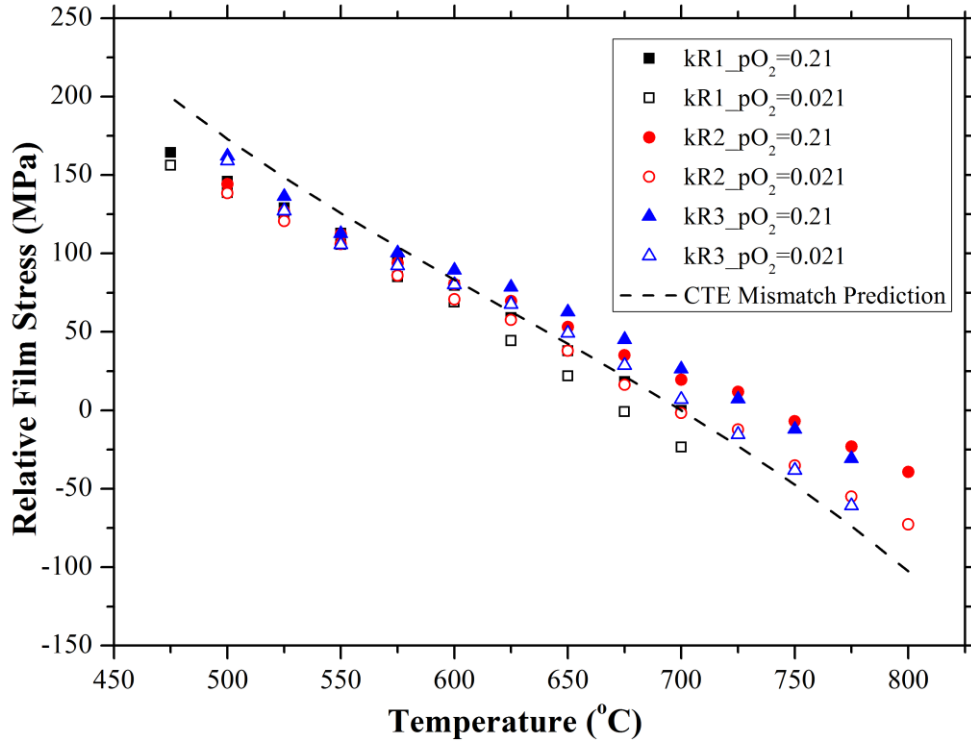


Figure 6.16 Average equilibrium stress levels of the PLD thin film LSF64/SDC/YSZ as a function of pO_2 and temperature. The dashed lines represent thermal expansion mismatch induced stress, based on coefficient of thermal expansion (CTE) and elastic constants of YSZ and LSF64 available in the literature [193, 215]. $700^\circ C$ was chosen as the stress-free state in line with the film deposition temperature.

Figure 6.16 shows the equilibrium stress of the PLD thin film LSF64|SDC|YSZ as a function of temperature compared to the stress expected from the coefficient of thermal expansion (CTE) mismatch between LSF64 and YSZ. For lack of an absolute reference, $700^\circ C$ was chosen as the stress-free state because this was the deposition temperature of the film. General agreement is observed compared to the CTE mismatch predictions, as well as the LSF64|YSZ sample.

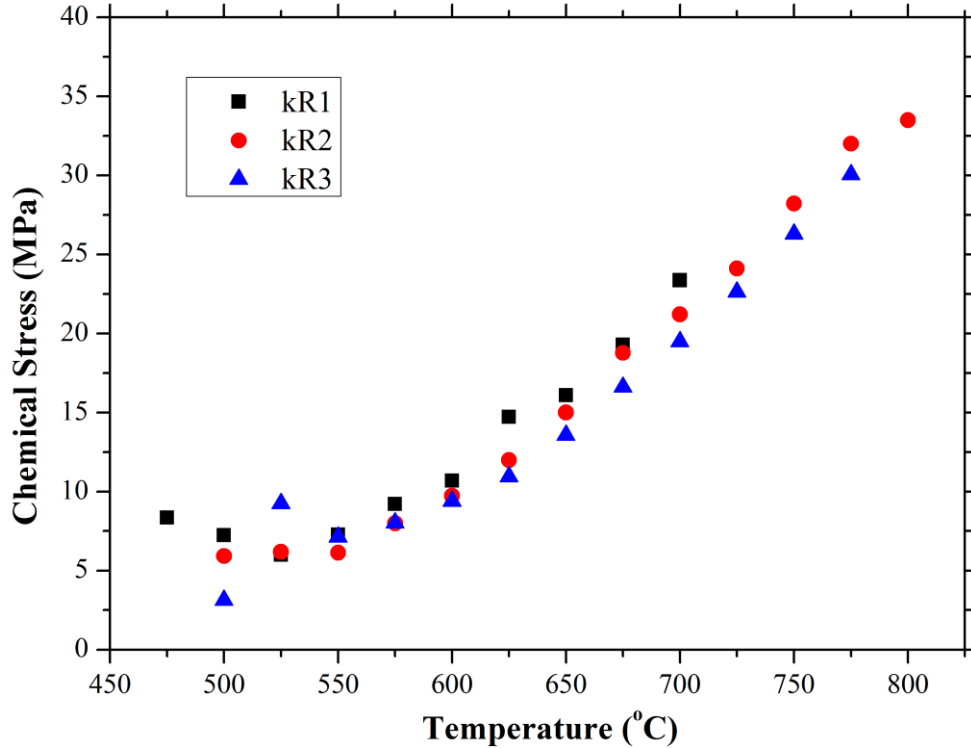


Figure 6.17 Chemical stress of the PLD thin film LSF64|SDC|YSZ induced by pO_2 changes between 0.21 and 0.021 as a function of temperature.

Figure 6.17 shows the chemical stress of the PLD thin film LSF64|SDC|YSZ induced by switching between $pO_2=0.21$ and $pO_2=0.021$ across all three thermal segments. Non-zero chemical stress levels were again observed for all temperatures, and the magnitude of these stresses resemble those measured for the LSF|YSZ sample.

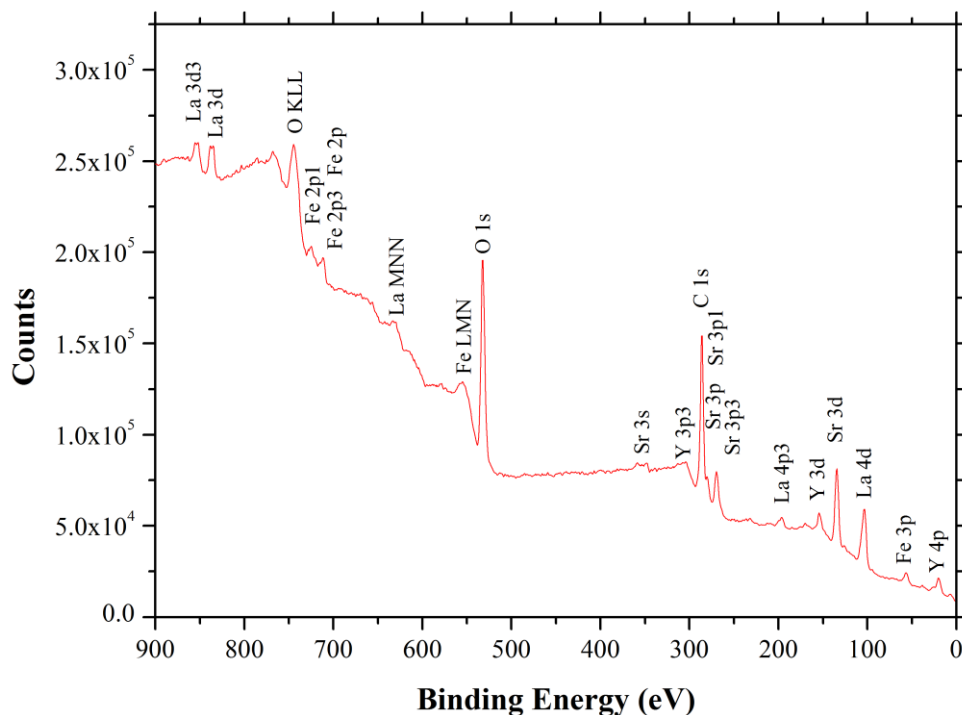


Figure 6.18 X-ray photoelectron spectroscopy (XPS) measurements of a PLD LSF64/SDC/YSZ sample.

Table 6 Comparison of XPS measurements on the PLD LSF64/YSZ and LSF64/SDC/YSZ thin films and the sputtered LSF64|8YSZ film after κ R testing.

		La	Sr	Fe	Y	La:Sr:Fe ratio
Atomic Fraction (%)	LSF64 8YSZ (SP-A) after κ R test	2.66	3.30	2.24	0.11	1.19 : 1.47 : 1
	LSF64 YSZ after κ R testing	0.78	7.46	2.61	1.06	0.30: 2.86 : 1
	LSF64 SDC YSZ after κ R testing	0.60	5.12	2.10	0.92	0.29 : 2.44 : 1

Figure 6.18 and Table 6 show the XPS measurement on the PLD LSF64|SDC|YSZ sample, and compare the atomic fractions of cations between LSF64|SDC|YSZ and LSF|YSZ as well as the sputtered thin film LSF|YSZ. Significant Sr segregation was also observed at the surface of LSF|SDC|YSZ. The similarities and differences of surface composition between the

two PLD films indicate that the hysteresis behavior observed in k measurements may be caused by Sr and/or Y surface segregation. Additional work is needed to understand the underlying causes for the hysteresis behavior observed in PLD LSF64 thin films

6.4 Conclusions

Stress and oxygen surface exchange coefficients were simultaneously measured on pulsed laser deposited LSF64 thin films using the curvature relaxation technique developed in this work. The stress and oxygen surface exchange coefficients of PLD LSF64 thin films were measured with thermal cycling first time. The magnitude of the PLD k values were consistent with literature reported PLD thin films with the same composition, but are 2 orders of magnitude lower than the sputtered thin films measured in this work as well as literature bulk LSF64 sample low temperature extrapolations. This indicates that the 5-order of magnitude k discrepancies in the literature is not caused by the electrodes used previously measure the k 's of LSF64 PLD films. A hysteresis behavior in k values was observed for the first time in both PLD thin films LSF|YSZ and LSF|SDC|YSZ upon thermal cycling, and may be caused by cation segregation to the surface of the film. Although the measured film stress levels were similar to sputtered films in magnitude, ferroelastic domain switching due to film yielding was not present, as indicated by the linear temperature dependence of the film stress. This is consistent with the single (110) dominated orientation of the films.

These κ R experiments demonstrate how microstructure and processing techniques may affect the stress and surface exchange kinetics of MIEC thin films with the same chemical composition, and provide additional insights towards understanding the relationship between surface exchange mechanisms and the microstructure.

7. Oxygen Surface Exchange and Stress Measurements on Spray Deposited LSF64 Porous Thick Films

7.1 Introduction

In this chapter, stress and k were simultaneously measured on porous MIEC thick films for the first time. Specifically, the κ R technique was used on LSF64|13YSZ bilayers to gain a deeper understanding of the k variations resulting from LSF64 films with different processing histories, morphologies, and stress states.

7.2 Experimental

7.2.1 Sample Fabrication

LSF64 powder synthesis and porous film fabrication procedures were detailed in *Sections 3.2.1 and 3.2.5*. 13YSZ substrates were chosen to avoid the cubic-to-tetragonal transformation of the substrate (which is known to occur in yttria doping levels below 8%) [204] that could complicate the curvature and film stress measurement.

7.2.2 Porous Pellet Dilatometry

In order to understand the densification behavior of the porous LSF film and ensure that no sintering occurred during κ R experiments, a porous, 12.7 mm diameter cylindrical pellet was prepared by uniaxially cold pressing the calcined LSF64 powder at 13 MPa in a stainless steel die. The resulting 9.25 mm-long pellet was then loaded into the dilatometer, followed by the same sintering schedule as the porous film (1050°C for 1 hour, with heating and cooling rates both 5°C/min), under 50 sccm continuously flowing air.

7.2.3 Curvature Relaxation Measurements

Immediately after sintering at 1050°C for 1 hour inside the MOSS apparatus, the bilayers were cooled down to 700°C in air followed by κ R experiments between air (Airgas, $p_{O_2}=0.21$) and of 2.1% O₂-97.9% N₂ mixture (Airgas, $p_{O_2}=0.021$) controlled by a four-way valve. Relaxation experiments under both a 100 sccm and a 500 sccm flow rate were conducted to identify the temperature range where reactor flush time limitations were present. At temperatures between 700°C and 400°C, the 10 mL chamber reactor volume determined from *Chapter 5* corresponded to a flush time ranging from 1.8 seconds to 2.7 seconds for 100 standard cubic centimeters/ minute (sccm) and from 0.37 seconds to 0.53 seconds for 500 sccm flow rate [181]. Based on the need for a relaxation time larger than 5 times the reactor volume flush time in order to correctly extract oxygen surface exchange coefficients [181], these reactor flush times allowed accurate k measurements to be obtained in those situations where the relaxation time constants were larger than 11 seconds and 2 seconds for the 100 sccm and 500 sccm flow rates, respectively.

For the porous thick films studied here, k was extracted from κ R data using the measured film porosity, the film surface area, and Equation (34). Thickness-averaged film stresses were obtained using the modified version of Stoney's Equation for arbitrary film thickness shown in Equations (38)-(40).

7.2.4 Structural and Morphological Characterization

SEM and XRD analysis before and after κ R experiments utilized the same conditions as those for the sputtered films, described in *Section 5.2.3*. Grain size was estimated using the line intercept method on micrographs of the film surface after κ R testing. FIB-SEM 3D

reconstructions were performed using the procedures detailed in *Section 3.4.2* to obtain microstructure parameters (V_V and S_V) of the porous films.

7.3 Results and Discussion

The sintering behavior of a porous LSF bulk sample (as shown in *Figure 4.3*) undergoing similar thermal conditions as the porous thick film indicated that no sintering occurred during porous film κR measurements between 250-700°C.

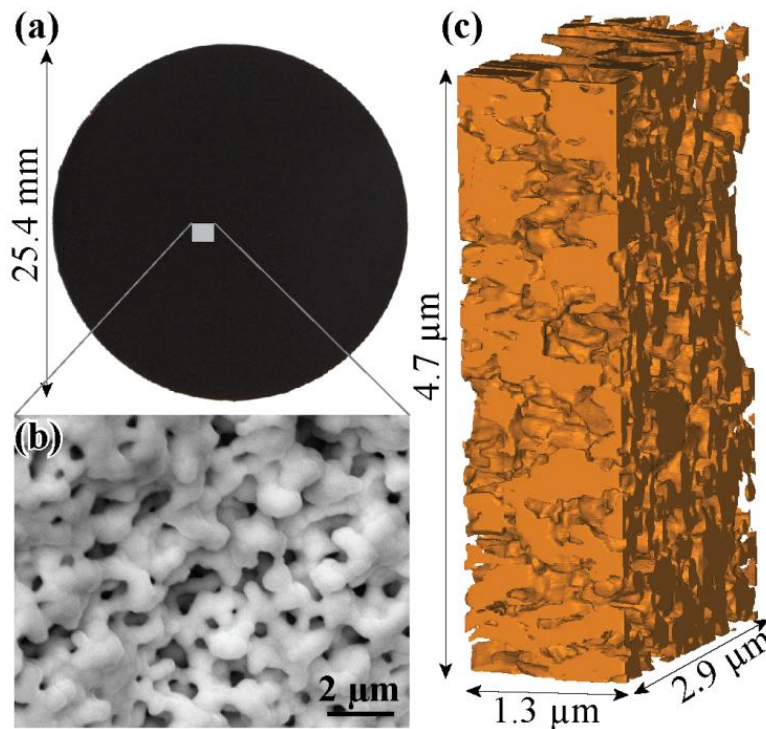


Figure 7.1 (a) Picture of the top surface of a κR -tested LSF64 porous thick film on a 25.4 mm diameter YSZ substrate, (b) SEM image of the top surface of a LSF film, and (c) a FIB-SEM 3D reconstruction. The film thickness is 5 μm and aligned in the upward direction.

Figure 7.1 shows the morphology and microstructure of a κR -tested LSF64 film on the rough side of a 25.4 mm diameter, one side polished 13YSZ substrate. The porous film was crack-free, uniform in thickness, and had well-necked particles. The size of these particles were

well below the reported characteristic thickness of LSF64, which is $>100 \mu\text{m}$ below 800°C [47, 49]. With rapid gas transport through the pores, this ensured that surface exchange dominated oxygen transport in the film (i.e. transport of oxygen through the bulk of the particles was significantly quicker than that across the gas/particle interface) in the temperature range of this study, and therefore the use of Equation (30) was legitimate to extract k [218]. From the FIB-SEM 3D reconstruction of the porous film, it was determined that $V_V = 50.7\%$ and $S_V = 0.024 \text{ nm}^{-1}$. Reconstruction of halves and quarters of the volume showed consistent V_V and S_V values within the margin of error (i.e. $<5\%$), indicating that the volume in *Figure 7.1* (c) is microstructurally representative. The particle size of the porous film after κR testing was determined to be $400 \pm 10 \text{ nm}$ using the line intercept method on *Figure 7.1* (b).

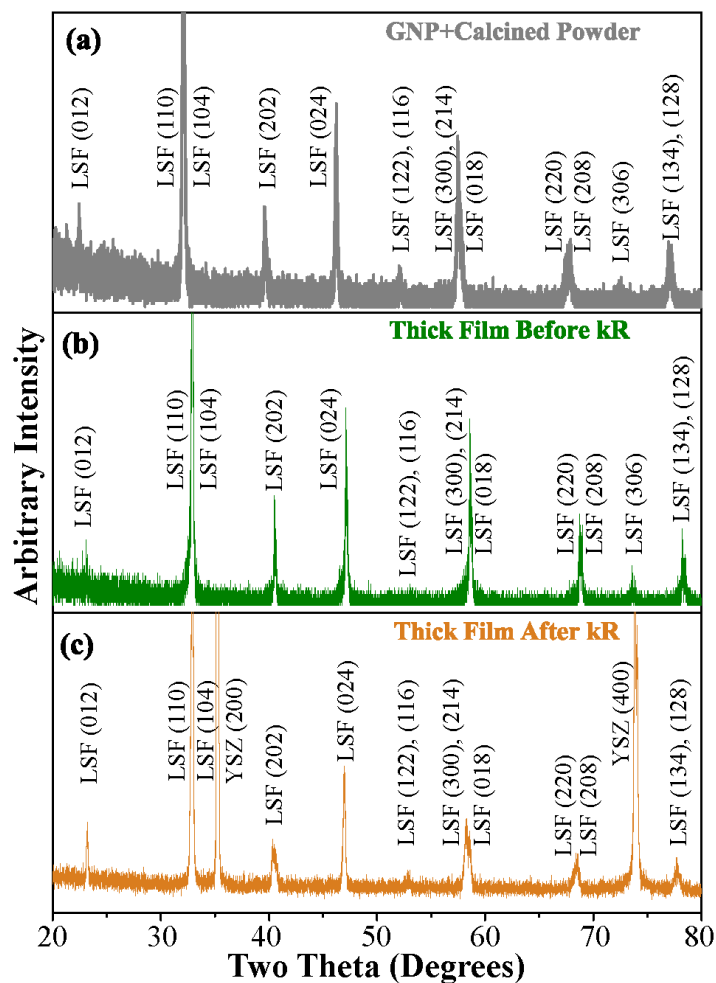


Figure 7.2 X-ray diffraction of (a) the LSF64 powder after calcination at 1000°C for 1h, (b) a LSF64|YSZ bilayer before κ R testing and (c) a LSF64|YSZ bilayer after κ R testing. XRD peak indexing was performed using LSF64 PDF # 01-082-1961 and YSZ PDF # 01-077-2114.

Figure 7.2 shows X-ray diffraction data for a) the GNP-produced LSF64 powder after calcination, b) the as-deposited LSF64 thick film atop a YSZ substrate, and c) a κ R-tested LSF64 thick film atop a YSZ substrate. Peak indexing indicated that both the LSF64 powder and the LSF64 films were polycrystalline and consistent with all major peaks listed in LSF64 PDF # 01-082-1961. The (200) and (400) planes of the YSZ substrate were observed in κ R-tested thick film, but were not present in the as-deposited film. This is assumed to be caused by the reduced

film thickness after sintering and κ R testing. The observed YSZ peaks are consistent with the (100) orientation of the single crystal substrate.

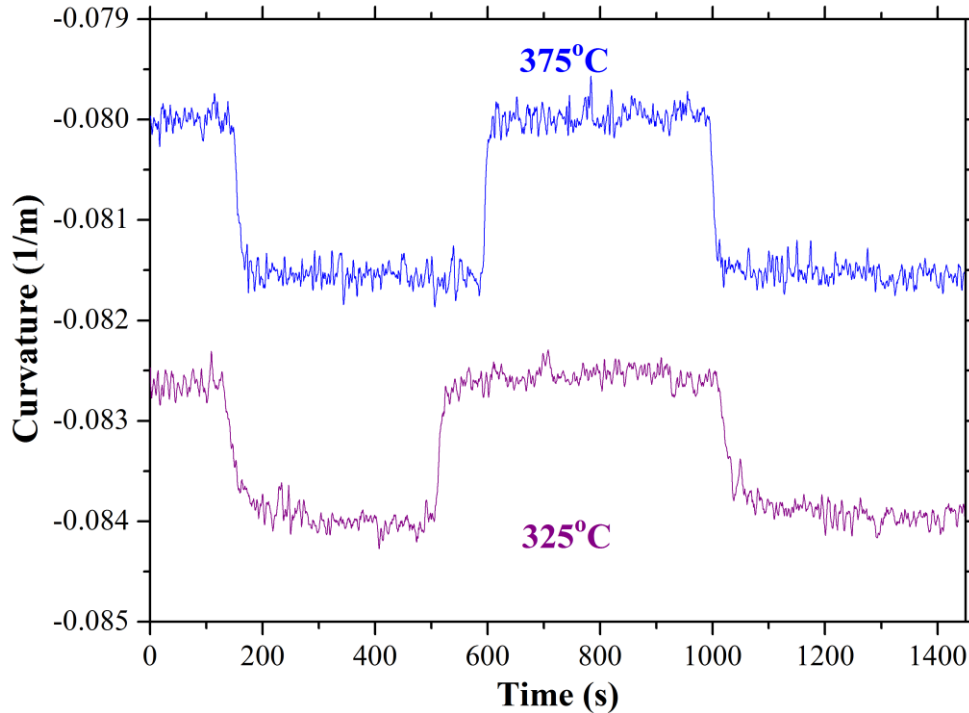


Figure 7.3 Multiple curvature relaxation cycles between $pO_2=0.21$ and $pO_2=0.021$, at 375°C (top) and 325°C (bottom).

Figure 7.3 shows the curvature relaxation of a LSF64|YSZ bilayer subject to multiple pO_2 cycles between 0.21 and 0.021 atm. It is readily seen that the curvature relaxation is faster at 375°C than 325°C due to the fact that oxygen surface exchange is a thermally activated process. The difference in equilibrium curvatures between two different temperatures is caused by the thermal expansion mismatch between LSF64 (~ 14 ppm/K) [193] and YSZ (9.4-9.5 ppm/K) [205]. The equilibrium curvature levels remain consistent across multiple pO_2 cycles, as is the case for all other temperatures analyzed, indicating that the oxygen nonstoichiometry changes were reversible and no other stress altering events like film cracking or delamination occurred to a significant extent. In contrast to the sputtered films described in *Chapter 5*, but similar to the

PLD films described in *Chapter 6*, only one relaxation time constant was observed. This is demonstrated in *Figure 7.4*, which shows that only one surface exchange rate was recorded during the κR experiment. Identical analysis at all tested temperatures (i.e. between 250°C to 700°C) yielded similar results.

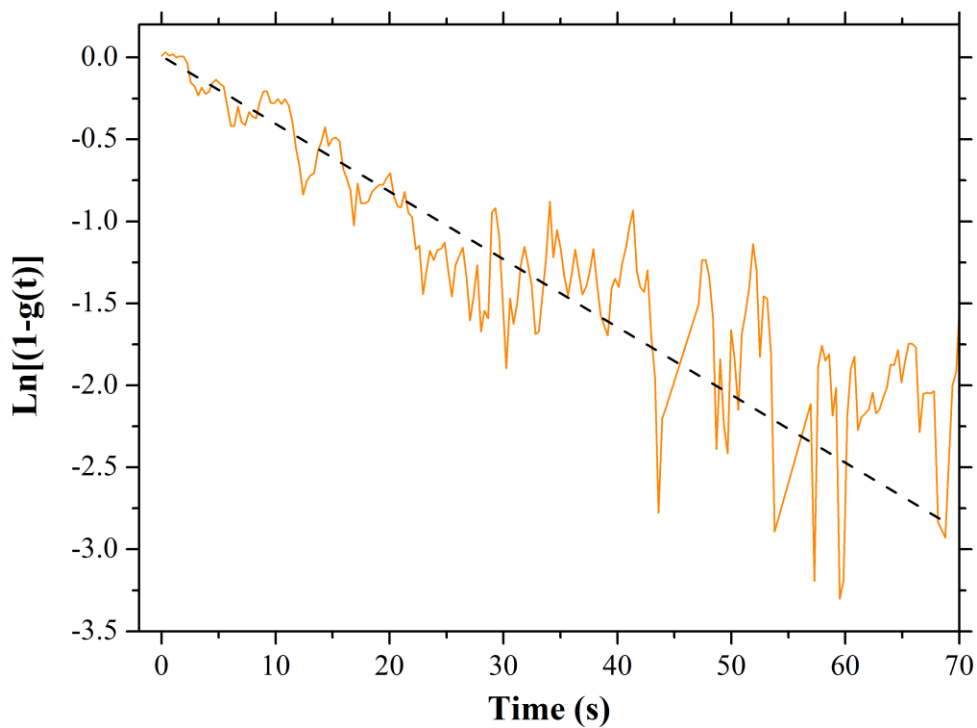


Figure 7.4 Representative κR data of 325°C on reduction shown in *Figure 7.3* replotted on a semi-log plot, and showing only one time constant. κR data of other temperatures showed similar single time constant behavior.

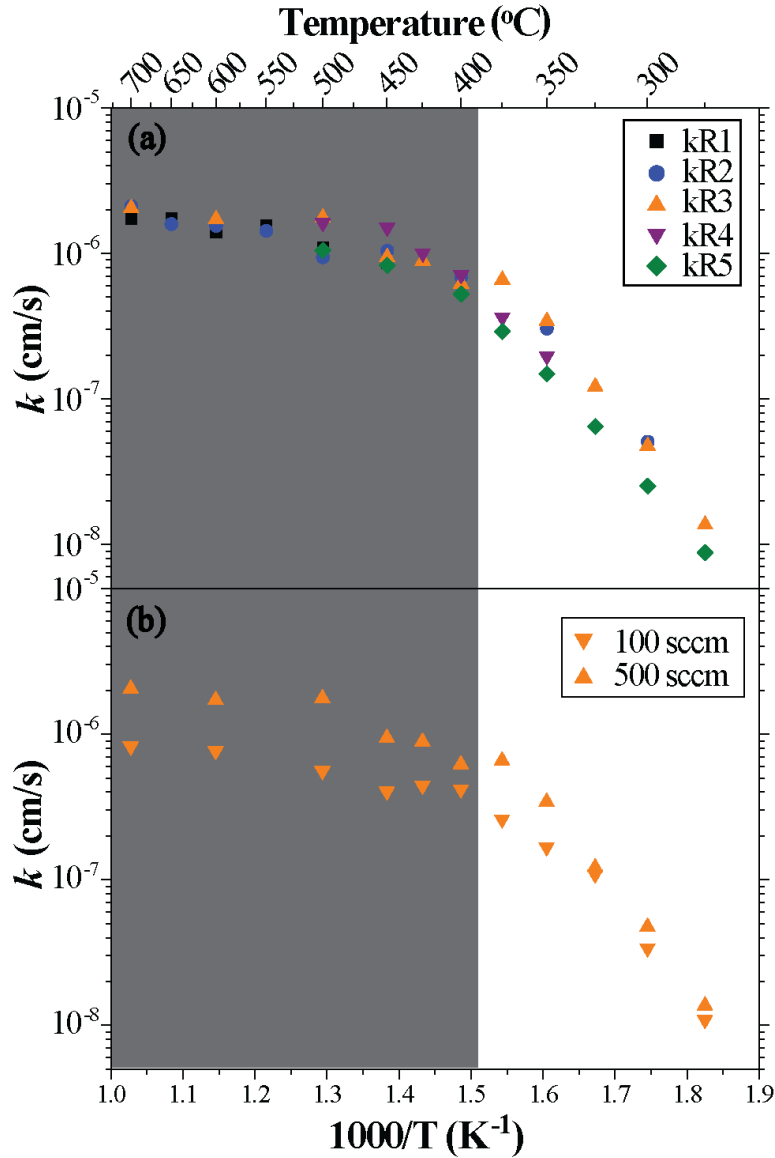


Figure 7.5 k measurements (a) under 500 sccm flow rate across multiple thermal segments $\kappa R1$ - $\kappa R5$ and (b) under different flow rates at $\kappa R3$. Errors of k 's are smaller than the symbols. The numbers are in chronological order of experiments, where 1, 3 and 5 are measurements during sample cooling, 2 and 4 are during sample heating. Open and solid symbols denote k measurements with and without flush time limitations, respectively. As indicated by the grayed out region, reliable k measurements could not be obtained above 375°C due to reactor flush time limitations.

Figure 7.5 shows that k measurements across multiple thermal cycles were generally reproducible. This suggests that phase transitions [193], ferroelastic domain switching [209], irreversible cation surface segregation [219], and other unaccounted for possible stress relaxation

processes did not occur with thermal cycling between 250-700°C, and therefore had no significant effect on k .

Further, as indicated by the identical k values for a 100 and 500 sccm flow rate below 325°C and a single, 500 sccm k slope below 375°C, flush time limitations are not present below 375°C when a 500 sccm gas flow is used. Above 375°C, the measured k 's exhibit an activation energy of 0.16 eV and 0.18 eV for 100 sccm and 500 sccm flow rates, respectively, which is close to the theoretical 0.07 eV estimated from the reactor flush time limitation [181]. This indicates a reactor flush time dominated regime for temperatures $\geq 375^\circ\text{C}$. At lower temperatures where the flush time is much shorter than the time constants of the relaxations, reliable k measurements were obtained.

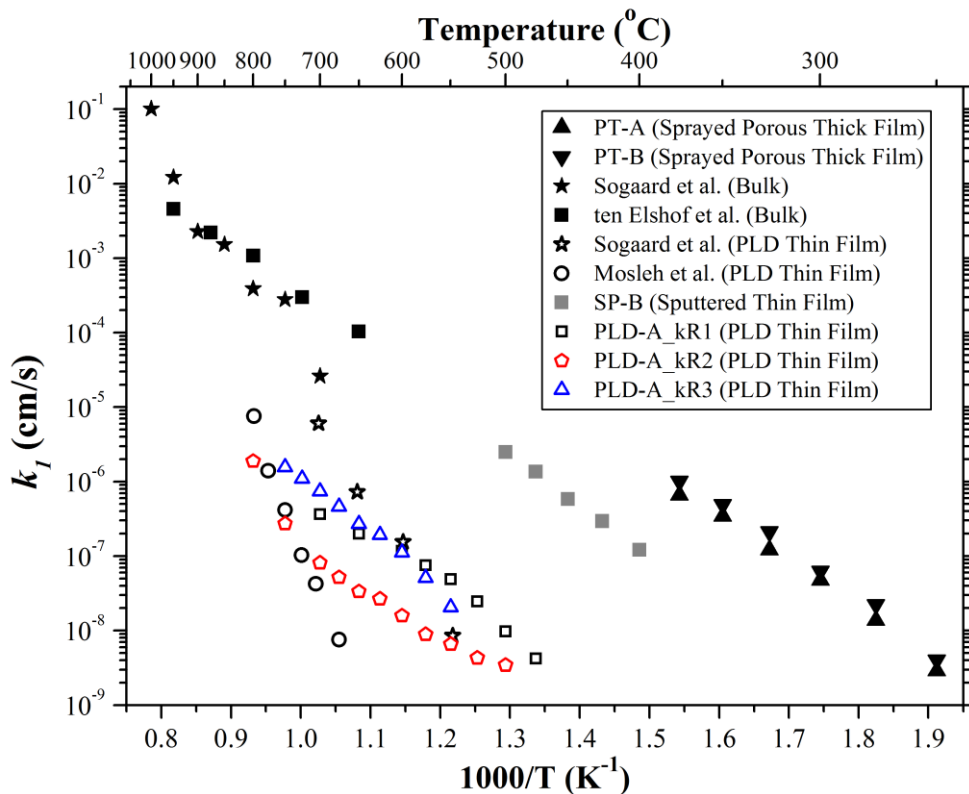


Figure 7.6 Surface exchange coefficients (averaged over the oxidation and reduction k 's) of the porous thick film LSF64 under 500 sccm for κR3 compared to other literature measurements [47, 49, 50, 220], as well as the sputtered and PLD thin films measured in this work. Only k_1 values are shown.

Figure 7.6 shows the Arrhenius behavior of the k 's measured by the κ R technique in comparison with other literature measurements on bulk and thin film LSF64 using various techniques. As shown in Figure 7.6 and reported in Yang and Nicholas [221], at temperatures $\leq 375^\circ\text{C}$, the porous thick film k 's exhibit an activation energy of 1.3 eV, consistent with the 1.3 eV activation energy reported by ten Elshof *et al.* on bulk LSF64, and the 1.1~1.4 eV activation energies reported by Yang *et al.* [220] and in Chapter 5 on sputtered thin film LSF64. This similarity may be because the polycrystalline, non-epitaxial nature of the porous thick film structurally resembles the bulk and sputtered LSF64 samples.

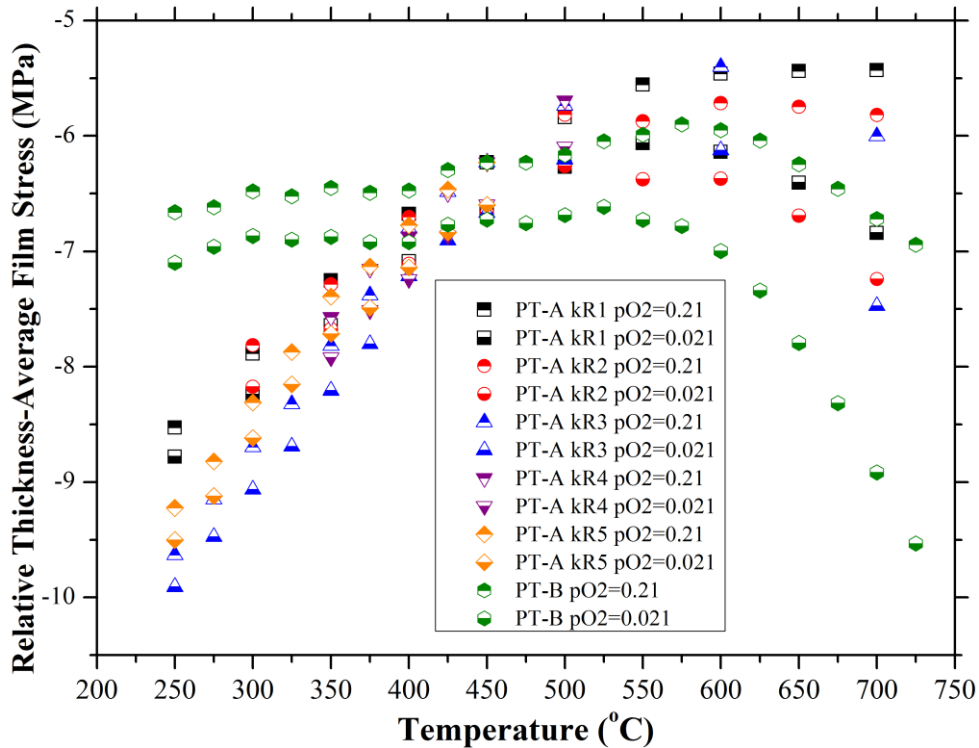


Figure 7.7 Estimated LSF64 thickness averaged film stress. Curvature/stress level of the bilayer prior to sintering (at room temperature) was chosen as reference of stress-free state.

Figure 7.7 shows thickness-averaged film stress measurements, $\lambda(z)$, extracted from equilibrium curvature levels based on Equation (41). These thickness-averaged film stresses do

not account for local stress variations caused by microstructure induced stress concentration through film particle necks. The elastic modulus of the porous film is estimated based on an exponential relationship with respect to the porosity, as seen in various studies on perovskite and fluorite materials [222-225]:

$$E = E_0 \exp(-b_E P) \quad (49)$$

where P is the volume fraction porosity, E_0 is the elastic modulus at $P=0$ and b_E is a material dependent constant. For the LSF64 porous film studied here, E_0 values of dense samples are obtained from Kimura et al., [226] and b_E is estimated to be 3.6 from that of $\text{La}_{0.6}\text{Sr}_{0.4}\text{Co}_{0.2}\text{Fe}_{0.8}\text{O}_{3-\delta}$ [222].

According to Equations (38)-(40), the thickness variation in z resulted in stress variation across the thickness of the film of less than 0.1 MPa between the LSF64|YSZ interface and the film top surface (not shown in plots here). This small effect introduces variations of stress measurements smaller than the symbol size. Linear stress levels are generally observed at temperatures between 725°C and 600°C, which is consistent with the relative linearity of the thermal expansion mismatch between LSF64 and YSZ. At temperatures below 600°C, the stress levels start to bend over and eventually become more compressive (less tensile) with decreasing temperature. This unexpected variation of the stress may be due to the small residual stress in the YSZ substrate that becomes noticeable in the porous thick films because these films are at much smaller stress states than the sputtered or PLD LSF64 films. The unusual low temperature stress-temperature behavior of these films, which varied from sample to sample, suggests that the 1100°C, 1-hour pre-deposition annealing cycle was not sufficient to relieve all the residual stress in the YSZ substrates. Future studies will investigate films deposited on higher temperature annealed YSZ wafers.

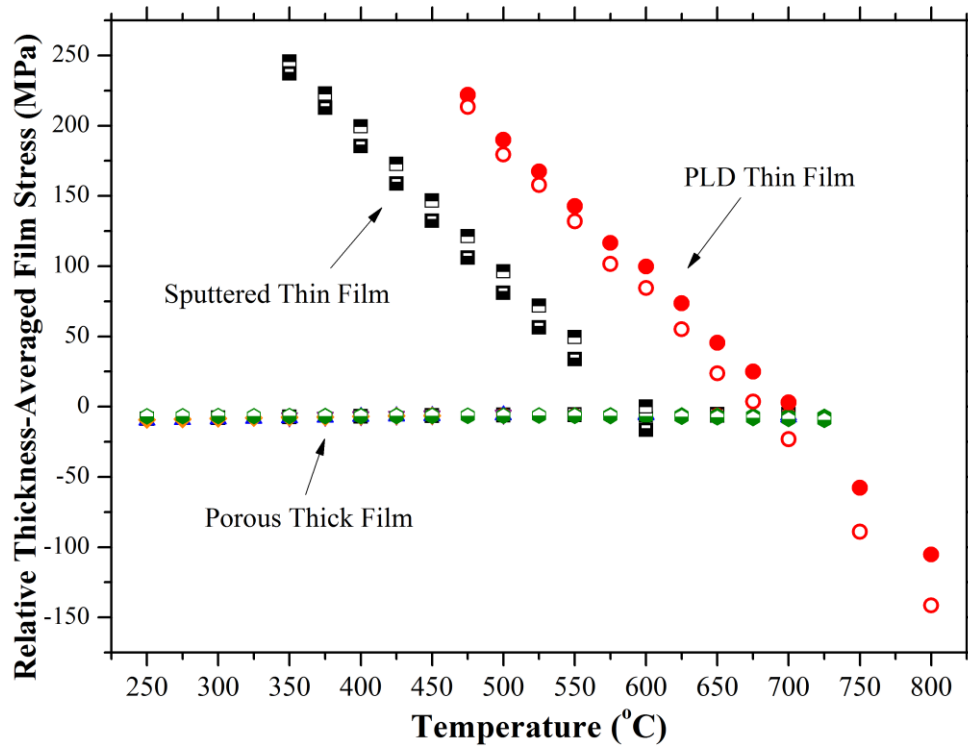


Figure 7.8 Thickness average film stress of the LSF64 porous thick films compared to representative film stresses as found in the sputtered and PLD thin films measured in this work.

As shown in *Figure 7.8*, appreciably smaller stresses in the porous thick film are observed, in comparison to the relatively large stress levels observed in sputtered and PLD films. The stress levels observed of these LSF64 thick films dictates that they are well within the elastic regime (i.e. much below the 100 MPa yield stress reported for LSF64 [209]) upon changes temperature and pO_2 applied in this work. This may explain the reproducible surface exchange coefficients measured across multiple thermal cycles for porous thick films, while the sputtered and PLD thin films show degradation/hysteresis behaviors though multiple thermal cycles.

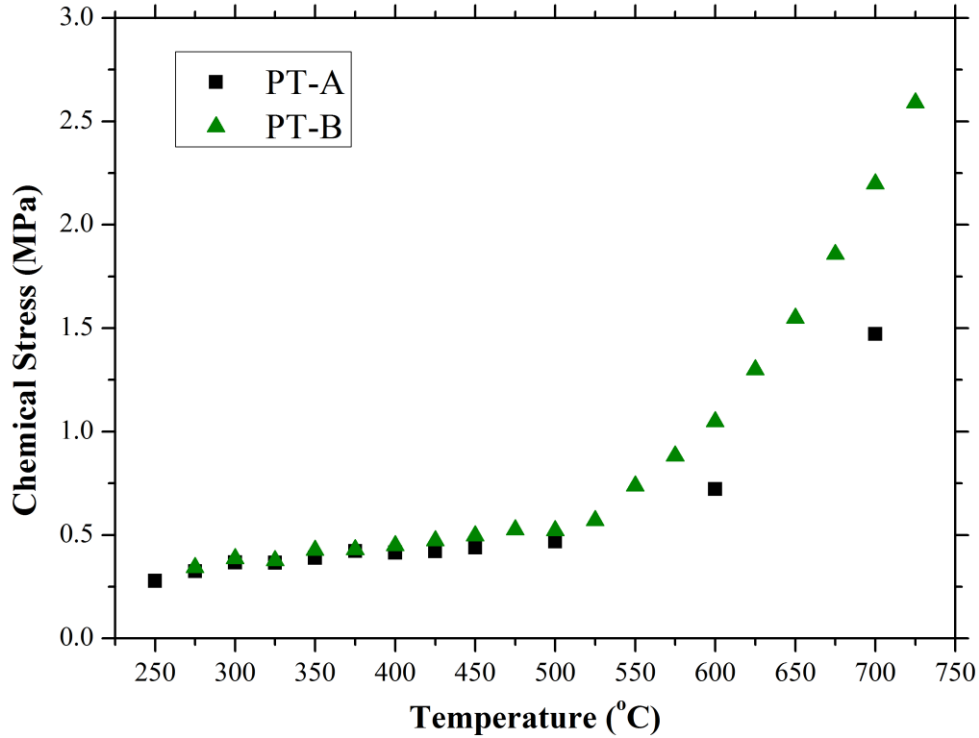


Figure 7.9 Chemical stress of spray deposited porous thick films LSF64 between $pO_2=0.21$ and $pO_2=0.021$ as a function of temperature.

The porous thick film chemical stresses shown in *Figure 7.9* are calculated from the different stress levels at $pO_2=0.21$ and $pO_2=0.021$ for each temperature, and show significant increase starting at 525°C , indicating significant increase of the oxygen nonstoichiometry above 525°C . At temperatures below 525°C , the chemical stress shows a slight decrease with decreasing temperature, but still remains small and non-zero at the lowest measurement temperature of 250°C .

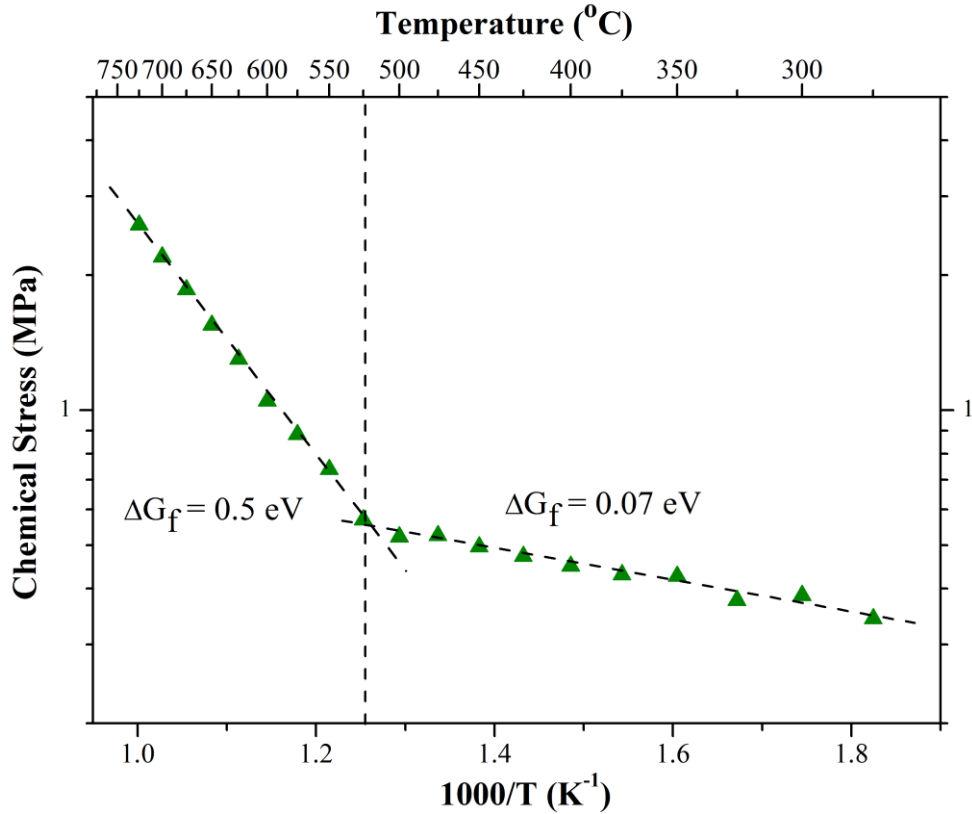


Figure 7.10 Replot of the *Figure 7.9* data on an Arrhenius scale, illustrating two regimes with different activation energies. The dashed lines are linear fits to the data.

The chemical stress Arrhenius plot in *Figure 7.10* displays a pronounced kink at 525°C . Curiously, this chemical expansion kink happens at the same temperature as the onset of chemical expansion in the large grained bulk samples of *Figure 4.2*. This suggests that LSF64 exhibits a distinct lattice-dominated chemical stress response above 525°C and a distinct grain-boundary-dominated chemical stress response below 525°C . Although more data is needed, a 525°C chemical stress kink is consistent with the sputtered LSF64 chemical stress measurements of *Figure 5.14* and the PLD LSF64 chemical stress measurements of *Figure 6.9* and *Figure 6.17*.

Given the definition of chemically induced strain in Equation (4) as well as Hooke's Law, the change in film stress is linearly proportional to the change in oxygen nonstoichiometry:

$$\Delta \lambda_f = M_f \alpha_c \Delta \delta \quad (50)$$

The application of Equation (50) and the assumption of temperature-independent M_f and α_c values allows the activation energies for oxygen vacancy formation (ΔG_f) to be extracted from the chemical stress activation energies shown in Figure 7.10. The assumption of temperature-independent M_f values is a good one, since LSF64 M_f values only change gradually by ~15% between 275 and 700°C [172] and can therefore not account for the exponential changes shown in Figure 7.10. The assumption of temperature-independent α_c values is a good assumption above 500°C, as indicated by large grained chemical expansion and nonstoichiometry data extracted from Kuhn *et al.* [200]. The assumption of temperature-independent α_c values below 500°C is more suspect, since no α_c data at these temperatures exist in the literature (i.e. no chemical expansion and nonstoichiometry experiments have been performed on small grain sized LSF64 samples). However, assuming that α_c remains constant from 275-500°C (i.e. assuming that only δ differences produce chemical stress differences, as has been assumed in studies on ceria [170] and anatase [227]) results in a grain boundary $\Delta G_f = 0.07$ eV and a lattice $\Delta G_f = 0.5$ eV. These ΔG_f values show it is much easier to form oxygen vacancies at the LSF64 grain boundaries than inside the LSF64 lattice.

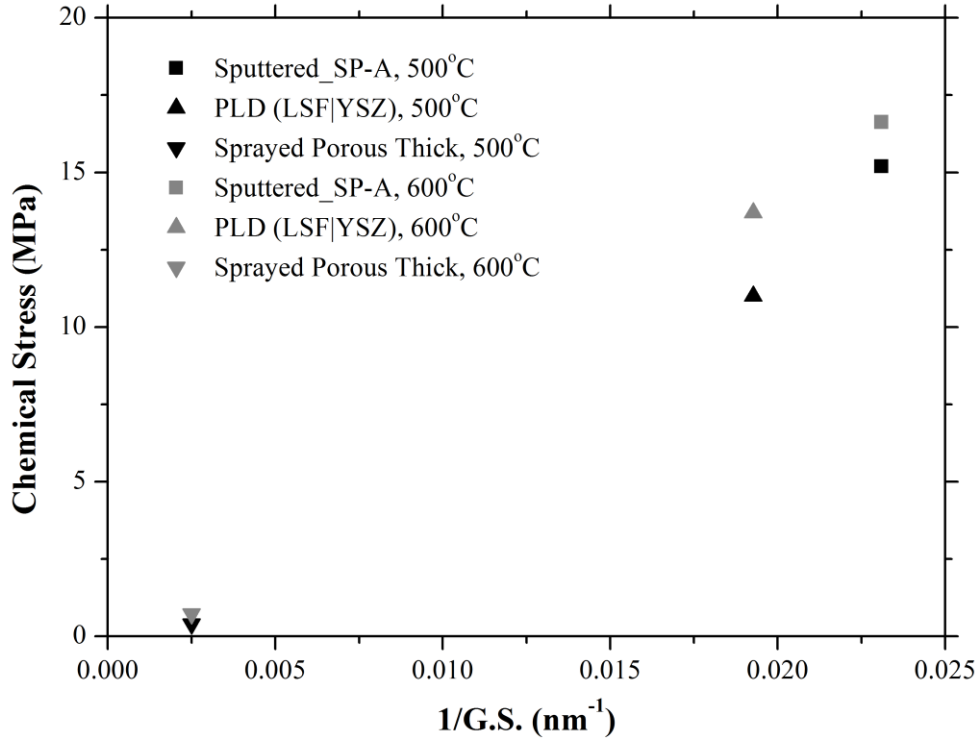


Figure 7.11 Summary of the chemical stress found in sputtered thin film SP-A, PLD thin film LSF|YSZ and the porous thick film PT-A measured at 500°C and 600°C as a function of inverse grain size (G.S.)

Figure 7.11 shows the correlation between film grain size and measured chemical stress at 500°C and 600°C for 3 different samples prepared by all three techniques in this work. Samples SP-B and SP-C, which were fabricated simultaneously with SP-A, were assumed to have the same grain size and chemical stresses as SP-A. As seen in the figures showing the temperature dependence of chemical stress throughout this dissertation, 525°C is the common temperature below which chemical stress starts to level off, but maintains a non-zero level. Further, this low temperature chemical stress increases as the grain size of the film decreases. This phenomenon is consistent with large compositional stress contribution from the grain boundaries in the nano-crystalline ceria films reported by Sheldon *et al.* [207]. At higher temperatures, chemical stress is largely induced by changes of oxygen vacancy concentration in

bulk grains. As the temperature is reduced, grain boundary induced chemical stress starts to take over the contribution from the bulk, and eventually dominates the entire chemical stress at low temperature. As the grain size dictates the ratio between grain boundary and grains, samples with smaller grain sizes are capable of causing more chemical stress at low temperature.

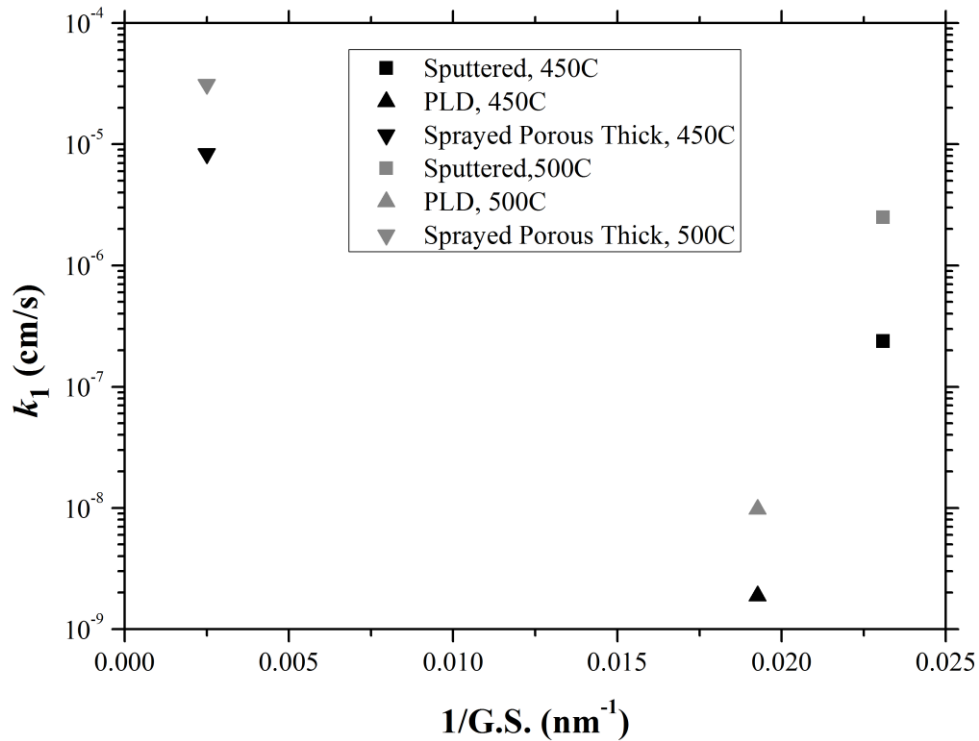


Figure 7.12 Summary of the k_1 values found in sputtered thin film SP-A, PLD thin film LSF/YSZ and the porous thick film PT-A measured at 450°C and 500°C as a function of inverse grain size (G.S.).

Figure 7.12 summarizes the surface exchange coefficients of films fabricated by all three techniques as a function of their respective inverse grain size. Although the measured k_1 values span up to 4 orders of magnitude among these films, no apparent dependence on grain size is observed, suggesting that factors other than grain size (such as differences in surface orientation, surface chemistry, etc.) control the oxygen surface exchange coefficients of the samples tested here. Additional experiments to understand this behavior are needed.

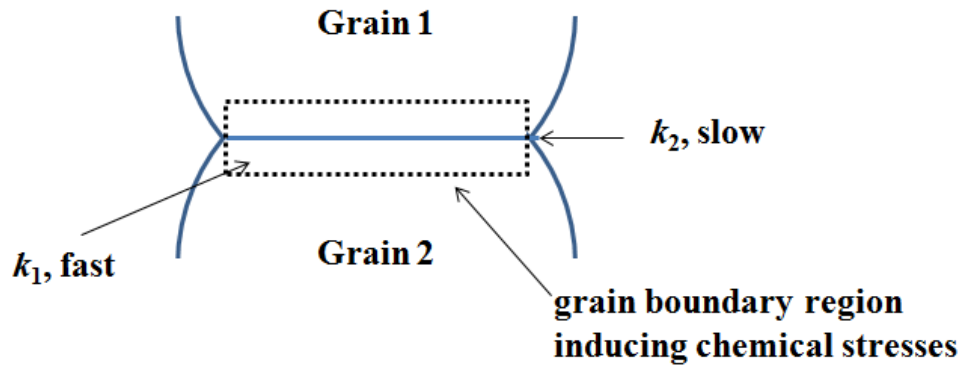


Figure 7.13 Possible surface exchange pathways. The dotted box represents the grain boundary region that induces the sub-525°C chemical stresses observed in this work.

Interestingly, although the oxygen nonstoichiometry in bulk grains becomes minimal at below 525°C, the lattice oxygen surface exchange coefficient (k_1) is still measurable in all the films tested here. This can be understood by considering that even though the lattice no longer changes its oxygen vacancy concentration below 525°C, the faster k_1 across the lattice surface, and the large surface area fraction of the lattice surface compared to the grain boundaries (at least for large grained samples) provides the dominant path for oxygen surface exchange, even as the grain boundaries alone alter their oxygen vacancy concentration at low temperature. Since the grain size is much smaller than the characteristic thickness, bulk diffusion through the lattice to the grain boundary is not rate-limiting. Interestingly, in the smallest grain size samples tested here, two exchange coefficients were observed. In these small grain sized samples, the large areal fraction of both the grain boundaries and the bulk may be the reason two oxygen incorporation processes, corresponding to oxygen incorporation at the exposed grain surfaces and the exposed grain boundaries, are observed.

7.4 Conclusions

The curvature relaxation technique was used to measure the oxygen chemical surface exchange coefficients and stresses of porous thick film $\text{La}_{0.6}\text{Sr}_{0.4}\text{FeO}_{3-\delta}$. For the first time, chemical expansion and measurable k values were obtained as low as 275°C , and are consistent with bulk LSF64 extrapolations below 400°C . The activation energy of the porous thick film is comparable to that of bulk and sputtered thin film LSF64 samples reported in the literature and in this work, but is very different than PLD thin films. Reproducible k values were obtained across multiple thermal segments, which were attributed to the noticeably small stress levels in these porous thick films. Similar to sputtered and PLD thin films, non-zero chemical stress were observed throughout the temperature range, and displayed a temperature-induced transition from grain boundary dominated chemical expansion to lattice dominated chemical expansion. This is the first time such a chemical stress transition has been observed. The low temperature chemical stresses measured in various films in this work were found to increase with decreasing grain size, suggesting that grain boundaries have enhanced oxygen vacancy concentration gradient. The grain size dependence of chemical stress observed in κR -measured films suggests that large grained SOFC electrodes may help the mechanical redox stability of SOFC materials.

8. Dissertation Summary

The aim of this dissertation was to demonstrate that a novel curvature relaxation technique could be utilized to 1) measure the *in situ* stress and oxygen surface exchange of MIEC films, and 2) provide insights on the factors such as processing techniques, microstructure, grain size, sample history and/or stress that presumably affect the surface exchange behavior. Below is a list of the conclusions from this dissertation:

- (1) The curvature relaxation technique developed in this work provides reliable, simultaneous, *in situ* measurement of the oxygen surface exchange coefficient and stress states of mechano-chemically active films.
- (2) Thermo-chemical expansion of bulk LSF64 samples were measured using dilatometry under various oxygen partial pressures ranging from air to N₂ for the first time. The chemical expansion onset temperature decreases with decreasing pO₂, and chemical expansion in bulk LSF64 only becomes active above 525°C in air. The bulk LSF64 25-1000°C thermal expansion coefficient is 12.4 ppm/K, while the 525-1000°C chemical expansion coefficient in air (pO₂=0.21) and 10% N₂-diluted air (pO₂=0.021) are 0.0101 and 0.00867, respectively.
- (3) The surface exchange coefficients of LSF64 vary among films prepared by different techniques. Thin films prepared by sputter deposition and porous thick films prepared by colloidal spray deposition have similar oxygen surface exchange coefficient magnitudes and activation energies. Further, these *k*'s are similar to those expected from low temperature extrapolations of bulk LSF64 reported in literature. In contrast, the PLD LSF64 thin films measured here have *k*'s that are much less than the bulk, sputtered, or

spray deposited films. Thin films prepared here by PLD have similar magnitude of surface exchange coefficients compared to PLD LSF64 films reported in literature. This behavior suggests that the 5-order of magnitude discrepancy reported in the literature is not related to artifacts such as the presence of electrodes or testing geometries, but rather due to other effects such as microstructure or surface chemistry.

- (4) The thickness-average film stress of sputtered and PLD thin films generally agree with the stress predictions of thermal expansion mismatch between LSF64 and YSZ, and can exceed 200 MPa below 400°C. However, the porous thick films tested here exhibited stress levels below 10 MPa throughout the 250°C to 725°C measurement range.
- (5) Degradation of surface exchange coefficients across multiple thermal cycles was observed in both sputtered and PLD thin films, while reproducible k measurements were obtained for the porous thick films. This degradation behavior could be caused by events such as ferroelastic domain switching, dislocation formation and/or cation segregation under stresses greater than ~200 MPa.
- (6) The observed correlation between the low temperature chemical stress and the film grain size suggests that enhanced grain boundary effects are responsible for the larger low temperature (i.e. <525°C) chemical stress observed in films with smaller grains.
- (7) While lattice dominated chemical expansion was observed above 525°C in all LSF64 films and large grained bulk samples, mechano-chemical coupling in LSF64 films was measured below 525°C (and as low as 250°C) for the first time using the κ R technique. This sub-525°C response is attributed to grain boundary dominated chemical expansion.

The transition between these two distinct regimes has been observed for the first time, and the associated lattice and grain boundary oxygen vacancy formation energies have been measured to be 0.5 eV and 0.07 eV, respectively.

APPENDIX

APPENDIX

Derivation of Surface Exchange Coefficient Fitting Equations used in Relaxation Experiments

In this appendix, the oxygen transport across the cathode membrane is modeled as a surface evaporation/uptaking process of moisture of a solid-state planar sheet, as seen in Crank [128].

Consider a planar sheet with a thickness of l and in-plane dimensions much larger than l . The sheet is initially equilibrated with the atmosphere in terms of the oxygen chemical potential, and has an initial oxygen concentration, C_0 . When a new oxygen atmosphere surrounding the sheet is introduced stepwise, the oxygen concentration of sheet undergoes a relaxation and eventually reaches a new equilibrium, C_∞ . The mass transport in/out of the sheet corresponds to a nonsteady state diffusion process, which can be described by the Fick's second law assuming constant diffusion coefficient, D_{chem} :

$$\frac{\partial C(x,t)}{\partial t} = D_{chem} \frac{\partial^2 C(x,t)}{\partial x^2} \quad (51)$$

$C(x,t)$ is the instantaneous oxygen concentration at position x in the sheet, where the origin is defined at the central plane. The initial condition is given as:

$$C(x,0) = C_0 \quad (52)$$

The first boundary condition concerns the uniform oxygen concentration in the bulk of the sheet:

$$\left. \frac{\partial C(x,t)}{\partial t} \right|_{x=0} = 0 \quad (53)$$

The second boundary condition concerns the outer surface of the sheet, where first order kinetics of the surface reaction is assumed:

$$-D_{chem} \left. \frac{\partial C(x,t)}{\partial x} \right|_{x=\pm l/2} = k_{chem} (C(x,t) - C_{\infty}) \quad (54)$$

The solution to the diffusion equation can then be written as [128]:

$$\frac{M_t}{M_{\infty}} = 1 - \sum_{n=1}^{\infty} \frac{2L^2 \exp(-4\beta_n^2 D_{chem} t / l^2)}{\beta_n^2 (\beta_n^2 + L^2 + L)} \quad (55)$$

where $\frac{M_t}{M_{\infty}}$ denotes the normalized amount of oxygen ions diffused at time t , β_n is a root of the

following equation

$$\beta_n \tan \beta_n = L \quad (56)$$

where L is a unitless variable defined by

$$L = \frac{lk_{chem}}{2D_{chem}} = \frac{l}{2L_c} \quad (57)$$

When $l \gg L_c$, i.e. the diffusion distance is large such that the bulk diffusion is much slower than the surface reaction, Equation (A.5) reduces to:

$$\frac{M_t}{M_{\infty}} = 1 - \sum_{n=1}^{\infty} \frac{8}{(2n+1)^2 \pi^2} \exp \left[-\frac{(2n+1)^2 \pi^2 D_{chem} t}{l^2} \right] \quad (58)$$

When $l \ll L_c$, i.e. the diffusion distance is small such that the bulk diffusion is much faster than the surface reaction, Equation (55) reduces to:

$$\frac{M_t}{M_\infty} = 1 - \exp\left(-\frac{tk_{chem}}{l}\right) \quad (59)$$

Since the number of sites occupied by oxygen ions is proportional to the oxygen concentration [228], a normalized quantity, $g(t)$, can be defined as:

$$g(t) = \frac{C(t) - C_0}{C_\infty - C_0} = \frac{M_t}{M_\infty} = 1 - \sum_{n=1}^{\infty} \frac{2L^2 \exp(-4\beta_n^2 D_{chem} t / l^2)}{\beta_n^2 (\beta_n^2 + L^2 + L)} \quad (60)$$

As the oxygen concentration is linearly correlated to a variety of measurable quantities, such as electrical conductivity, weight, strain and optical properties, the solutions above are widely used in relaxation techniques measuring oxygen transport.

REFERENCES

REFERENCES

1. *International Energy Outlook*. 2013, U.S. Energy Information Administration.
2. *Annual Energy Review*. 2012, U.S. Energy Information Administration.
3. Steele, B.C.H. and A. Heinzl, *Materials for Fuel-Cell Technologies*. Nature, 2001. **414**(6861): p. 345-352.
4. *The Fuel Cell Industry Review*. 2013, FuelCell Today.
5. *Hexis Inc. Galileo 1000 N Brochure*. Available from: http://www.hexis.com/sites/default/files/media/publikationen/130524_hexis_broschuere_galileo_e_web.pdf.
6. Hosoi, K. and M. Nakabaru, *Status of National Project for SOFC Development in Japan*. ECS Transactions, 2009. **25**(2): p. 11-20.
7. Bauen, A. and D. Hart, *Assessment of the Environmental Benefits of Transport and Stationary Fuel Cells*. Journal of Power Sources, 2000. **86**(1-2): p. 482-494.
8. Schlapbach, L. and A. Zuttel, *Hydrogen-storage Materials for Mobile Applications*. Nature, 2001. **414**(6861): p. 353-358.
9. Wachsman, E.D. and K.T. Lee, *Lowering the Temperature of Solid Oxide Fuel Cells*. Science, 2011. **334**(6058): p. 935-939.
10. Haile, S.M., *Fuel Cell Materials and Components*. Acta Materialia, 2003. **51**: p. 5981-6000.
11. O'Hayre, R.P., *Fuel Cell Fundamentals*. 2006: John Wiley & Sons.
12. Carrette, L., K.A. Friedrich, and U. Stimming, *Fuel Cells: Principles, Types, Fuels, and Applications*. Chemphyschem, 2000. **1**(4): p. 162-193.
13. *Molten Carbonate Fuel Cell Technology*. 2011, U.S. Department of Energy.
14. Kroger, F.A. and H.J. Vink, *Relations between the Concentrations of Imperfections in Crystalline Solids*. Solid State Physics-Advances in Research and Applications, 1956. **3**: p. 307-435.
15. Adler, S.B., *Factors Governing Oxygen Reduction in Solid Oxide Fuel Cell Cathodes*. Chemical Reviews, 2004. **104**(10): p. 4791-4843.

16. Steele, B.C.H., K.M. Hori, and S. Uchino, *Kinetic Parameters Influencing the Performance of IT-SOFC Composite Electrodes*. Solid State Ionics, 2000. **135**(1-4): p. 445-450.
17. Godickemeier, M., K. Sasaki, L.J. Gauckler, and I. Riess, *Perovskite Cathodes for Solid Oxide Fuel Cells Based on Ceria Electrolytes*. Solid State Ionics, 1996. **86-88**: p. 691-701.
18. Maguire, E., B. Gharbage, F.M.B. Marques, and J.A. Labrincha, *Cathode Materials for Intermediate Temperature SOFCs*. Solid State Ionics, 2000. **127**: p. 329-335.
19. Colomer, M.T., B.C.H. Steele, and J.A. Kilner, *Structural and Electrochemical Properties of the Sr_{0.8}Ce_{0.1}Fe_{0.7}Co_{0.3}O_{3-delta} Perovskite as Cathode Material for ITSOFCs*. Solid State Ionics, 2002. **147**: p. 41-48.
20. Shao, Z. and S.M. Haile, *A High-Performance Cathode for the Next Generation of Solid Oxide Fuel Cells*. Nature, 2004. **431**: p. 170-173.
21. Skinner, S.J., *Recent Advances in Perovskite-type Materials for Solid Oxide Fuel Cell Cathodes*. International Journal of Inorganic Materials, 2001. **3**(2): p. 113-121.
22. Xia, C., W. Rauch, F. Chen, and M. Liu, *Sm_{0.5}Sr_{0.5}CoO₃ Cathodes for Low-temperature SOFCs*. Solid State Ionics, 2002. **149**(1-2): p. 11-19.
23. Shao, Z.P. and S.M. Haile, *A High-performance Cathode for the Next Generation of Solid-Oxide Fuel Cells*. Nature, 2004. **431**(7005): p. 170-173.
24. Nicholas, J.D., L. Wang, A.V. Call, and S.A. Barnett, *Use of the Simple Infiltrated Microstructure Polarization Loss Estimation (SIMPLE) Model to Describe the Performance of Nano-composite Solid Oxide Fuel Cell Cathodes*. Physical Chemistry Chemical Physics, 2012.
25. Baumann, F.S., J. Fleig, G. Cristiani, B. Stuhlhofer, H.-U. Habermeier, and J. Maier, *Quantitative Comparison of Mixed Conducting SOFC Cathode Materials by Means of Thin Film Model Electrodes*. Journal of the Electrochemical Society, 2007. **154**(9): p. B931-B941.
26. Baumann, F.S., J. Fleig, H.U. Habermeier, and J. Maier, *Impedance Spectroscopic Study on Well-defined (La,Sr)(Co,Fe)O_{3-delta} Model Electrodes*. Solid State Ionics, 2006. **177**(11-12): p. 1071-1081.
27. Atkinson, A., S.A. Barnett, R.J. Gorte, J.T.S. Irvine, A.J. McEvoy, M.B. Mogensen, S. Singhal, and J. Vohs, *Advanced Anodes for High Temperature Fuel Cells*. Nature Materials, 2004. **3**: p. 17-27.
28. Oishi, M., K. Yashiro, K. Sato, J. Mizusaki, and T. Kawada, *Oxygen Nonstoichiometry and Defect Structure Analysis of B-site Mixed Perovskite-type Oxide (La, Sr)(Cr, M)O₃₋*

- delta* ($M = \text{Ti, Mn and Fe}$). Journal of Solid State Chemistry, 2008. **181**(11): p. 3177-3184.
29. Tao, S.W., J.T.S. Irvine, and S.M. Plint, *Methane Oxidation at Redox Stable Fuel Cell Electrode $\text{La}_{0.75}\text{Sr}_{0.25}\text{Cr}_{0.5}\text{Mn}_{0.5}\text{O}_3\text{-delta}$* . Journal of Physical Chemistry B, 2006. **110**(43): p. 21771-21776.
 30. Boukamp, B.A., *The Amazing Perovskite Anode*. Nature Materials, 2003. **2**(5): p. 294-296.
 31. Wan, J., J.H. Zhu, and J.B. Goodenough, *$\text{La}_{0.75}\text{Sr}_{0.25}\text{Cr}_{0.5}\text{Mn}_{0.5}\text{O}_3\text{-delta} + \text{Cu}$ Composite Anode Running on H_2 and CH_4 Fuels*. Solid State Ionics, 2006. **177**(13-14): p. 1211-1217.
 32. Tao, S. and J.T.S. Irvine, *A Redox-Stable, Efficient Anode For Solid-Oxide Fuel Cells*. Nature Materials, 2003. **2**: p. 320-323.
 33. Doshi, R., V.L. Richards, J.D. Carter, X. Wang, and M. Krumpelt, *Development of Solid Oxide Fuel Cells That Operate at 500C*. J. Electrochem. Soc., 1999. **146**: p. 1273-1278.
 34. Huijsmans, J.P.P., F.P.F. van Berkel, and G.M. Christie, *Intermediate Temperature SOFC - A Promise for the 21st Century*. Journal of Power Sources, 1998. **71**(1-2): p. 107-110.
 35. Ralph, J.M., A.C. Schoeler, and M. Krumpelt, *Materials for Lower Temperature Solid Oxide Fuel Cells*. Journal of Materials Science, 2001. **36**(5): p. 1161-1172.
 36. Huang, K.Q., R.S. Tichy, and J.B. Goodenough, *Superior Perovskite Oxide-ion Conductor; Strontium- and Magnesium-doped LaGaO_3 : I, Phase Relationships and Electrical Properties*. Journal of the American Ceramic Society, 1998. **81**(10): p. 2565-2575.
 37. Huang, K.Q., R.S. Tichy, and J.B. Goodenough, *Superior Perovskite Oxide-ion Conductor; Strontium- and Magnesium-doped LaGaO_3 : II, AC Impedance Spectroscopy*. Journal of the American Ceramic Society, 1998. **81**(10): p. 2576-2580.
 38. Huang, K.Q., R. Tichy, and J.B. Goodenough, *Superior Perovskite Oxide-ion Conductor; Strontium- and Magnesium-doped LaGaO_3 : III, Performance Tests of Single Ceramic Fuel Cells*. Journal of the American Ceramic Society, 1998. **81**(10): p. 2581-2585.
 39. Baur, E. and H. Preis, *On fuel Chains with Fixed Cables*. Zeitschrift Fur Elektrochemie Und Angewandte Physikalische Chemie, 1937. **43**: p. 727-732.
 40. Oishi, N., A. Atkinson, N.P. Brandon, J.A. Kilner, and B.C.H. Steele, *Fabrication of an Anode-Supported Gadolinium-Doped Ceria Solid Oxide Fuel Cell and Its Operation at 550 °C*. Journal of the American Ceramic Society, 2005. **88**(6): p. 1394-1396.

41. Suzuki, T., Z. Hasan, Y. Funahashi, T. Yamaguchi, Y. Fujishiro, and M. Awano, *Impact of Anode Microstructure on Solid Oxide Fuel Cells*. Science, 2009. **325**(5942): p. 852-855.
42. Tu, H. and U. Stimming, *Advances, Aging Mechanisms and Lifetime in Solid-Oxide Fuel Cells*. Journal of Power Sources, 2004. **127**(1-2): p. 284-293.
43. Blum, L., U. Packbier, I.C. Vinke, and L.G.J. de Haart, *Long-Term Testing of SOFC Stacks at Forschungszentrum Jilich*. Fuel Cells, 2013. **13**(4): p. 646-653.
44. Kleitz, M. and F. Petitbon, *Optimized SOFC Electrode Microstructure*. Solid State Ionics, 1996. **92**(1-2): p. 65-74.
45. Gourba, E., A. Ringuede, M. Cassir, A. Billard, J. Paiviasaari, J. Niinisto, M. Putkonen, and L. Niinisto, *Characterisation of thin films of ceria-based electrolytes for Intermediate Temperature - Solid oxide fuel cells (IT-SOFC)*. Ionics, 2003. **9**(1-2): p. 15-20.
46. Huang, H., M. Nakamura, P.C. Su, R. Fasching, Y. Saito, and F.B. Prinz, *High-performance ultrathin solid oxide fuel cells for low-temperature operation*. Journal of the Electrochemical Society, 2007. **154**(1): p. B20-B24.
47. tenElshof, J.E., M.H.R. Lankhorst, and H.J.M. Bouwmeester, *Oxygen Exchange and Diffusion Coefficients of Strontium-doped Lanthanum Ferrites by Electrical Conductivity Relaxation*. Journal of the Electrochemical Society, 1997. **144**(3): p. 1060-1067.
48. Sogaard, M., A. Bieberle-Hutter, P.V. Hendriksen, M. Mogensen, and H.L. Tuller, *Oxygen Incorporation in Porous Thin Films of Strontium Doped Lanthanum Ferrite*. Journal of Electroceramics, 2011. **27**(3-4): p. 134-142.
49. Sogaard, M., P.V. Hendriksen, and M. Mogensen, *Oxygen Nonstoichiometry and Transport Properties of Strontium Substituted Lanthanum Ferrite*. Journal of Solid State Chemistry, 2007. **180**(4): p. 1489-1503.
50. Mosleh, M., M. Sogaard, and P.V. Hendriksen, *Kinetics and Mechanisms of Oxygen Surface Exchange on La_{0.6}Sr_{0.4}FeO_{3-delta} Thin Films*. Journal of the Electrochemical Society, 2009. **156**(4): p. B441-B457.
51. Yildiz, B., "Stretching" the Energy Landscape of Oxides—Effects on Electrocatalysis and Diffusion. Mrs Bulletin, 2014. **39**(02): p. 147-156.
52. Kushima, A., S. Yip, and B. Yildiz, *Competing Strain Effects in Reactivity of LaCoO₃ with Oxygen*. Physical Review B, 2010. **82**(11).
53. Ivers-Tiffée, E., A. Weber, and D. Herbristrit, *Materials and Technologies for SOFC-components*. Journal of the European Ceramic Society, 2001. **21**(10-11): p. 1805-1811.

54. Adler, S.B., J.A. Lane, and B.C.H. Steele, *Electrode Kinetics of Porous Mixed Conducting Oxygen Electrodes*. Journal of the Electrochemical Society, 1996. **143**(11): p. 3554-3564.
55. Shah, M., J.D. Nicholas, and S.A. Barnett, *Prediction of infiltrated solid oxide fuel cell cathode polarization resistance*. Electrochemistry Communications, 2009. **11**(1): p. 2-5.
56. Tsuchiya, M., N.A. Bojarczuk, S. Guha, and S. Ramanathan, *Microstructural Effects on Electrical Conductivity Relaxation in Nanoscale Ceria Thin Films*. Journal of Chemical Physics, 2009. **130**(17).
57. Rupp, J.L.M. and L.J. Gauckler, *Microstructures and Electrical Conductivity of Nanocrystalline Ceria-based Thin Films*. Solid State Ionics, 2006. **177**(26-32): p. 2513-2518.
58. Chiang, Y.M., E.B. Lavik, I. Kosacki, H.L. Tuller, and J.Y. Ying, *Defect and Transport Properties of Nanocrystalline CeO_{2-x}*. Applied Physics Letters, 1996. **69**(2): p. 185-187.
59. Karthikeyan, A. and S. Ramanathan, *Oxygen Surface Exchange Studies in Thin Film Gd-doped Ceria*. Applied Physics Letters, 2008. **92**(24).
60. Mutoro, E., E.J. Crumlin, M.D. Biegalski, H.M. Christen, and Y. Shao-Horn, *Enhanced oxygen reduction activity on surface-decorated perovskite thin films for solid oxide fuel cells*. Energy & Environmental Science, 2011. **4**(9): p. 3689-3696.
61. Lane, J.A., S.J. Benson, D. Waller, and J.A. Kilner, *Oxygen Transport in La_{0.6}Sr_{0.4}Co_{0.2}Fe_{0.8}O_{3-δ}*. Solid State Ionics, 1999. **121**(1-4): p. 201-208.
62. Zomorrodian, A., H. Salamati, Z.G. Lu, X. Chen, N.J. Wu, and A. Ignatiev, *Electrical Conductivity of Epitaxial La_{0.6}Sr_{0.4}Co_{0.2}Fe_{0.8}O_{3-δ} Thin Films Grown by Pulsed Laser Deposition*. International Journal of Hydrogen Energy, 2010. **35**(22): p. 12443-12448.
63. Armstrong, E.N., K.L. Duncan, D.J. Oh, J.F. Weaver, and E.D. Wachsman, *Determination of Surface Exchange Coefficients of LSM, LSCF, YSZ, GDC Constituent Materials in Composite SOFC Cathodes*. Journal of the Electrochemical Society, 2011. **158**(5): p. B492-B499.
64. Simrick, N.J., A. Bieberle-Hutter, T.M. Ryll, J.A. Kilner, A. Atkinson, and J.L.M. Rupp, *An Investigation of the Oxygen Reduction Reaction Mechanism of La_{0.6}Sr_{0.4}Co_{0.2}Fe_{0.8}O₃ Using Patterned Thin Films*. Solid State Ionics, 2012. **206**: p. 7-16.
65. Li, Y.H., K. Gerdes, T. Horita, and X.B. Liu, *Surface Exchange and Bulk Diffusivity of LSCF as SOFC Cathode: Electrical Conductivity Relaxation and Isotope Exchange Characterizations*. Journal of the Electrochemical Society, 2013. **160**(4): p. F343-F350.

66. Dalslet, B.T., M. Sogaard, and P.V. Hendriksen, *Determination of Oxygen Transport Properties from Flux and Driving Force Measurements*. Journal of the Electrochemical Society, 2007. **154**(12): p. B1276-B1287.
67. Trovarelli, A., *Catalytic Properties of Ceria and CeO₂-containing Materials*. Catalysis Reviews: Science and Engineering, 1996. **38**: p. 439-509.
68. Stefanik, T.S. and H.L. Tuller, *Ceria-Based Gas Sensors*. Journal of the European Ceramic Society, 2001. **21**(10–11): p. 1967-1970.
69. Chueh, W.C., C. Falter, M. Abbott, D. Scipio, P. Furler, S.M. Haile, and A. Steinfeld, *High-Flux Solar-Driven Thermochemical Dissociation of CO₂ and H₂O Using Nonstoichiometric Ceria*. Science, 2010. **330**(6012): p. 1797-1801.
70. Primo, A., T. Marino, A. Corma, R. Molinari, and H. Garcia, *Efficient Visible-Light Photocatalytic Water Splitting by Minute Amounts of Gold Supported on Nanoparticulate CeO₂ Obtained by a Biopolymer Templating Method*. Journal of the American Chemical Society, 2011. **133**(18): p. 6930-6933.
71. Bouwmeester, H.J.M. and A.J. Burggraaf, *Dense Ceramic Membranes for Oxygen Separation*, in *The CRC Handbook of Solid State Electrochemistry*, P.J. Gellings and H.J.M. Bouwmeester, Editors. 1997, CRC Press: New York. p. 481-554.
72. Woodford, W.H., W.C. Carter, and Y.M. Chiang, *Design Criteria for Electrochemical Shock Resistant Battery Electrodes*. Energy & Environmental Science, 2012. **5**(7): p. 8014-8024.
73. Atkinson, A., *Chemically-Induced Stresses in Gadolinium-Doped Ceria Solid Oxide Fuel Cell Electrolytes*. Solid State Ionics, 1997. **95**: p. 249-258.
74. Pei, S., M.S. Kleefisch, T.P. Kobylinski, J. Faber, C.A. Udovich, V. Zhangmccoy, B. Dabrowski, U. Balachandran, R.L. Mieville, and R.B. Poepfel, *Failure Mechanisms of Ceramic Membrane Reactors in Partial Oxidation of Methane to Synthesis Gas*. Catalysis Letters, 1995. **30**(1-4): p. 201-212.
75. Li, Y.P., E.R. Maxey, and J.W. Richardson, *Structural Behavior of Oxygen Permeable SrFe_{0.2}Co_{0.8}O_x Ceramic Membranes with and without pO(2) Gradients*. Journal of the American Ceramic Society, 2005. **88**(5): p. 1244-1252.
76. Mizusaki, J., M. Yoshihiro, S. Yamauchi, and K. Fueki, *Nonstoichiometry and Defect Structure of the Perovskite-Type Oxides La_{1-x}Sr_xFeO_{3-δ}*. Journal of Solid State Chemistry, 1985. **58**(2): p. 257-266.
77. Kharton, V.V., A.A. Yaremchenko, M.V. Patrakeev, E.N. Naumovich, and F.M.B. Marques, *Thermal and Chemical Induced Expansion of La_{0.3}Sr_{0.7}(Fe,Ga)O_{3-δ} Ceramics*. Journal of the European Ceramic Society, 2003. **23**(9): p. 1417-1426.

78. Bishop, S.R., K.L. Duncan, and E.D. Wachsman, *Surface and Bulk Oxygen Non-stoichiometry and Bulk Chemical Expansion in Gadolinium-doped Cerium Oxide*. Acta Materialia, 2009. **57**(12): p. 3596-3605.
79. Bishop, S.R., K.L. Duncan, and E.D. Wachsman, *Defect Equilibria and Chemical Expansion in Non-stoichiometric Undoped and Gadolinium-doped Cerium Oxide*. Electrochimica Acta, 2009. **54**(5): p. 1436-1443.
80. Chiang, H.W., R.N. Blumenthal, and R.A. Fournelle, *A High-temperature Lattice-Parameter and Dilatometer Study of the Defect Structure of Nonstoichiometric Cerium Dioxide*. Solid State Ionics, 1993. **66**(1-2): p. 85-95.
81. Chen, X.Y., J.S. Yu, and S.B. Adler, *Thermal and Chemical Expansion of Sr-doped Lanthanum Cobalt Oxide ($La_{1-x}Sr_xCoO_{3-\delta}$)*. Chemistry of Materials, 2005. **17**(17): p. 4537-4546.
82. Bishop, S.R., K.L. Duncan, and E.D. Wachsman, *Thermo-Chemical Expansion in Strontium-Doped Lanthanum Cobalt Iron Oxide*. Journal of the American Ceramic Society, 2010. **93**(12): p. 4115-4121.
83. Larsen, P.H., P.V. Hendriksen, and M. Mogensen, *Dimensional Stability and Defect Chemistry of Doped Lanthanum Chromites*. Journal of Thermal Analysis, 1997. **49**(3): p. 1263-1275.
84. Miyoshi, S., J.O. Hong, K. Yashiro, A. Kaimai, Y. Nigara, K. Kawamura, T. Kawada, and J. Mizusaki, *Lattice Expansion upon Reduction of Perovskite-type $LaMnO_3$ with Oxygen-Deficit Nonstoichiometry*. Solid State Ionics, 2003. **161**(3-4): p. 209-217.
85. Adler, S.B., *Chemical Expansivity of Electrochemical Ceramics*. Journal of the American Ceramic Society, 2001. **84**(9): p. 2117-2119.
86. McIntosh, S., J.F. Vente, W.G. Haije, D.H.A. Blank, and H.J.M. Bouwmeester, *Oxygen Stoichiometry and Chemical Expansion of $Ba_{0.5}Sr_{0.5}Co_{0.8}Fe_{0.2}O_{3-\delta}$ Measured by In Situ Neutron Diffraction*. Chemistry of Materials, 2006. **18**(8): p. 2187-2193.
87. Vracar, M., A. Kuzmin, R. Merkle, J. Purans, E.A. Kotomin, J. Maier, and O. Mathon, *Jahn-Teller Distortion around $Fe(4+)$ in $SrFe_xTi_{1-x}O_{3-\delta}$ from X-ray Absorption Spectroscopy, X-ray Diffraction, and Vibrational Spectroscopy*. Physical Review B, 2007. **76**(17): p. 174107-1 to 144107-10.
88. Bishop, S.R., K.L. Duncan, and E.D. Wachsman, *Surface and Bulk Oxygen Non-stoichiometry and Bulk Chemical Expansion in Gadolinium-doped Cerium Oxide*. Acta Mater., 2009. **57**(12): p. 3596-3605.
89. Bishop, S.R., K.L. Duncan, and E.D. Wachsman, *Defect Equilibria and Chemical Expansion in Non-stoichiometric Undoped and Gadolinium-doped Cerium Oxide*. Electrochem. Acta, 2009. **54**(5): p. 1436-1443.

90. Kharton, V.V., A.A. Yaremchenko, M.V. Patrakeev, E.N. Naumovich, and F.M.B. Marques, *Thermal and Chemical Induced Expansion of $La_{0.3}Sr_{0.7}(Fe,Ga)O_{3-\delta}$ Ceramics*. J. Eur. Ceram. Soc., 2003. **23**(9): p. 1417-1426.
91. Bishop, S.R., K.L. Duncan, and E.D. Wachsman, *Thermo-Chemical Expansion in Strontium-Doped Lanthanum Cobalt Iron Oxide*. J. Am Cer. Soc., 2010. **93**(12): p. 4115-4121.
92. Adler, S.B., *Chemical Expansivity of Electrochemical Ceramics*. J. Am Cer. Soc., 2001. **84**(9): p. 2117-2119.
93. Chen, X.Y., J.S. Yu, and S.B. Adler, *Thermal and Chemical Expansion of Sr-doped Lanthanum Cobalt Oxide ($La_{1-x}Sr_xCoO_{3-\delta}$)*. Chem. Mater., 2005. **17**(17): p. 4537-4546.
94. Vracar, M., A. Kuzmin, R. Merkle, J. Purans, E.A. Kotomin, J. Maier, and O. Mathon, *Jahn-Teller Distortion around $Fe(4+)$ in $SrFe_xTi_{1-x}O_{3-\delta}$ from X-ray Absorption Spectroscopy, X-ray Diffraction, and Vibrational Spectroscopy*. Phys. Rev. B, 2007. **76**(17): p. 174107-1 - 174107-12.
95. McIntosh, S., J.F. Vente, W.G. Haije, D.H.A. Blank, and H.J.M. Bouwmeester, *Oxygen Stoichiometry and Chemical Expansion of $Ba_{0.5}Sr_{0.5}Co_{0.8}Fe_{0.2}O_{3-\delta}$ Measured by In Situ Neutron Diffraction*. Chem. Mater., 2006. **18**(8): p. 2187-2193.
96. Larsen, P.H., P.V. Hendriksen, and M. Mogensen, *Dimensional Stability and Defect Chemistry of Doped Lanthanum Chromites*. J. Therm. Anal., 1997. **49**(3): p. 1263-1275.
97. Atkinson, A. and T.M.G.M. Ramos, *Chemically-Induced Stresses in Ceramic Oxygen Ion-Conducting Membranes*. Solid State Ionics, 2000. **129**(1-4): p. 259-269.
98. Mandowara, S., *Grain Boundary Induced Compositional Stresses in Non-stoichiometric Oxide Films*, in *Division of Engineering*. 2009, Brown University: Providence, RI. p. 257.
99. Mandowara, S. and B.W. Sheldon, *Compositional Stresses in Polycrystalline Ceria Films*. Electrochem. Soc. Trans., 2008. **11**(33): p. 191-196.
100. Chroneos, A., B. Yildiz, A. Tarancon, D. Parfitt, and J.A. Kilner, *Oxygen diffusion in solid oxide fuel cell cathode and electrolyte materials: mechanistic insights from atomistic simulations*. Energy & Environmental Science, 2011. **4**(8): p. 2774-2789.
101. Azad, S., O.A. Marina, C.M. Wang, L. Saraf, V. Shutthanandan, D.E. McCready, A. El-Azab, J.E. Jaffe, M.H. Engelhard, C.H.F. Peden, and S. Thevuthasan, *Nanoscale Effects on Ion Conductance of Layer-by-layer Structures of Gadolinia Doped Ceria and Zirconia*. Appl. Phys. Lett., 2005. **86**(13): p. 131906-1 - 131906-3.
102. Rushton, M.J.D., A. Chroneos, S.J. Skinner, J.A. Kilner, and R.W. Grimes, *Effect of Strain on the Oxygen Diffusion in Yttria and Gadolinia Co-doped Ceria*. Solid State Ionics, 2012: p. In Press.

103. De Souza, R.A., A. Ramadan, and S. Horner, *Modifying the Barriers for Oxygen-vacancy Migration in Fluorite-structured CeO₂ Electrolytes through Strain: A Computer Simulation Study*. Energy & Environmental Science, 2012. **5**(1): p. 5445-5453.
104. Avila-Paredes, H.J. and S. Kim, *The Effect of Segregated Transition Metal Ions on the Grain Boundary Resistivity of Gadolinium Doped Ceria: Alteration of the Space Charge Potential*. Solid State Ionics, 2006. **177**: p. 3075-3080.
105. la O, G.J., S.J. Ahn, E. Crumlin, Y. Orikasa, M.D. Biegalski, H.M. Christen, and Y. Shao-Horn, *Catalytic Activity Enhancement for Oxygen Reduction on Epitaxial Perovskite Thin Films for Solid-Oxide Fuel Cells*. Angew. Chem.-Intl. Ed., 2010. **49**(31): p. 5344-5347.
106. Santiso, J. and M. Burriel, *Deposition and Characterisation of Epitaxial Oxide Thin Films for SOFCs*. J. Solid State Electrochem., 2011. **15**(5): p. 985-1006.
107. Sayle, T.X.T., M. Cantoni, U.M. Bhatta, S.C. Parker, S.R. Hall, G. Mobus, M. Molinari, D. Reid, S. Seal, and D.C. Sayle, *Strain and Architecture-Tuned Reactivity in Ceria Nanostructures; Enhanced Catalytic Oxidation of CO to CO₂*. Chem. Mater., 2012. **24**(10): p. 1811-1821.
108. Solis, C., W. Jung, H.L. Tuller, and J. Santiso, *Defect Structure, Charge Transport Mechanisms, and Strain Effects in Sr(4)Fe(6)O(12+delta) Epitaxial Thin Films*. Chem. Mater., 2010. **22**(4): p. 1452-1461.
109. Kushima, A. and B. Yildiz, *Oxygen Ion Diffusivity in Strained Yttria Stabilized Zirconia: Where is the Fastest Strain?* J. Mater. Chem., 2010. **20**(23): p. 4809-4819.
110. Kubicek, M., Z.H. Cai, W. Ma, B. Yildiz, H. Hutter, and J. Fleig, *Tensile Lattice Strain Accelerates Oxygen Surface Exchange and Diffusion in La_{1-x}Sr_xCoO_{3-delta} Thin Films*. Acs Nano, 2013. **7**(4): p. 3276-3286.
111. Kuru, Y., D. Marrocchelli, S.R. Bishop, D. Chen, B. Yildiz, and H.L. Tuller, *Anomalous Chemical Expansion Behavior of Pr_{0.2}Ce_{0.8}O_{2-delta} Thin Films Grown by Pulsed Laser Deposition*. Journal of the Electrochemical Society, 2012. **159**(11): p. F799-F803.
112. Bouwmeester, H.J.M., H. Kruidhof, and A.J. Burggraaf, *Importance of the Surface Exchange Kinetics as Rate-Limiting Step in Oxygen Permeation through Mixed-Conducting Oxides*. Solid State Ionics, 1994. **72**: p. 185-194.
113. Weppner, W. and R.A. Huggins, *Determination of Kinetic and Thermodynamic Parameters of Mixed-Conducting Electrodes, and Application to System Li-Sb*. Journal of the Electrochemical Society, 1977. **124**(3): p. C135-C135.
114. Leonhardt, M., R.A. De Souza, J. Claus, and J. Maier, *Surface Kinetics of Oxygen Incorporation into SrTiO₃*. Journal of the Electrochemical Society, 2002. **149**(2): p. J19-J26.

115. Smith, J.B. and T. Norby, *On the Steady-state Oxygen Permeation through La₂NiO₄+ δ Membranes*. Journal of the Electrochemical Society, 2006. **153**(2): p. A233-A238.
116. Jamnik, J. and J. Maier, *Treatment of the Impedance of Mixed Conductors - Equivalent Circuit Model and Explicit Approximate Solutions*. J. Electrochem Soc., 1999. **146**(11): p. 4183-4188.
117. De Souza, R.A. and J.A. Kilner, *Oxygen Transport in La_{1-x}Sr_xMn_{1-y}Co_yO₃+/-[δ] Perovskites: Part II. Oxygen Surface Exchange*. Solid State Ionics, 1999. **126**(1-2): p. 153-161.
118. tenElshof, J.E., M.H.R. Lankhorst, and H.J.M. Bouwmeester, *Chemical Diffusion and Oxygen Exchange of La_{0.6}Sr_{0.4}Co_{0.6}Fe_{0.4}O_{3- δ}* Solid State Ionics, 1997. **99**(1-2): p. 15-22.
119. Armstrong, E.N., K.L. Duncan, D.J. Oh, J.F. Weaver, and E.D. Wachsman, *Determination of Surface Exchange Coefficients of LSM, LSCF, YSZ, GDC Constituent Materials in Composite SOFC Cathodes*. J. Electrochem Soc., 2011. **158**(5): p. B492-B499.
120. Diethelm, S. and J. Van herle, *Electrochemical Characterisation of Oxygen Nonstoichiometry and Transport in Mixed Conducting Oxides - Application to La_{0.4}Ba_{0.6}Fe_{0.8}Co_{0.2}O_{3- δ}* . Solid State Ionics, 2004. **174**(1-4): p. 127-134.
121. Katsuki, M., S. Wang, K. Yasumoto, and M. Dokiya, *The Oxygen Transport in Gd-doped Ceria*. Solid State Ionics, 2002. **154-155**(0): p. 589-595.
122. Noll, F., W. Munch, I. Denk, and J. Maier, *SrTiO₃ as a Prototype of a Mixed Conductor. Conductivities, Oxygen Diffusion and Boundary Effects*. Solid State Ionics, 1996. **86-8**: p. 711-717.
123. Moreno, R., P. Garcia, J. Zapata, J. Roqueta, J. Chaigneau, and J. Santiso, *Chemical Strain Kinetics Induced by Oxygen Surface Exchange in Epitaxial Films Explored by Time-Resolved X-ray Diffraction*. Chemistry of Materials, 2013. **25**(18): p. 3640-3647.
124. Gellings, P.J. and H.J.M. Bouwmeester, *The CRC Handbook of Solid State Electrochemistry*. 1997, Boca Raton, FL: CRC Press, Inc.
125. Jamnik, J. and J. Maier, *Treatment of the Impedance of Mixed Conductors - Equivalent Circuit Model and Explicit Approximate Solutions*. Journal of the Electrochemical Society, 1999. **146**(11): p. 4183-4188.
126. Steele, B.C.H., *Interfacial Reactions Associated with Ceramic Ion-Transport Membranes*. Solid State Ionics, 1995. **75**: p. 157-165.
127. Nicholas, J.D. and S.A. Barnett, *Finite-Element Modeling of Idealized Infiltrated Composite Solid Oxide Fuel Cell Cathodes*. Journal of the Electrochemical Society, 2009. **156**(4): p. B458-B464.

128. Crank, J., *The Mathematics of Diffusion*. 1975, Oxford, UK: Oxford University Press.
129. Yasuda, I. and T. Hikita, *Precise Determination of The Chemical Diffusion Coefficient of Calcium-Doped Lanthanum Chromites by Means of Electrical Conductivity Relaxation*. Journal of the Electrochemical Society, 1994. **141**(5): p. 1268-1273.
130. Kim, G., S. Wang, A.J. Jacobson, and C.L. Chen, *Measurement of Oxygen Transport Kinetics in Epitaxial LaNiO₄+delta Thin Films by Electrical Conductivity Relaxation*. Solid State Ionics, 2006. **177**(17-18): p. 1461-1467.
131. Kerman, K., C.H. Ko, and S. Ramanathan, *Orientation Dependent Oxygen Exchange Kinetics on Single Crystal SrTiO₃ Surfaces*. Physical Chemistry Chemical Physics, 2012. **14**(34): p. 11953-11960.
132. Ko, C.H., A. Karthikeyan, and S. Ramanathan, *Studies on Oxygen Chemical Surface Exchange and Electrical Conduction in Thin Film Nanostructured Titania at High Temperatures and Varying Oxygen Pressure*. Journal of Chemical Physics, 2011. **134**(1).
133. Diethelm, S., A. Closset, K. Nisancioglu, J. Van herle, A.J. McEvoy, and T.M. Gur, *Simultaneous Determination of Chemical Diffusion and Surface Exchange Coefficients of Oxygen by the Potential Step Technique*. Journal of the Electrochemical Society, 1999. **146**(7): p. 2606-2612.
134. Diethelm, S., A. Closset, J. Van herle, and K. Nisancioglu, *Determination of chemical diffusion and surface exchange coefficients of oxygen by electrochemical impedance spectroscopy*. Journal of the Electrochemical Society, 2002. **149**(11): p. E424-E432.
135. Bieger, T., J. Maier, and R. Waser, *An Optical in-Situ Method to Study Redox-Kinetics in SrTiO₃*. Berichte Der Bunsen-Gesellschaft-Physical Chemistry Chemical Physics, 1993. **97**(9): p. 1098-1104.
136. Huang, P.N. and A. Petric, *Superior Oxygen Ion Conductivity of Lanthanum Gallate Doped with Strontium and Magnesium*. Journal of the Electrochemical Society, 1996. **143**(5): p. 1644-1648.
137. Yasuda, I. and M. Hishinuma, *Electrical Conductivity and Chemical Diffusion Coefficient of Strontium-doped Lanthanum Manganites*. Journal of Solid State Chemistry, 1996. **123**(2): p. 382-390.
138. Marina, O.A., N.L. Canfield, and J.W. Stevenson, *Thermal, Electrical, and Electrocatalytical Properties of Lanthanum-doped Strontium Titanate*. Solid State Ionics, 2002. **149**(1-2): p. 21-28.
139. Kim, M.C., S.J. Park, H. Haneda, J. Tanaka, and S. Shirasaki, *High-Temperature Electrical-Conductivity of La_{1-x}Sr_xFeO₃-Delta (x-Greater-Than-0.5)*. Solid State Ionics, 1990. **40-1**: p. 239-243.

140. Mizusaki, J., M. Yoshihiro, S. Yamauchi, and K. Fueki, *Nonstoichiometry and Defect Structure of the Perovskite-Type Oxides La_{1-x}Sr_xFeO_{3-Δ}*. Journal of Solid State Chemistry, 1985. **58**(2): p. 257-266.
141. Kilner, J.A. and R.J. Brook, *A Study of Oxygen Ion Conductivity in Doped Nonstoichiometric Oxides*. Solid State Ionics, 1982. **6**(3): p. 237-252.
142. Wang, L., R. Merkle, J. Maier, T. Acarturk, and U. Starke, *Oxygen Tracer Diffusion in Dense Ba_{0.5}Sr_{0.5}Co_{0.8}Fe_{0.2}O_{3-Δ} Films*. Applied Physics Letters, 2009. **94**(7).
143. Zeng, P.Y., Z.H. Chen, W. Zhou, H.X. Gu, Z.P. Shao, and S.M. Liu, *Re-evaluation of Ba_{0.5}Sr_{0.5}Co_{0.8}Fe_{0.2}O_{3-Δ} Perovskite as Oxygen Semi-permeable Membrane*. Journal of Membrane Science, 2007. **291**(1-2): p. 148-156.
144. McIntosh, S., J.F. Vente, W.G. Haije, D.H.A. Blank, and H.J.M. Bouwmeester, *Oxygen Stoichiometry and Chemical Expansion of Ba_{0.5}Sr_{0.5}Co_{0.8}Fe_{0.2}O_{3-Δ} Measured by in Situ Neutron Diffraction*. Chemistry of Materials, 2006. **18**(8): p. 2187-2193.
145. Bucher, E., A. Egger, P. Ried, W. Sitte, and P. Holtappels, *Oxygen Nonstoichiometry and Exchange Kinetics of Ba_{0.5}Sr_{0.5}Co_{0.8}Fe_{0.2}O_{3-Δ}*. Solid State Ionics, 2008. **179**(21-26): p. 1032-1035.
146. van der Haar, L.M., M.W. den Otter, M. Morskate, H.J.M. Bouwmeester, and H. Verweij, *Chemical Diffusion and Oxygen Surface Transfer of La_{1-x}Sr_xCoO_{3-Δ} Studied with Electrical Conductivity Relaxation*. Journal of the Electrochemical Society, 2002. **149**(3): p. J41-J46.
147. Wang, S., A. Verma, Y.L. Yang, A.J. Jacobson, and B. Abeles, *The Effect of the Magnitude of the Oxygen Partial Pressure Change in Electrical Conductivity Relaxation Measurements: Oxygen Transport Kinetics in La_{0.5}Sr_{0.5}CoO_{3-Δ}*. Solid State Ionics, 2001. **140**(1-2): p. 125-133.
148. Feng, Z.A., F. El Gabaly, X. Ye, Z.-X. Shen, and W.C. Chueh, *Fast Vacancy-mediated Oxygen Ion Incorporation across the Ceria-gas Electrochemical Interface*. Nat Commun, 2014. **5**.
149. Imanishi, N., T. Matsumura, Y. Sumiya, K. Yoshimura, A. Hirano, Y. Takeda, D. Mori, and R. Kanno, *Impedance Spectroscopy of Perovskite Air Electrodes for SOFC Prepared by Laser Ablation Method*. Solid State Ionics, 2004. **174**(1-4): p. 245-252.
150. Yan, L., K.R. Balasubramaniam, S.L. Wang, H. Du, and P.A. Salvador, *Effects of Crystallographic Orientation on the Oxygen Exchange Rate of La_{0.7}Sr_{0.3}MnO₃ Thin Films*. Solid State Ionics, 2011. **194**(1): p. 9-16.
151. Jin-Phillipp, N.Y., N. Sata, J. Maier, C. Scheu, K. Hahn, M. Kelsch, and M. Ruhle, *Structures of BaF₂-CaF₂ Heterolayers and their Influences on Ionic Conductivity*. Journal of Chemical Physics, 2004. **120**(5): p. 2375-2381.

152. Karthikeyan, A., C.L. Chang, and S. Ramanathan, *High Temperature Conductivity Studies on Nanoscale Ytria-doped Zirconia Thin Films and Size Effects*. Applied Physics Letters, 2006. **89**(18).
153. Kosacki, I., C.M. Rouleau, P.F. Becher, J. Bentley, and D.H. Lowndes, *Surface Interface-related Conductivity in Nanometer Thick YSZ Films*. Electrochemical and Solid State Letters, 2004. **7**(12): p. A459-A461.
154. Guo, X., W. Sigle, J. Fleig, and J. Maier, *Role of Space Charge in the Grain Boundary Blocking Effect in Doped Zirconia*. Solid State Ionics, 2002. **154**: p. 555-561.
155. Guo, X., W. Sigle, and J. Maier, *Blocking Grain Boundaries in Ytria-doped and Undoped Ceria Ceramics of High Purity*. Journal of the American Ceramic Society, 2003. **86**(1): p. 77-87.
156. Sase, M., J. Suzuki, K. Yashiro, T. Otake, A. Kaimai, T. Kawada, J. Mizusaki, and H. Yugami, *Electrode Reaction and Microstructure of La_{0.6}Sr_{0.4}CoO_{3-delta} Thin Films*. Solid State Ionics, 2006. **177**(19-25): p. 1961-1964.
157. Mavrikakis, M., B. Hammer, and J.K. Norskov, *Effect of Strain on the Reactivity of Metal Surfaces*. Physical Review Letters, 1998. **81**(13): p. 2819-2822.
158. Suntivich, J., H.A. Gasteiger, N. Yabuuchi, H. Nakanishi, J.B. Goodenough, and Y. Shao-Horn, *Design Principles for Oxygen-Reduction Activity on Perovskite Oxide Catalysts for Fuel Cells and Metal-Air Batteries*. Nature Chemistry, 2011. **3**(7): p. 546-550.
159. Lee, Y.L., J. Kleis, J. Rossmeisl, Y. Shao-Horn, and D. Morgan, *Prediction of solid oxide fuel cell cathode activity with first-principles descriptors*. Energy & Environmental Science, 2011. **4**(10): p. 3966-3970.
160. Jung, W. and H.L. Tuller, *A New Model Describing Solid Oxide Fuel Cell Cathode Kinetics: Model Thin Film SrTi_{1-x}FexO_{3-d} Mixed Conducting Oxides-a Case Study*. Advanced Energy Materials, 2011. **1**(6): p. 1184-1191.
161. Swallow, J.G., W.H. Woodford, Y. Chen, Q. Lu, J.J. Kim, D. Chen, Y.M. Chiang, W.C. Carter, B. Yildiz, H.L. Tuller, and K.J. Van Vliet, *Chemomechanics of ionically conductive ceramics for electrical energy conversion and storage*. Journal of Electroceramics, 2014. **32**(1): p. 3-27.
162. Chu, M., Y.K. Sun, U. Aghoram, and S.E. Thompson, *Strain: A Solution for Higher Carrier Mobility in Nanoscale MOSFETs*. Annu. Rev. Mater. Res., 2009. **39**: p. 203-229.
163. Baykan, M.O., S.E. Thompson, and T. Nishida, *Strain Effects on Three-Dimensional, Two-Dimensional, and One-Dimensional Silicon Logic Devices: Predicting the Future of Strained Silicon*. J. Appl. Phys., 2010. **108**(9): p. 093716-1 - 093716-24.

164. Kim, S., M. Yokoyama, N. Taoka, R. Nakane, T. Yasuda, O. Ichikawa, N. Fukuhara, M. Hata, M. Takenaka, and S. Takagi, *Strained $In_{0.53}Ga_{0.47}As$ Metal-Oxide-Semiconductor Field-Effect Transistors with Epitaxial Based Biaxial Strain*. Appl. Phys. Lett., 2012. **100**(19): p. 193510-1 - 193510-3.
165. Cai, Z.H., Y. Kuru, J.W. Han, Y. Chen, and B. Yildiz, *Surface Electronic Structure Transitions at High Temperature on Perovskite Oxides: The Case of Strained $La_{0.8}Sr_{0.2}CoO_3$ Thin Films*. Journal of the American Chemical Society, 2011. **133**(44): p. 17696-17704.
166. Han, J.W. and B. Yildiz, *Enhanced one Dimensional Mobility of Oxygen on Strained $LaCoO_3$ (001) Surface*. Journal of Materials Chemistry, 2011. **21**(47): p. 18983-18990.
167. Sillassen, M., P. Eklund, N. Pryds, E. Johnson, U. Helmersson, and J. Bottiger, *Low-Temperature Superionic Conductivity in Strained Yttria-Stabilized Zirconia*. Advanced Functional Materials, 2010. **20**(13): p. 2071-2076.
168. Li, B., J.M. Zhang, T. Kaspar, V. Shutthanandan, R.C. Ewing, and J. Lian, *Multilayered YSZ/GZO Films with Greatly Enhanced Ionic Conduction for Low Temperature Solid Oxide Fuel Cells*. Physical Chemistry Chemical Physics, 2013. **15**(4): p. 1296-1301.
169. Bhatia, S. and B.W. Sheldon, *Compositional Stresses in Polycrystalline Titania Films*. J. Am. Cer. Soc., 2008. **91**(12): p. 3986-3993.
170. Sheldon, B.W., S. Mandowara, and J. Rankin, *Grain Boundary Induced Compositional Stress in Nanocrystalline Ceria Films*. Solid State Ionics, 2013. **233**(0): p. 38-46.
171. Freund, L.B. and S. Suresh, *Thin Film Materials: Stress, Defect Formation and Surface Evolution*. 2003, New York, NY: Cambridge University Press.
172. Kimura, Y., T. Kushi, S.-i. Hashimoto, K. Amezawa, and T. Kawada, *Influences of Temperature and Oxygen Partial Pressure on Mechanical Properties of $La_{0.6}Sr_{0.4}Co_{1-y}Fe_yO_{3-\delta}$* Journal of the American Ceramic Society, 2012. **95**(8): p. 2608-2613.
173. Kuhn, M., S. Hashimoto, K. Sato, K. Yashiro, and J. Mizusaki, *Thermo-chemical Lattice Expansion in $La_{0.6}Sr_{0.4}Co_{1-y}Fe_yO_{3-\delta}$* . Solid State Ionics, 2013. **241**(0): p. 12-16.
174. Messerschmidt, U., D. Baither, B. Baufeld, and M. Bartsch, *Plastic Deformation of Zirconia Single Crystals: A Review*. Materials Science and Engineering A-Structural Materials Properties Microstructure and Processing, 1997. **233**(1-2): p. 61-74.
175. Wang, Y., K. Duncan, E.D. Wachsman, and F. Ebrahimi, *The Effect of Oxygen Vacancy Concentration on the Elastic Modulus of Fluorite-Structured Oxides*. Solid State Ionics, 2007. **178**(1-2): p. 53-58.
176. Ganeshanathan, R. and A.V. Virkar, *Measurement of surface exchange coefficient on porous $La_{0.6}Sr_{0.4}CoO_{3-\delta}$ samples by conductivity relaxation*. Journal of The Electrochemical Society, 2005. **152**(8): p. A1620-A1628.

177. Ganeshanathan, R. and A.V. Virkar, *Measurement of Surface Exchange Coefficient on Porous $La_{0.6}Sr_{0.4}CoO_{3-\delta}$ Samples by Conductivity Relaxation*. Journal of the Electrochemical Society, 2005. **152**(8): p. A1620-A1628.
178. Freund, L.B. and S. Suresh, *Thin Film Materials: Stress, Defect Formation, and Surface Evolution*. 2003, New York, NY: Cambridge University Press. xviii, 750 p.
179. Yan, L., K.R. Balasubramaniam, S. Wang, H. Du, and P.A. Salvador, *Effects of Crystallographic Orientation on the Oxygen Exchange Rate of $La_{0.7}Sr_{0.3}MnO_3$ Thin Films*. Solid State Ionics, 2011. **194**(1): p. 9-16.
180. Kim, S., S. Wang, X. Chen, Y.L. Yang, N. Wu, A. Ignatiev, A.J. Jacobson, and B. Abeles, *Oxygen Surface Exchange in Mixed Ionic Electronic Conductors: Application $La_{0.5}Sr_{0.5}Fe_{0.8}Ga_{0.2}O_{3-\delta}$* . Journal of the Electrochemical Society, 2000. **147**(6): p. 2398-2406.
181. den Otter, M.W., H.J.M. Bouwmeester, B.A. Boukamp, and H. Verweij, *Reactor Flush Time Correction in Relaxation Experiments*. Journal of the Electrochemical Society, 2001. **148**(2): p. J1-J6.
182. Karthikeyan, A. and S. Ramanathan, *Oxygen Surface Exchange Studies in Thin Film Gd-doped Ceria*. Applied Physics Letters, 2008. **92**(24): p. 243109-1 - 243109-3.
183. Yang, Q., R.R. Lunt, and J.D. Nicholas, *Low Temperature Lanthanum Strontium Ferrite Thin Film Stress and Oxygen Surface Exchange Coefficient Measurements*. ECS Transactions, 2013. **58**(3): p. 37-46.
184. Klein, C.A., *How Accurate are Stoney's Equation and Recent Modifications*. Journal of Applied Physics, 2000. **88**(9): p. 5487-5489.
185. Kushi, T., K. Sato, A. Unemoto, S. Hashimoto, K. Amezawa, and T. Kawada, *Elastic Modulus and Internal Friction of SOFC Electrolytes at High Temperatures under Controlled Atmospheres*. Journal of Power Sources, 2011. **196**(19): p. 7989-7993.
186. Alben, S., B. Balakrishnan, and E. Smela, *Edge Effects Determine the Direction of Bilayer Bending*. Nano Letters, 2011. **11**(6): p. 2280-2285.
187. Meyer, S.L., *Data Analysis for Scientists and Engineers*. 1992: Peer Management Consultants, Limited.
188. Chick, L.A., L.R. Pederson, G.D. Maupin, J.L. Bates, L.E. Thomas, and G.J. Exarhos, *Glycine-Nitrate Combustion Synthesis of Oxide Ceramic Powders*. Materials Letters, 1990. **10**: p. 6-12.
189. Eason, R., *Pulsed Laser Deposition of Thin Films: Applications-led Growth of Functional Materials*. 2007: Wiley-Interscience.

190. Kremer, J.R., D.N. Mastrorade, and J.R. McIntosh, *Computer Visualization of Three-dimensional Image Data Using IMOD*. Journal of Structural Biology, 1996. **116**(1): p. 71-76.
191. Ritter, M. and P.A. Midgley, *A Practical Approach to Test the Scope of FIB-SEM 3D Reconstruction*. Journal of Physics: Conference Series, 2010. **241**(1): p. 012081.
192. Brandon, D. and W.D. Kaplan, *Microstructural Characterization of Materials*. 2008: Wiley.
193. Fossdal, A., M. Menon, I. Waernhus, K. Wiik, M.A. Einarsrud, and T. Grande, *Crystal Structure and Thermal Expansion of La_{1-x}Sr_xFeO_{3-delta}*. Journal of the American Ceramic Society, 2004. **87**(10): p. 1952-1958.
194. Kuhn, M., S. Hashimoto, K. Sato, K. Yashiro, and J. Mizusaki, *Oxygen Nonstoichiometry, Thermo-chemical Stability and Lattice Expansion of La_{0.6}Sr_{0.4}FeO_{3-delta}*. Solid State Ionics, 2011. **195**(1): p. 7-15.
195. Kharton, V.V., A.A. Yaremchenko, M.V. Patrakeev, E.N. Naumovich, and F.M.B. Marques, *Thermal and Chemical Induced Expansion of La_{0.3}Sr_{0.7}(Fe,Ga)O_{3-delta} Ceramics*. Journal of the European Ceramic Society, 2003. **23**(9): p. 1417-1426.
196. Sagdahl, L.T., M.-A. Einarsrud, and T. Grande, *Sintering Behaviour of La_{1-x}Sr_xFeO_{3-delta} Mixed Conductors*. Journal of the European Ceramic Society, 2006. **26**(16): p. 3665-3673.
197. Bahteeva, J.A., I.A. Leonidov, M.V. Patrakeev, E.B. Mitberg, V.L. Kozhevnikov, and K.R. Poeppelmeier, *High-temperature Ion Transport in La_{1-x}Sr_xFeO_{3-delta}*. Journal of Solid State Electrochemistry, 2004. **8**(9): p. 578-584.
198. Jacobson, A.J., *Materials for Solid Oxide Fuel Cells*. Chemistry of Materials, 2010. **22**(3): p. 660-674.
199. Bongio, E.V., H. Black, F.C. Raszewski, D. Edwards, C.J. McConville, and V.R.W. Amarakoon, *Microstructural and High-temperature Electrical Characterization of La_{1-x}Sr_xFeO_{3-delta}*. Journal of Electroceramics, 2005. **14**(3): p. 193-198.
200. Kuhn, M., S. Hashimoto, K. Sato, K. Yashiro, and J. Mizusaki, *Oxygen Nonstoichiometry, Thermo-chemical Stability and Lattice Expansion of La_{0.6}Sr_{0.4}FeO_{3-delta}*. Solid State Ionics, 2011. **195**(1): p. 7-15.
201. Dann, S.E., D.B. Currie, M.T. Weller, M.F. Thomas, and A.D. Alrawwas, *The Effect of Oxygen Stoichiometry on Phase-Relations and Structure in the System La_{1-x}Sr_xFeO_{3-delta} (0-Less-Than-or-Equal-to-X-Less-Than-or-Equal-to-1, 0-Less-Than-or-Equal-to-Delta-Less-Than-or-Equal-to-0.5)*. Journal of Solid State Chemistry, 1994. **109**(1): p. 134-144.

202. Simner, S.P., J.P. Shelton, M.D. Anderson, and J.W. Stevenson, *Interaction between La(Sr)FeO₃ SOFC Cathode and YSZ Electrolyte*. Solid State Ionics, 2003. **161**(1-2): p. 11-18.
203. Yang, Q., T.E. Burye, R.R. Lunt, and J.D. Nicholas, *In Situ Oxygen Surface Exchange Coefficient Measurements on Lanthanum Strontium Ferrite Thin Films via a New Curvature Relaxation Method*. Solid State Ionics, 2013.
204. Chevalier, J., L. Gremillard, A.V. Virkar, and D.R. Clarke, *The Tetragonal-Monoclinic Transformation in Zirconia: Lessons Learned and Future Trends*. Journal of the American Ceramic Society, 2009. **92**(9): p. 1901-1920.
205. Selçuk, A., G. Merere, and A. Atkinson, *The Influence of Electrodes on the Strength of Planar Zirconia Solid Oxide Fuel Cells*. Journal of Materials Science, 2001. **36**(5): p. 1173-1182.
206. Kim, G., S. Wang, A.J. Jacobson, and C.L. Chen, *Measurement of Oxygen Transport Kinetics in Epitaxial La₂NiO_{4+δ} Thin Films by Electrical Conductivity Relaxation*. Solid State Ionics, 2006. **177**(17-18): p. 1461-1467.
207. Sheldon, B.W., S. Mandowara, and J. Rankin, *Grain Boundary Induced Compositional Stress in Nanocrystalline Ceria Films*. Solid State Ionics, 2013. **233**: p. 38-46.
208. Mosleh, M., M. Sogaard, and P.V. Hendriksen, *Kinetics and Mechanisms of Oxygen Surface Exchange on La_{0.6}Sr_{0.4}FeO_{3-δ} Thin Films*. Journal of the Electrochemical Society, 2009. **156**(4): p. B441-B457.
209. Orlovskaya, N., H. Anderson, M. Brodnikovskyy, M. Lugovy, and M.J. Reece, *Inelastic Deformation Behavior of La_{0.6}Sr_{0.4}FeO₃ Perovskite*. Journal of Applied Physics, 2006. **100**(2).
210. Araki, W. and J. Malzbender, *Ferroelastic Deformation of La_{0.58}Sr_{0.4}Co_{0.2}Fe_{0.8}O_{3-δ} under Uniaxial Compressive Loading*. Journal of the European Ceramic Society, 2013. **33**(4): p. 805-812.
211. Araki, W. and J. Malzbender, *Electrical Conductivity of La_{0.58}Sr_{0.4}Co_{0.2}Fe_{0.8}O_{3-δ} during Ferroelastic Deformation under Uniaxial Compressive Loading*. Solid State Ionics, 2013. **233**: p. 67-72.
212. Williamson, G.K. and W.H. Hall, *X-ray Line Broadening from Filled Aluminium and Wolfram*. Acta Metallurgica, 1953. **1**(1): p. 22-31.
213. Lussier, A., J. Dvorak, S. Stadler, J. Holroyd, M. Liberati, E. Arenholz, S.B. Ogale, T. Wu, T. Venkatesan, and Y.U. Idzerda, *Stress Relaxation of La_{1/2}Sr_{1/2}MnO₃ and La_{2/3}Ca_{1/3}MnO₃ at Solid Oxide Fuel Cell Interfaces*. Thin Solid Films, 2008. **516**(6): p. 880-884.

214. Sillassen, M., P. Eklund, N. Pryds, E. Johnson, U. Helmersson, and J. Bottiger, *Low-Temperature Superionic Conductivity in Strained Yttria-Stabilized Zirconia (vol 20, pg 2071, 2010)*. Advanced Functional Materials, 2010. **20**(19): p. 3194-3194.
215. Selcuk, A., G. Merere, and A. Atkinson, *The influence of electrodes on the strength of planar zirconia solid oxide fuel cells*. Journal of Materials Science, 2001. **36**(5): p. 1173-1182.
216. Chen, Y., W. Jung, Z.H. Cai, J.J. Kim, H.L. Tuller, and B. Yildiz, *Impact of Sr Segregation on the Electronic Structure and Oxygen Reduction Activity of SrTi1-xFexO3 Surfaces*. Energy & Environmental Science, 2012. **5**(7): p. 7979-7988.
217. Fister, T.T., D.D. Fong, J.A. Eastman, P.M. Baldo, M.J. Highland, P.H. Fuoss, K.R. Balasubramaniam, J.C. Meador, and P.A. Salvador, *In Situ Characterization of Strontium Surface Segregation in Epitaxial La(0.7)Sr(0.3)MnO(3) Thin Films as a Function of Oxygen Partial Pressure*. Applied Physics Letters, 2008. **93**(15).
218. Fischer, E. and J.L. Hertz, *Measurability of the Diffusion and Surface Exchange Coefficients using Isotope Exchange with Thin Film and Traditional Samples*. Solid State Ionics, 2012. **218**: p. 18-24.
219. Jung, W. and H.L. Tuller, *Investigation of Surface Sr Segregation in Model Thin Film Solid Oxide Fuel Cell Perovskite Electrodes*. Energy & Environmental Science, 2012. **5**(1): p. 5370-5378.
220. Yang, Q., T.E. Burye, R.R. Lunt, and J.D. Nicholas, *In situ Oxygen Surface Exchange Coefficient Measurements on Lanthanum Strontium Ferrite Thin Films via the Curvature Relaxation Method*. Solid State Ionics, 2013. **249–250**(0): p. 123-128.
221. Yang, Q. and J.D. Nicholas, *Porous Thick Film Lanthanum Strontium Ferrite Stress and Oxygen Surface Exchange Bilayer Curvature Relaxation Measurements*. Journal of the Electrochemical Society, 2014. **Accepted**.
222. Chen, Z.W., X. Wang, V. Bhakhri, F. Giuliani, and A. Atkinson, *Nanoindentation of Porous Bulk and Thin Films of La0.6Sr0.4Co0.2Fe0.8O3-delta*. Acta Materialia, 2013. **61**(15): p. 5720-5734.
223. Lipinska-Chwalek, M., F. Schulze-Koppers, and J. Malzbender, *Stability Aspects of Porous Ba0.5Sr0.5Co0.8Fe0.2O3-delta*. Ceramics International, 2014. **40**(5): p. 7395-7399.
224. Selcuk, A. and A. Atkinson, *Elastic Properties of Ceramic Oxides Used in Solid Oxide Fuel Cells (SOFC)*. Journal of the European Ceramic Society, 1997. **17**(12): p. 1523-1532.
225. Fan, X., E.D. Case, Q. Yang, and J.D. Nicholas, *Room Temperature Elastic Properties of Gadolinia-doped Ceria as a Function of Porosity*. Ceramics International, 2013. **39**(6): p. 6877-6886.

226. Kimura, Y., T. Kushi, S.-i. Hashimoto, K. Amezawa, and T. Kawada, *Influences of Temperature and Oxygen Partial Pressure on Mechanical Properties of $La_{0.6}Sr_{0.4}Co_{1-y}Fe_yO_{3-\delta}$* . Journal of the American Ceramic Society, 2012. **95**(8): p. 2608-2613.
227. Bhatia, S. and B.W. Sheldon, *Compositional Stresses in Polycrystalline Titania Films*. Journal of the American Ceramic Society, 2008. **91**(12): p. 3986-3993.
228. Yasuda, I. and T. Hikita, *Precise Determination of the Chemical Diffusion Coefficient of Calcium - Doped Lanthanum Chromites by Means of Electrical Conductivity Relaxation*. Journal of the Electrochemical Society, 1994. **141**(5): p. 1268-1273.